UNIVERSITÀ DEGLI STUDI DI PAVIA
DOTTORATO DI RICERCA IN FISICA – XXIX CICLO

# Effects of electric and magnetic fields on the event reconstruction in the ICARUS T600 detector

Marta Torti

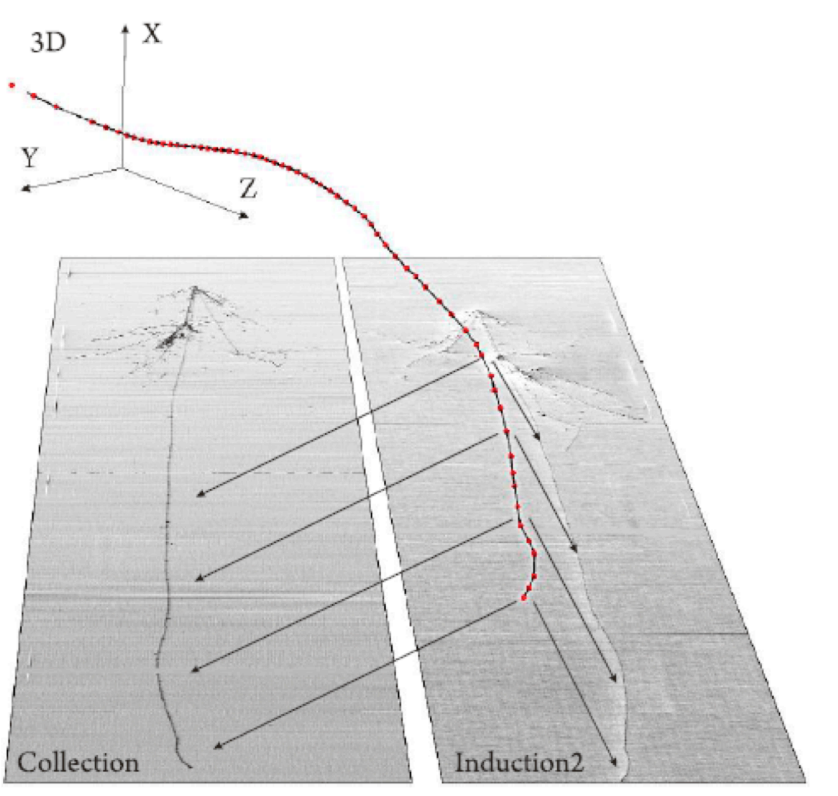


Tesi per il conseguimento del titolo

*Full title:*
Effects of electric and magnetic fields on the event reconstruction in the ICARUS T600 detector

*Short title for the side if necessary:*
Effects of E and B fields on the ICARUS event reconstruction

Marta Torti

2016

Università di Pavia

Università degli Studi di Pavia
Dipartimento di Fisica

INFN Sez. di Pavia

DOTTORATO DI RICERCA IN FISICA - XXIX CICLO

# Effects of electric and magnetic fields on the event reconstruction in the ICARUS T600 detector

Marta Torti

Submitted to the Graduate School of Physics in partial fulfilment of the requirements for the degree of

DOTTORE DI RICERCA IN FISICA

DOCTOR OF PHILOSOPHY IN PHYSICS

at the

University of Pavia

Supervisor: Prof. Alessandro Menegolli

**Cover:** General idea of the ICARUS T600 event reconstruction.

**Effects of electric and magnetic fields on the event reconstruction in the ICARUS T600 detector**

*Marta Torti*
PhD thesis - University of Pavia
Pavia, Italy, December 2016

# Contents

# List of Figures

# Introduction

In the last twenty years, many experiments using neutrinos from various sources (solar, atmospheric, accelerators, reactors) confirmed the existence of neutrino oscillations and established a coherent phenomenological picture. This scenario is characterised by three active neutrino flavours ($\nu_e$, $\nu_\mu$, $\nu_\tau$) and by three mass eigenstates ($\nu_1$, $\nu_2$, $\nu_3$) with small mass differences, while mixing angles are relatively large.
However, in recent years, a number of anomalies were observed, that point out to possible non-standard oscillations models which could imply the existence of a fourth (or more) neutrino, called *sterile neutrino* because it does not undergo to weak interaction. In Chap. 1 a review of present neutrino oscillation theory and of experimental hints for the presence of sterile neutrino is illustrated.
The sterile neutrino existence, or its absence, represents one of the main puzzles in the present neutrino physics scenario, which calls for a definitive clarification with new data. A new generation of experimental programs is under construction, with the specific purpose to clarify this issue.
In particular, the Short Baseline Neutrino (SBN) program at Fermilab (FNAL), will exploit three Liquid Argon Time Projection Chamber (LAr TPC) detectors along the $\nu_{mu}$ beam produced by the Booster Neutrino Beamline (BNB). Each detector has different mass, and a different position respect to the neutrino production point: the near detector ($\sim$110 m) SBND is the smallest, the intermediate detector ($\sim$479 m) MicroBooNE is the medium sized while the biggest one is the far detector ($\sim$600 m), the ICARUS T600. Thanks to the significative cancellation of systematics related to neutrino flux and cross section or detector effects, it is expected to explore the parameter space region relevant to the sterile neutrino anomaly at a $\sim 5\sigma$ confidence level for 3 years of data taking. Two of the three detectors involved in this program, MicroBooNE and ICARUS, are existing while SBND has to be build anew.
This Ph.D. thesis is focused on the ICARUS T600 detector, the largest LAr TPC ever built, that concluded successfully the operation at Gran Sasso National Laboratories (LNGS) in Italy, where it was exposed, from 2010 to 2012, at underground conditions, to the CNGS (CERN Neutrinos to Gran Sasso) $\nu_\mu$ beam, in order to study oscillations to both $\nu_\tau$ and $\nu_e$ states.

After the CNGS beam shut down, the detector continued taking data with cosmic rays until the middle 2013, when the T600 was de-commissioned and transported to CERN, where it is now under refurbishment, before moving to FNAL. Various renovations are indeed necessary, due to the experimental conditions at FNAL, where the detector will be at shallow depths, very different from the deep underground LNGS ones.In Chap. 2 I will describe the detector characteristics, the results obtained during LNGS operation and what is needed in order to make the detector suitable for the shallow depths conditions, as it will be a FNAL.
In a LAr TPC, when a charge particle crosses the detector, ionizing electrons are drifted towards the wire anode planes, where they are collected providing two spatial coordinates of the track; arrays of PMTs detect scintillation light, providing the measurement of the absolute time of occurrence that, combined with the knowledge of the drift velocity, permits the determination of the third coordinate of the track, that along the drift direction. The goal of the ICARUS reconstruction procedure, as I will describe in detail in Chap. 3, is to extract, in an accurate way, all the physical information contained in the wire and PMT output signals, i.e. the energy deposited by the different particles and the point where the deposition occurred, to build a complete 3D spatial and calorimetric picture of the event. To have this faithful event reconstruction, it is mandatory to determine wire and drift coordinates accurately and so it is essential to understand everything that could distort these information.
The uniformity of electric field is essential in order to ensure an uniform drift velocity and thus the proportionality between drift time and drift coordinate. Electric field distortions may arise by a local accumulation of positive ions, that are drifted towards the cathode more slowly than the electrons, along the drift path. This accumulation is emphasised by high interaction rate, given for example by high cosmic ray flux.
This problem, called *space charge*, could be present at FNAL, where the ICARUS T600 detector will be placed at shallow depths, with a cosmic ray flux much higher than in underground conditions. In order to understand the influence of this effect in track reconstruction, I analysed a data sample collected in 2001, where the detector was at surface condition for a test run in Pavia (Italy). I will describe the parameter used to study space charge effects in the ICARUS detector and the results obtained in Chap. 4.
As stated before, the drift coordinate precision is derived by the electrons drifted towards the wire planes and it is affected by several factors, such as the diffusion. In the ICARUS T600 detector, it is possible to estimate the longitudinal diffusion only, that parallel to the drift direction, because the spatial resolution due to the wires pitch is such to hide the effects of transverse diffusion, i.e. that perpendicular to the drift direction. To evaluate the longitudinal diffusion parameter, a dedicated run with different electric field values was performed collecting cosmic rays at the end of LNGS run. In Chap. 5 I will described the analysis of these data samples in order to evaluate this

parameter, considering the dependence of the width of the signal registered by the TPC.
The ICARUS Collaboration is also involved in a long time project, called DUNE (Deep Underground Neutrino Experiment): it will be a long baseline experiment, with modular kiloton LAr-TPCs, to be built in the next 20 years in a South Dakota mine (USA). The T600 could be used as Near Detector in this future experiment, once provided with a magnetic field for precise particle momentum measurements and charged particle identification.
The presence of a magnetic field introduces new parameters and possibilities for the reconstruction procedure. In fact it will became possible to identify the charge of particles, thanks to their behaviour under the influence of a magnetic field. In this framework, I developed an algorithm, described in Chap. 6, for the discrimination between electron neutrino and electron antineutrino, considering their interaction products. I developed the algorithm within the ICARUS analysis framework and tested it on a Monte Carlo sample.

Chapter 1

# Neutrino oscillations and sterile neutrinos

The Standard Model (SM) was formulated in the 60's by Glashow [1], Weinberg [2] and Salam [3]. In this model neutrinos are massless fermions, described by left-handed Weyl spinors [4, 5, 6] and are subject neither to strong nor to electromagnetic interactions. To keep neutrinos massless the non existence of right-handed neutrino fields is assumed: they are in fact necessary in order to generate Dirac neutrino masses, with the same Higgs mechanism that generates the Dirac masses of quarks and charged leptons.
The SM predicts three generations of neutrinos, as part of the left-handed lepton doublets

$$L_l = \begin{pmatrix} \nu_{lL} \\ l_L \end{pmatrix} \tag{1.1}$$

where $l = e,\mu,\tau$. The standard neutrino interactions are described by the leptonic Charged Current (CC)

$$j^{\rho}_{W,L} = 2 \cdot \sum_{\alpha=e,\mu,\tau} \overline{\nu}_{\alpha,L} \gamma^{\rho} l_{\alpha,L} = \sum_{\alpha=e,\mu,\tau} \overline{\nu}_{\alpha} \gamma^{\rho} \left(1 - \gamma^5\right) l_{\alpha}, \tag{1.2}$$

and by the neutrino part of the leptonic Neutral Current (NC)

$$j^{\rho}_{Z,\nu} = \sum_{\alpha=e,\mu,\tau} \overline{\nu}_{\alpha,L} \gamma^{\rho} \nu_{\alpha,L} = \frac{1}{2} \sum_{\alpha=e,\mu,\tau} \overline{\nu}_{\alpha} \gamma^{\rho} \left(1 - \gamma^5\right) \nu_{\alpha}, \tag{1.3}$$

which enter respectively into the leptonic charged-current weak interaction Lagrangian

$$\mathcal{L}^{(CC)}_{l} = -\frac{g}{2\sqrt{2}} \left( j^{\rho}_{W,L} W_{\rho} + j^{\rho\dagger}_{W,L} W_{\rho\dagger} \right), \tag{1.4}$$

and in the neutrino part of the leptonic neutral-current weak interaction Lagrangian

$$\mathcal{L}_{\nu}^{(NC)} = -\frac{g}{2\cos\vartheta_W} j^{\rho}_{Z,\nu} Z_{\rho}, \tag{1.5}$$

where $g$ is the SU(2) gauge coupling constant, $\vartheta_W$ is the Weinberg angle, $W_\rho$ and $Z_\rho$ are fields of charged $W^{\pm}$ and neutral $Z^0$ vector bosons.
This theoretical structure describes, with impressive accuracy, neutrino interactions: so far, no deviation from the standard neutrino interactions have been found in experimental data [7].
On the other hand, an intnse experimental investigation carried out with a broad variety of source, energies, baseline lenngths and detectors has led to the establishment of a scenario in which neutrinos change their flavour from the source to the detector. This characteristic can be explained with the mechanism of neutrino oscillations, first proposed by Pontecorvo in 1958 [8], as periodical transitions among different flavour neutrinos which implies massive neutrinos. The first experimental evidence of neutrino oscillations led to the Nobel Prize to T. Kajita and A.B. McDonald [9].
Furthermore a number of hints have been collected in neutrino oscillation experiments for the existence of sterile neutrinos, i.e. a neutral lepton with no ordinary interactions except those induced by mixing. Their existence is not yet an evidence but it certainly pose an experimental problem that needs clarification.

## 1.1 Neutrino oscillations theory

If neutrinos have small mass and are mixed particles, neutrino oscillations take place [10, 11, 12].
In the theory of neutrino mixing, the flavour state of a neutrino $|\nu_\alpha\rangle$ produced in a weak process is a superposition of the states of neutrinos with definite masses:

$$|\nu_\alpha\rangle = \sum_k U_{k\alpha} |\nu_k\rangle \qquad \alpha = e, \mu, \tau \quad k = 1, 2, 3, \tag{1.6}$$

where $|\nu_k\rangle$ are the mass eigenstates, while $U_{k\alpha}$ is an unitary matrix, which describes the neutrino mixing (called Pontecorvo Maki Nakagawa Sakata PMNS matrix). The massive neutrino states $|\nu_k\rangle$ are eigenstates of the Hamiltonian,

$$\mathcal{H} |k\rangle = E_k |\nu_k\rangle , \tag{1.7}$$

with energy eigenvalues

$$E_k = \sqrt{\mathbf{p^2} + m_k^2}. \tag{1.8}$$

The Schrödinger equation

$$i\frac{d}{dt} |\nu_k(t)\rangle = \mathcal{H} |\nu_k(t)\rangle , \tag{1.9}$$

implies that the massive neutrino states evolve in time as plane waves:

$$|\nu_k(t)\rangle = e^{-iE_k t}\,|\nu_k\rangle\,. \tag{1.10}$$

Consider now a beam composed of neutrinos of a definite flavour $\alpha$. In the following, the three momentum $\mathbf{p}$ of the different components in the beam will be assumed the same; differences in energy will derive from the masses differences. The neutrino, created with the flavour $\alpha$ at time $t = 0$, is described by Eq. 1.6. After a time $t$, the evolution of the initial beam is

$$|\nu_\alpha(t)\rangle = \sum_k U_{\alpha k} e^{-iE_k t}\,|\nu_k\rangle\,. \tag{1.11}$$

Since all $E_k$ are not equal if the masses are not, Eq. 1.11 represents a different superimposition of the physical eigenstates $\nu_k$ compared to Eq. 1.6. In the neutrino mixing theory, this state has not only the properties of a $\nu_\alpha$, but also of other flavour states. The amplitude of finding a $\nu_\beta$ in the original $\nu_\alpha$ beam is

$$\begin{aligned}\langle\nu_\beta|\nu_\alpha(t)\rangle &= \sum_{k,j}\langle\nu_j|U^\dagger_{j\beta}e^{-iE_k t}U_{\alpha k}|\nu_k\rangle \\ &= \sum_k e^{-iE_k t}U_{\alpha k}U^*_{\beta k},\end{aligned} \tag{1.12}$$

considering that the mass eigenstates are orthonormal ($\langle\nu_k|\nu_j\rangle = \delta_{kj}$).
At $t = 0$, as expected, the amplitude is $\delta_{\alpha\beta}$, due to the unitarity of the matrix $U$. At time $t$, the probability of finding a $\nu_\beta$ in an original $\nu_\alpha$ beam is

$$\begin{aligned}P_{\nu_\alpha\nu_\beta}(t) &= |\langle\nu_\beta|\nu_\alpha(t)\rangle|^2 \\ &= \sum_{k,j}|U_{\alpha k}U^*_{\beta k}U^*_{\alpha j}U_{\beta j}|\cos\left[(E_k - E_j)\,t - \phi_{\alpha\beta jk}\right],\end{aligned} \tag{1.13}$$

where

$$\phi_{\alpha\beta jk} = \arg\left(U_{\alpha k}U^*_{\beta k}U^*_{\alpha j}U_{\beta j}\right). \tag{1.14}$$

Neutrinos are extremely relativistic, so the energy-momentum relation (Eq. 1.8) can be approximated as

$$E_k \sim |\mathbf{p}| + \frac{m_k^2}{2|\mathbf{p}|}\,, \tag{1.15}$$

and also the time $t$ can be replaced by the distance $x$ traveled by the beam. Thus one obtains

$$P_{\nu_\alpha\nu_\beta}(x) = \sum_{k,j}|U_{\alpha k}U^*_{\beta k}U^*_{\alpha j}U_{\beta j}|\cos\left(\frac{2\pi x}{L_{kj}} - \phi_{\alpha\beta jk}\right), \tag{1.16}$$

where, writing $|\mathbf{p}| = E$ for sake of brevity, one defines

$$L_{kj} \equiv \frac{4\pi E}{\Delta m^2_{kj}}\,, \tag{1.17}$$

where

$$\Delta m^2_{kj} \equiv m^2_k - m^2_j\,. \tag{1.18}$$

The quantities $|L_{kj}|$ give a distance scale over which the oscillation effects can be appreciable and they are called *oscillation lengths*.
Let us consider the simplest case of an oscillation between two neutrinos only. In this case, the matrix $U$ takes a particularly simple form:

$$\begin{pmatrix} \cos\vartheta & \sin\vartheta \\ -\sin\vartheta & \cos\vartheta \end{pmatrix}. \tag{1.19}$$

Eq. (1.16) now reduces to

$$\begin{aligned} P_{conv}(x) &= \sin^2 2\vartheta \sin^2\left(\frac{1.27\Delta m^2}{E}x\right) \\ P_{surv}(x) &= 1 - \sin^2 2\vartheta \sin^2\left(\frac{1.27\Delta m^2}{E}x\right), \end{aligned} \tag{1.20}$$

where the terms $P_{conv}$ and $P_{surv}$ denote, respectively, the conversion and the survival probabilities of a particular neutrino flavour. The numerical constant 1.27 applies if $\Delta m^2 = |m_1^2 - m_2^2|$ is expressed in $(\mathrm{eV/c^2})^2$, while the distance from the neutrino source $x$ is expressed in meters and the energy $E$ in MeV.
The experimental data thus restrict $\Delta m^2$ as a function of $\sin^2 2\vartheta$ from the limits of the observed probabilities. In the case of three neutrinos, instead, the mixing matrix becomes more complex, with three mixing angle and a phase. Its most common parametrization is:

$$U = \begin{pmatrix} 1 & 0 & 0 \\ 0 & c_{23} & s_{23} \\ 0 & -s_{23} & c_{23} \end{pmatrix} \begin{pmatrix} c_{13} & 0 & s_{13}e^{-i\delta} \\ 0 & 1 & 0 \\ -s_{13}e^{+i\delta} & 0 & c_{13} \end{pmatrix} \begin{pmatrix} c_{12} & s_{12} & 0 \\ -s_{12} & c_{12} & 0 \\ 0 & 0 & 1 \end{pmatrix} \tag{1.21}$$

where $c_{jk} = \cos(\theta_{jk})$ and $s_{jk} = \sin(\theta_{jk})$.
This form of the matrix turns out to be very useful when considering experimental data with fixed baseline and neutrino energy range: the first matrix contains the parameters relevant for atmospheric and accelerator neutrino oscillations, the second one contains the parameters accessible to short baseline reactor experiments and the CP violating phase $\delta$, while the third matrix depends upon the parameters involved in solar neutrino oscillations.
The exposed theory is valid for neutrinos traveling in vacuum. When neutrinos propagate in matter, as for solar neutrino inside the Sun, oscillations are modified by the coherent interactions with the medium, which produce effective

potentials that are different for different neutrino flavours [13]. In particular $\nu_e$ can have both NC and CC interactions with matter electrons, while $\nu_{\mu,\tau}$ are susceptible only to NC interactions.
Neutrino oscillations in matter, as neutrino oscillations in vacuum, depend on the differences of the squared neutrino masses, not on the absolute value of neutrino masses, with an effective mixing angle in matter $\vartheta_M$. For a particular electron density the effective mixing angle is equal to $\pi/4$, i.e. the mixing is maximal, leading to the possibility of total transitions between the two flavours if the resonance region is wide enough. This mechanism is referred as Mikheev-Smirnov-Wolfenstein (MSW) effect [14].

### 1.1.1 Neutrino oscillations: experimental status

The theory exposed above is confirmed by many experimental results that involved different type of detectors in the lasts decades. All the mixing angle of the matrix $U$ (Eq. 1.21) have been measured, as well as the difference of the squared masses; the global fit values of all experimental results are reported in Tab. 1.1 [15] and plotted in Fig. 1.1 [16]. The preferred value of the CP-violing phase lies around $\delta \simeq \pi$, although with low statistical significance [17].

| Parameter | Best Fit ($\pm$ 1 $\sigma$) |
|---|---|
| $\Delta m_{12}$ | $7.54^{+0.26}_{-0.22} \times 10^{-5}$ eV$^2$ |
| $\lvert\Delta m_{23}\rvert \simeq \lvert\Delta m_{13}\rvert$, $\Delta m_{13}>0$ | $2.46 \pm 0.06 \times 10^{-3}$ eV$^2$ |
| $\lvert\Delta m_{23}\rvert \simeq \lvert\Delta m_{13}\rvert$, $\Delta m_{13}<0$ | $2.38 \pm 0.06 \times 10^{-3}$ eV$^2$ |
| $\sin^2\theta_{12}$ | $0.308 \pm 0.017$ |
| $\sin^2\theta_{23}$, $\Delta m_{13}>0$ | $0.437^{+0.033}_{-0.023}$ |
| $\sin^2\theta_{23}$, $\Delta m_{13}<0$ | $0.455^{+0.039}_{-0.031}$ |
| $\sin^2\theta_{13}$, $\Delta m_{13}>0$ | $0.0234^{+0.0020}_{-0.0019}$ |
| $\sin^2\theta_{13}$, $\Delta m_{13}<0$ | $0.0240^{+0.0019}_{-0.0022}$ |

Table 1.1: The best-fit values of the 3-neutrino oscillation parameters, derived from a global fit of the current neutrino oscillation data [15].

However a lot of questions about neutrinos remain unresolved. Up to now, direct or kinematic searches have not revealed any indication for non vanishing neutrino masses, and also the neutrino mass hierarchy remains unknown.
Even the mechanism that gives mass to neutrinos remains object of discussion, such as their Majorana or Dirac nature (see [7] for detailed description).
A series of experimental anomalies, uncorrelated with each other but all hinting at oscillation phenomena driven by $\Delta m^2$ and $\sin^2 2\theta$ parameters not compatible with the values in Tab. 1.1, suggested a different numeber of neutrino families $N_\nu$, that could not be three as accepted until now.
Result from LEP on the Z-boson decay width [18], implies that there are only three weakly interacting flavours (called *active neutrinos*), but sets no limits

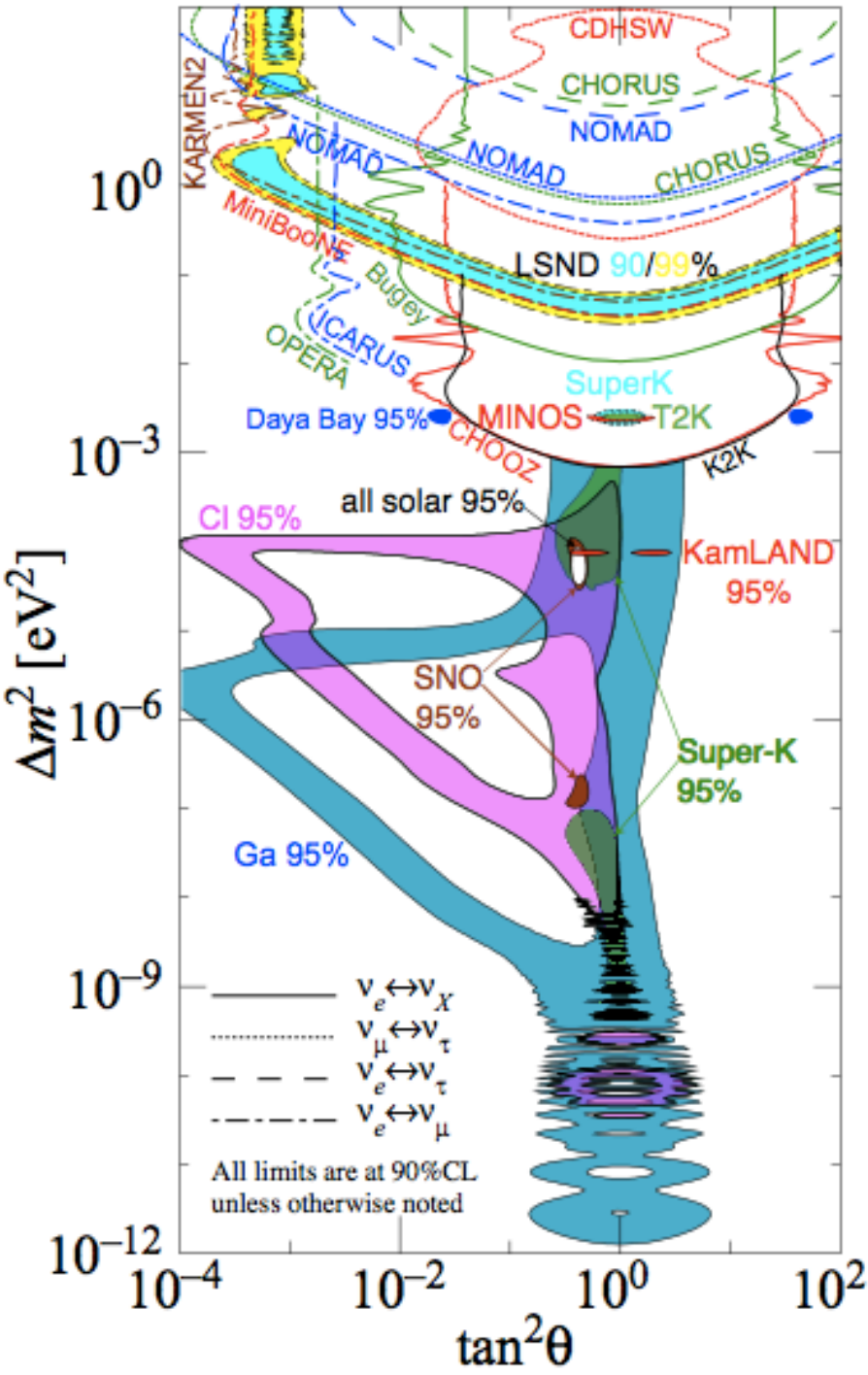


Figure 1.1: Plot of the experimental results obtained in the neutrino oscillation sector [16].

on the number of non interacting flavours, called *sterile neutrinos*.
Measurement of anisotropies of the Cosmic Microwave Background, sensible to the number of neutrino families, do not exclude $N_\nu > 3$; in particular $N_\nu = 4$ is also consistent with 95% C.L [19], also if tensions remain between cosmogenic results and the possible presence of light sterile neutrino.

## 1.2 Sterile neutrino

Sterile neutrinos [20] are hypothetical types of neutrinos that do not interact via any of the fundamental interactions of the Standard Model, except gravity. Since they would not interact electromagnetically, weakly or strongly, they are extremely difficult to detect. However, oscillations with ordinary neutrinos are possible: only in this way we can reveal their presence.
There are some experimental hints on their presence: anomalous results have been reported in LSND [21], MiniBooNE [25], radioactive source experiments [28, 29] and short baseline reactor experiments [35]. Also results of the global fit of short-baseline neutrino oscillation experiments [36] show that the data can be explained by the addition of one or two sterile neutrinos to the three active neutrinos of the Standard Model, the so called (3+1) and (3+2) scenarios respectively [7]. However some tensions remain between appearance and disappearance data in the global fits [30]. It is worth noting that sterile neutrinos would affect the oscillation probabilities of the active flavours and therefore could influence cosmological processes [31].

### 1.2.1 Short baseline experiment

The first evidence in favour of oscillations beyond the three-flavour framework came from the LSND (Liquid Scintillator Neutrino Detector) experiment [21] that run from 1993 to 1998. It was a scintillation and Cherenkov light detector, installed at Los Alamos National Laboratory, 30 m away from an accelerator $\overline{\nu}_\mu$ source, with $20 < E_{\overline{\nu}} < 200$ MeV, to search for $\overline{\nu}_\mu \rightarrow \overline{\nu}_e$ oscillations with high sensitivity. An excess of $\overline{\nu}_e$ over the expected from background and standard oscillation was found, with an oscillation probability of $(0.264 \pm 0.067 \pm 0.045)\%$, leading to a $> 3\sigma$ evidence for $\overline{\nu}_\mu \rightarrow \overline{\nu}_e$ oscillation with $\Delta m^2 > 0.2$ eV$^2$, much higher than the standard $\Delta m^2$, reported in Tab. 1.1. In the ($\sin^2 2\theta$,$\Delta m^2$) parameter space, the most favoured allowed region is in the band of $\Delta m^2$ from 0.2 to 2.0 eV$^2$ (see Fig. 1.2) [22].
The KARMEN (KArlsruhe Rutherford Medium Energy Neutrino) experiment [23], very similar to LSND, did no observed such an excess during its operation (1990 - 2001). It rules out a part of the mass-mixing parameters region allowed by LSND, but, due to the smaller baseline (17.5 m vs 30 m), in the region $\Delta m^2 < 2$ eV$^2$ and $\Delta m^2 \sim 7$ eV$^2$ KARMEN result is compatible with the LNSD oscillation evidence (see Fig. 1.2) [24].
To test the LSND anomaly, the experiment MiniBooNE (Booster Neutrino

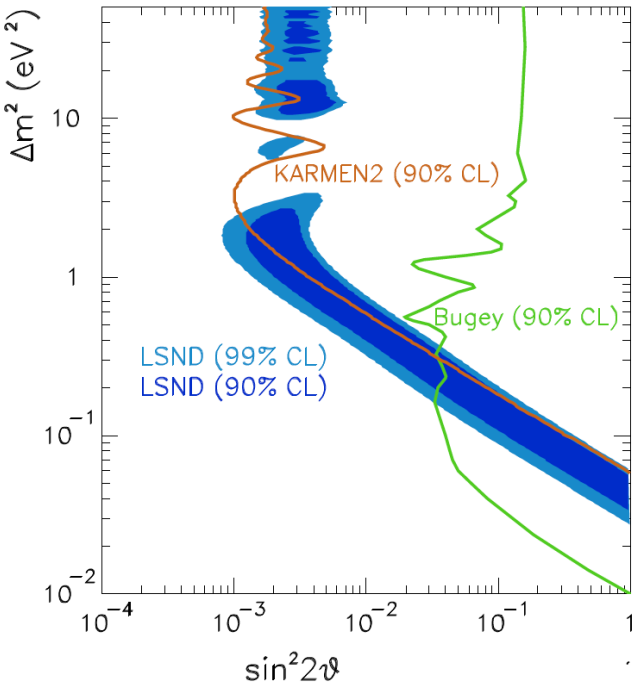


Figure 1.2: The ($\sin^2 2\theta$,$\Delta m^2$) oscillation parameter fit for the entire LSND data sample, $20 < E_{\overline{\nu}} < 200$ MeV [22].

Experiment) [25] was developed at Fermilab. It was placed 541 m from the beam source. It studied both $\overline{\nu}_\mu \rightarrow \overline{\nu}_e$ and $\nu_\mu \rightarrow \nu_e$. It found an excess of $\nu_e$ events both in antineutrino and neutrino analysis (see Fig. 1.3) [26, 27]. In antineutrino mode this excess is very similar to what is expected from neutrino oscillation based on the LSND signal (see Fig. 1.4); in neutrino mode, instead, the data in the energy range sensitive to LSND oscillations are consistent with the background oscillation, while a $3\sigma$ excess at low energy could correspond to a significantly different $L/E$ distribution than that suggested by LSND anomaly.

### 1.2.2 Gallium experiment

The GALLEX (GALLium EXperiment) [28] and SAGE (Soviet American Gallium Experiment) [29] solar neutrino detectors were two Gallium radioactive source experiments to study solar neutrino oscillations starting their operation in 1994. During their calibration procedures, they showed an indiction of $\nu_e$ disappearence. This calibration procedure consisted in introducing intense artificial $^{51}$Cr and $^{37}$Ar radioactive sources inside the detectors and counting the number of $^{71}$Ge contaminating the $^{71}$Ga as a consequence of the inverse beta decay. The radioactive nuclei decay through electron capture ($e^- + X \rightarrow Y + \nu_e$) and the emitted neutrino is then detected through the reaction

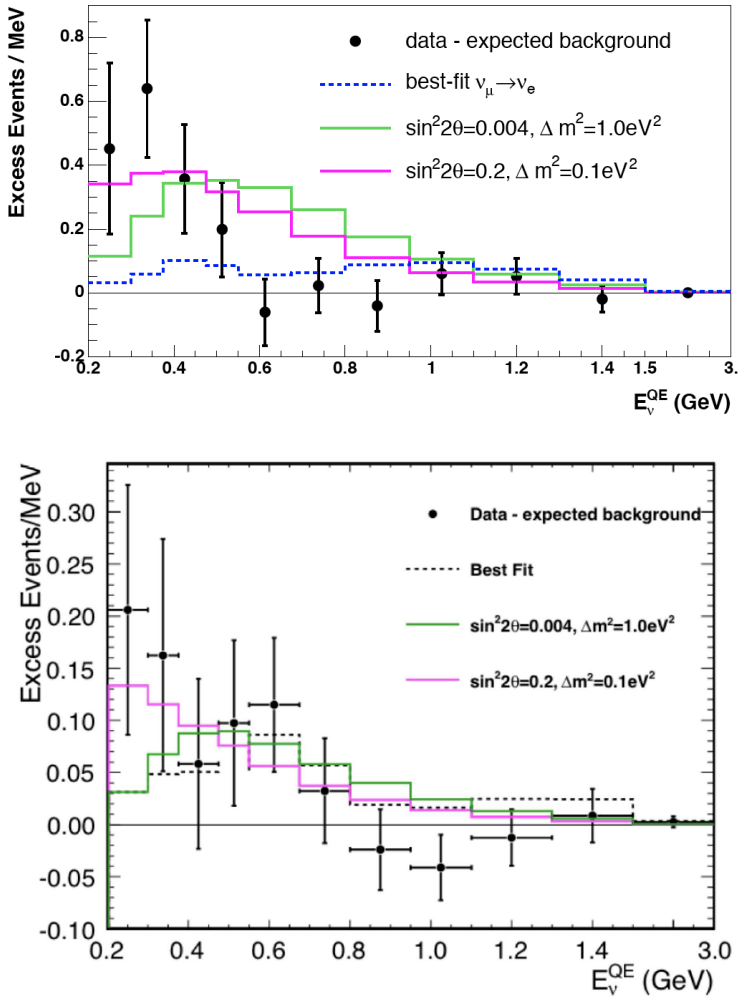


Figure 1.3: The excess of $\nu_e$ (top) and $\overline{\nu}_e$ (bottom) candidate events observed by MiniBooNE in neutrino and antineutrino mode respectively [27].

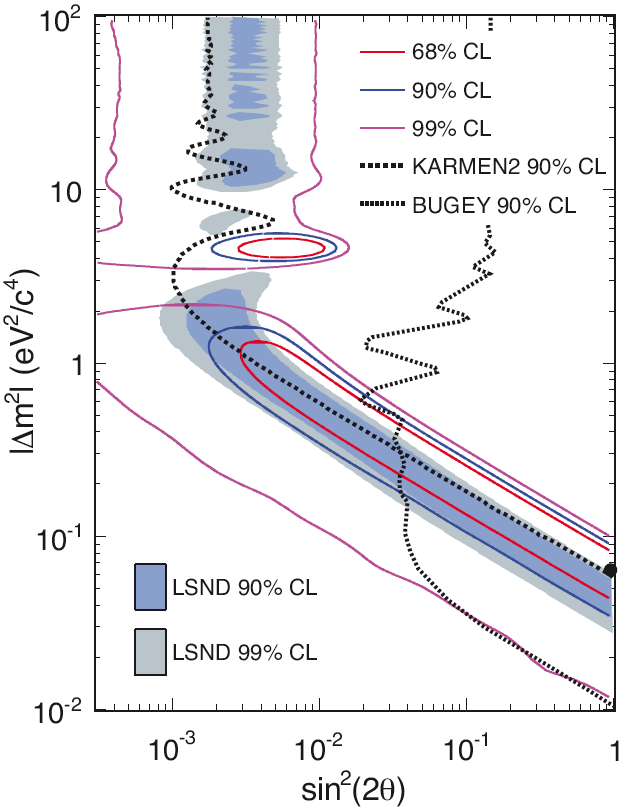


Figure 1.4: The MiniBooNE oscillation allowed region in antineutrino mode [27].

$$\nu_e + {}^{71}Ga \rightarrow {}^{71}Ge + e^-, \tag{1.22}$$

which has a low neutrino energy threshold, $E_\nu^{th}(^{71}\text{Ga}) = 0.233$ MeV. The value of the ratio $R$ between measured and predicted $^{71}$Ge production rate, averaged between the two experiment, is

$$R = 0.86 \pm 0.05. \tag{1.23}$$

Thus, the number of measured events is about 2.8 $\sigma$ smaller than the prediction: in terms of neutrino oscillations this indicates an oscillation amplitude of $\sin^2 2\theta \geq 0.07$ and a squared-mass difference $\Delta m^2 \geq 0.35$ eV$^2$ at 99% C.L. [32].

### 1.2.3 Reactor experiment

Nuclear reactors are very intense sources of neutrinos, produced along the $\beta$-decay chains of the fission products, that have been used all along the neutrino history, from its discovery up to the most recent oscillation studies. Since unstable fission products are neutron-rich nuclei, all $\beta$-decays are of $\beta^-$ type and the neutrino flux is an actually pure electronic antineutrinos one.
The neutrino oscillation search at a reactor is always based on a disappearance measurement: the observed neutrino spectrum at a distance $L$ from the reactor is compared to the expected spectrum. If a deficit is measured it can be interpreted in terms of disappearance probability. Until late 2010, all data from reactor neutrino experiments appeared to be fully consistent with the standard oscillation theory. The measured rate of $\overline{\nu}_e$ was in reasonable agreement with that predicted from the reactor antineutrino spectra, though slightly lower than expected, with a measured/expected ratio of $0.980 \pm 0.024$ [33].
In preparation for the Double Chooz reactor experiment, the Saclay reactor neutrino group re-evaluated the specific reactor antineutrino flux. In 2011, they reported their results [34], which correspond to a flux a few percent higher than the previous prediction. This also necessitated a re-analysis of the ratio between observed event rate and predicted rate for old published experiments with reactor-detector distances below 100 m. In Fig. 1.5 a general systematic shift with different significance below unity can be observed. These re-evaluations unveil a reactor antineutrino anomaly [35].
The average ratio is now $0.927 \pm 0.023$, leading to a significance at the 3 $\sigma$ confidence level of the reactor antineutrino anomaly. The best fit point for oscillation parameters is at $\Delta m^2 = 2.4$ eV$^2$ and $\sin(2\theta) \sim 0.14$ [35].

### 1.2.4 Global fit of present scenario

Several theoretical models have been proposed to explain the entire experimental landscape, from the extension of the Standard Model with only one sterile neutrino (3+1) to more complex scenario with additional states.

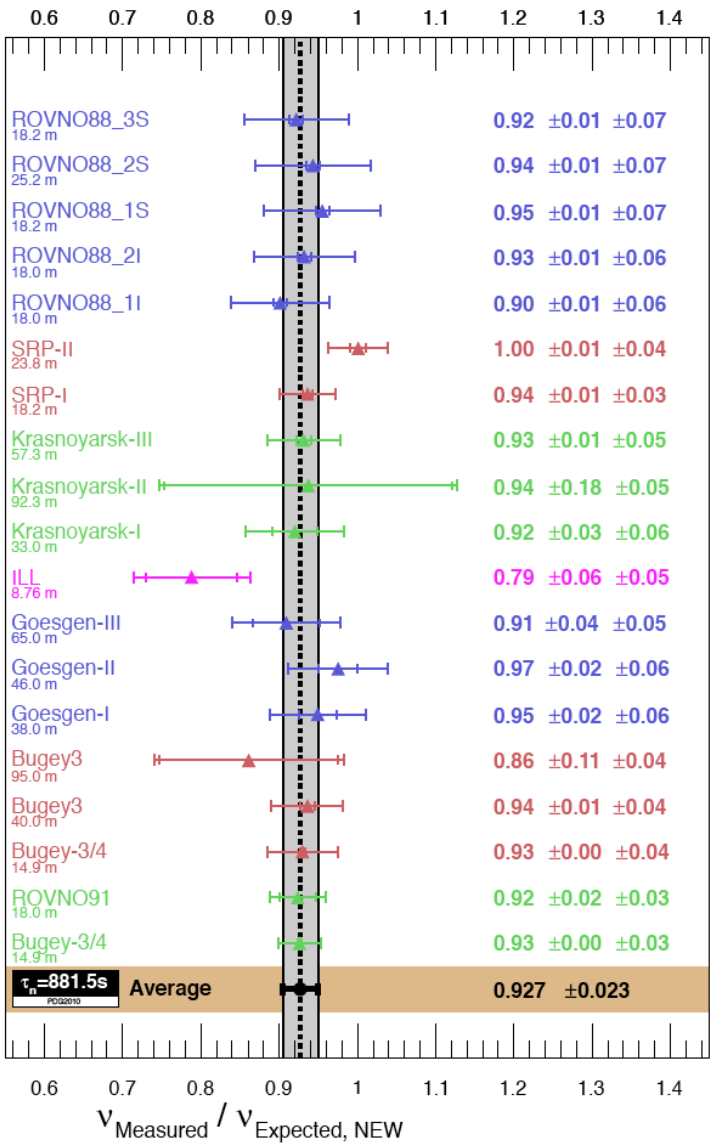


Figure 1.5: Weighted average (with correlations) of 19 measurements of reactor neutrino experiments operating at short baselines [35].

As a reference, in Fig. 1.6 global fits for short baseline data for the simplest (3+1) hypothesis are reported [36]. The allowed regions in the $\sin^2(2\theta_{e\mu}) - \Delta m^2_{41}$, $\sin^2(2\theta_{ee}) - \Delta m^2_{41}$ and $\sin^2(2\theta_{\mu\mu}) - \Delta m^2_{41}$ planes are shown, obtained with a fit, indicated as PrGLO global fit [37] in the picture, that does not include the low-energy excess of MiniBooNE. These regions are relevant, respectively, for $\nu_\mu \to \nu_e$ appearance, $\nu_e$ disappearance and $\nu_\mu$ disappearance searches. The figure shows also the region allowed by $\nu_\mu \to \nu_e$ appearance data and the constraints from $\nu_e$ disappearance and $\nu_\mu$ disappearance data. It can be seen that the combined disappearance constraint in the $\sin^2(2\theta_{e\mu}) - \Delta m^2_{41}$ plane excludes a large part of the region allowed by $\nu_\mu \to \nu_e$ appearance data, leading to a well-known appearance-disappearance tension.

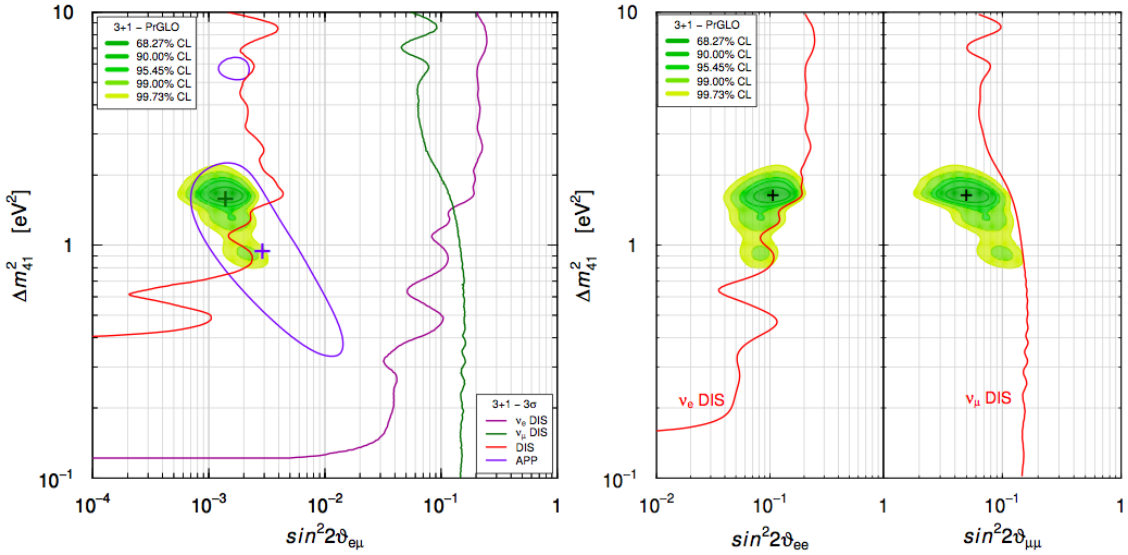


Figure 1.6: Allowed regions in the $\sin^2(2\theta_{e\mu}) - \Delta m^2_{41}$, $\sin^2(2\theta_{ee}) - \Delta m^2_{41}$ and $\sin^2(2\theta_{\mu\mu}) - \Delta m^2_{41}$ planes obtained in the 3+1-PrGLO global fit of short-baseline neutrino oscillation data compared with the $3\sigma$ allowed regions obtained from $\nu_\mu \to \nu_e$ short-baseline appearance data (APP) and the $3\sigma$ constraints obtained from $\nu_e$ short-baseline disappearance data ($\nu_e$ DIS), $\nu_\mu$ short-baseline disappearance data ($\nu_\mu$ DIS) and the combined short-baseline disappearance data (DIS). The best-fit points of the PrGLO and APP fits are indicated by crosses [36].

A tension is also indicated by cosmological data, between the necessity to have a sterile neutrino mass at the eV scale and the expected full thermalization of the sterile neutrinos through active-sterile oscillations in the early Universe [36].
Hence, the possible existence of light sterile neutrinos at the eV scale remains a hot topic of research and discussions.

## 1.3 Conclusions and future experiments

The LSND experiment stands perhaps as the first possible evidence of new physics, beyond the Standard Model, showing an excess $\overline{\nu}_e$ signal indicative of the existence of one or more sterile neutrinos. The nature of the signal is however limited to a rate, with some energy information. The MiniBooNE experiment did not see a direct evidence in $\nu_e$ appearance, though a low energy excess in their data could potentially accommodate the existence of sterile neutrinos. Their antineutrino data, though statistically limited, appear instead to show consistency with the original LSND signal. Calibration data from Gallex and Sage also suggest a deficit which hints at the existence of sterile neutrinos. Finally, the latest results from a re-analysis of the neutrino reactor data, which reflects a rate dependence as well, appear consistent with this sterile oscillation picture.
To proceed forward with the goal to establish or refute the existence of sterile neutrinos, multiple and possibly orthogonal approaches have arose, in the same spirit as employed for neutrino oscillations:

- **Reactor** experiments will investigate $\bar{\nu}_e$ disappearance at L/E $\sim$1 m/MeV, looking for an oscillation pattern imprinted in the energy distribution of events [38]. Neutrino interaction will be reconstructed by the coincidence of promo and delay signals of the final state of inverse beta deca reactions in liquid scintillator detectors, doped woth Gd or $^6$Li and possibly highly segmented, positioned at distances of the order of 10 m from high intensity nuclear reactors cores (Nucifer [39], DANSS [40] and SoLid [41]); solutions with moving detectors have been also proposed (Stereo [39], Neutrino4 [42] and Hanaro [43] ).

- Searches for $\nu_e$ and $\bar{\nu}_e$ disappearance will be carried out as well exploiting **radioactive source** placed near or inside large liquid scintillator (SOX [44], KamLAND [45, 46], JUNO [46], Daya Bay [47] and LENS [48]), radiochemical (BEST [49]) or bolometer (RICHOCET [50]) detectors [51]. In case of monochromatic $\nu_e$ is generated by nuclear electron capture ($^{51}$Cr) variations of the neutrino detection probability will be measured as a function of distance from the source, while in case of a continuos spectrum generated by nuclear $\beta$ decay (($^{144}$Ce) also distorions in the neutrino spectrum will be appreciable.

- Experiments at accelerators feauture the unique possibility to address both $\nu_e$ appearance and $\nu_\mu$ disappearance at the same time [52]. These investigations will be based on $\nu_\mu/\bar{\nu}_\mu$ beams produced by $\pi$/muons/kaons decay at rest (JPARK-MLF [53]), muon decay in flight (nuStorm [54]) and isotope decay at rest (ISODAR [55]), beyond the conventional $\pi$ decay in flight (SBN [87]).

Chapter 2

# The ICARUS experiment: past results and future perspectives

Historically, imaging detectors have always played a crucial role in particle physics. In the past century successive generations of detectors realised new ways to visualize particle interactions. In particular, bubble chamber detectors were a fruitful tool, permitting to visualize and study particle interactions, that provided fundamental contributions to particle physics discoveries. Huge bubble chambers, like Gargamelle [56], were extraordinary achievements, successfully employed in particular in neutrino physics.
In 1977, C.Rubbia [57] conceived the idea of a Liquid Argon Time Projection Chamber (LAr TPC), to perform the calorimetric measurement of particle energy together with the three-dimensional track reconstruction, from electrons drifting in an electric field in sufficiently pure liquid argon. The LAr TPC successfully reproduces the extraordinary imaging features of a bubble chamber, its medium and its spatial resolution being similar to those of heavy liquid bubble chambers, with the further feature of being a fully electronic detector, potentially scalable to huge masses (several kilotons). In addition, the LAr TPC provides excellent calorimetric measurements and has the great advantage of being continuously sensitive and self-triggering.
The ICARUS (Imaging Cosmic And Rare Underground Signals) T600 cryogenic detector is the largest LAr TPC ever realised, with the cryostat containing 760 tons of LAr (476 tons of active mass) splitted into two identical T300 modules [64]. Its construction finalised many years of R&D studies by the ICARUS Collaboration [58, 59, 60, 61, 62], with prototypes of growing mass developed both in laboratory and with industry involvement. Nowadays, it represents the state of the art of this technique and it marks a major milestone in the practical realisation of large-scale LAr detectors. The pre-assembly of the ICARUS T600 detector began in 1999 in Pavia (Italy); one of the T300 module was brought into operation in 2001. A test run lasting three months was carried out with exposure to cosmic rays on the surface, allowing for the first time an extensive study of the main detector features [63, 64].

After the test, in 2004 the two cryostats housing the internal detectors were transported to the underground Gran Sasso National Laboratories (LNGS), where operated with a remarkable efficiency from October 2010 to December 2012, accomplishing a three years physics program. It was placed in the Hall B of the LNGS, 1400 m deep (3800 m.w.e) and 730 km far from the source of the CNGS (CERN Neutrinos to Gran Sasso) beam, an almost pure $\nu_\mu$ beam produced by the SPS accelerator at CERN [65].
Collected neutrino events correspond to $8.6 \times 10^{19}$ protons on target (pot), with an efficiency exceeding 93%; a total of about 3000 CNGS neutrino events was collected and actively analysed [75] in order to study the $\nu_{mu} \rightarrow \nu_e$ and $\nu_{mu} \rightarrow \nu_{tau}$ neutrino oscillations. After the shut down of the beam, additional data were collected with cosmic rays trigger to study atmospheric neutrinos. Furthermore at the end of this data taking, some runs were collected varying the TPC electric field, in order to study diffusion parameter and test the limit of the readout electronics. From the technological point of view, the T600 run was a complete success, featuring a smooth operation, high live time, and high reliability [67, 68].
The T600 decommissioning process started in June 2013; after the emptying and warming-up phase, the cryostats were opened, to recover the internal TPC detectors and the cryogenic plant and electronics to be re-used in future projects. The two T300 modules were moved to CERN, where a complete overhauling (CERN WA104 project) is ongoing, preserving most of the existing operational equipment, while upgrading some components with up-to-date technology in view of the T600 future non-underground operation at FNAL.

## 2.1 Description of the ICARUS T600 detector

The ICARUS T600 detector (see Fig. 2.1) consisted of a large cryostat split into two identical, adjacent T300 modules, with internal dimensions $3.6 \times 3.9 \times 19.6$ m$^3$ each, filled with about 380 tons of ultra-pure LAr each; each module housed two TPCs separated by a common cathode, made of punched inox sheets with 58% transparency to light. The modules will be referred in the text as West module (the oldest one) and East module (the newest one), with respect to CNGS beam coming from the North and each module is divided in Left and Right chamber, with respect to the CNGS again.
One thermal insulation vessel surrounded the two modules: between the insulation and the aluminium containers a thermal shield was placed, with boiling nitrogen circulating inside to intercept the heat load and to maintain the cryostat bulk temperature uniform (within 1 K) and stable at 89 K.
To keep the electronegative impurities in LAr at a very low concentration level, each module was equipped with two gaseous argon (GAr) and one LAr recirculation/purification systems [65]. Argon gas was continuously drawn from the cryostat ceiling and, once re-condensed, let it pass through Oxysorb$^{\text{TM}}$ filters and finally re-injected into the LAr containers. LAr instead was recir-

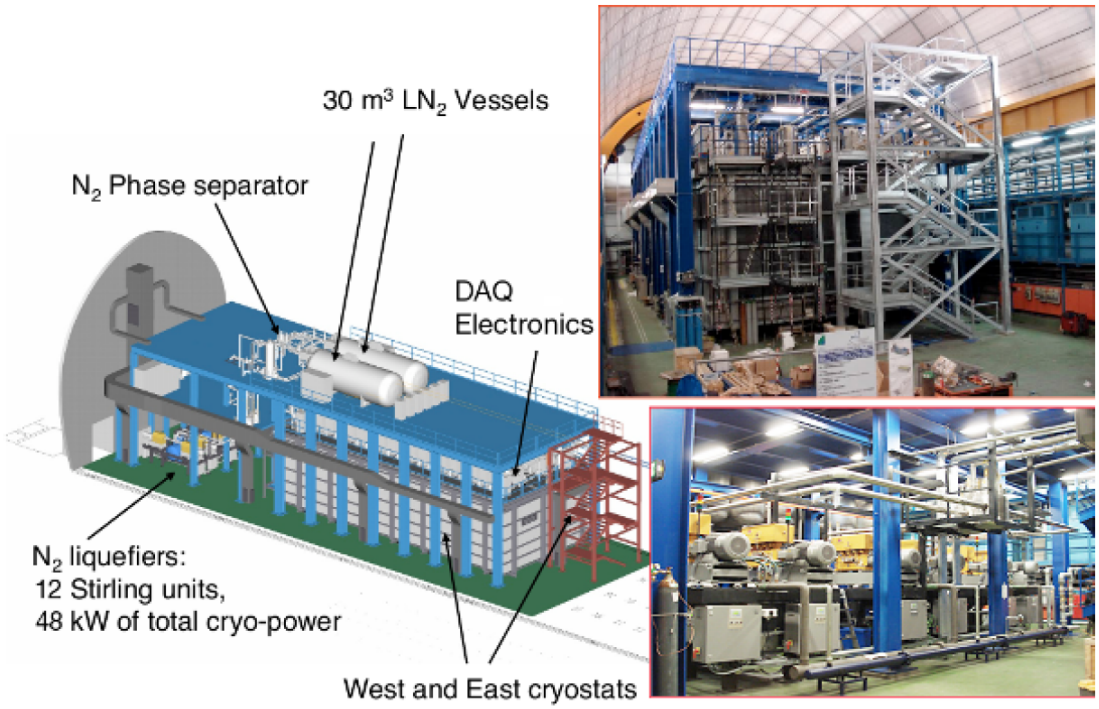


Figure 2.1: Left: schematic view of the whole ICARUS-T600 plant at LNGS. Right-top: photo of the detector installation. Right-bottom: details of the cryo-cooler plant.

culated by means of an immersed cryogenic pump and it was purified through standard Hydrosorb$^{TM}$ / Oxysorb$^{TM}$ filters before being re-injected into the cryostats. Convective motions induced by heat losses from the module walls ensured a fast and almost complete LAr mixing, minimizing the fluctuations of the relevant parameters, such as LAr density, temperature and purity. This solution permitted to reach an impressive result in terms of argon purity, with a corresponding free electron lifetime exceeding 15 ms [67].
A uniform electric field ($E_{drift}$ = 500 V/cm) perpendicular to the wires was established in the LAr volume of each half-module by means of a HV system, as required to allow and guide the drift of the ionization electrons. The system was composed of a cathode plane, parallel to the wire planes, placed in the centre of the LAr volume of each half-module at a distance of about 1.5 m from the wires of each side. This distance defines the maximum drift path (Fig. 2.2). The HV system was completed by field-shaping electrodes to guarantee the uniformity of the field along the drift direction, and by an HV feedthrough to mantain the cathode at the required potential of 75 kV [64].


Figure 2.2: Picture of the inner detector layout inside the first half-module: the cathode (vertical plane on the right) divides the volume in two symmetric sectors (chambers). The picture refers to the left sector where wires and mechanical structure of the TPC and some PMTs are visible.

Charged particles, generated for example by a neutrino interaction in LAr, produced ionization along their path. Thanks to the low transverse diffusion of charge in LAr, the images of the tracks, produced by ionization electron clouds, were preserved and, drifting along the electric field lines, were projected onto the anode, as illustrated in Fig. 2.3.

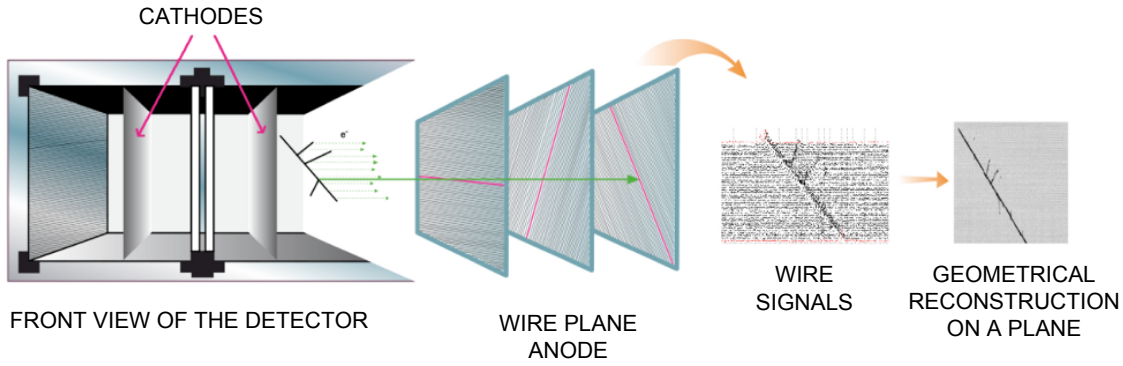


Figure 2.3: Illustration of the ICARUS T600 working principle: a charged particle ionization path in LAr and its geometrical reconstruction.

The TPC anode was made of three parallel planes of wires, 3 mm apart, facing the 1.5 m drift path. Globally, 53248 wires with length up to 9 m and 150 $\mu$m diameter were installed in the detector. By means of appropriate voltage biasing, the ionization charge induced signals in non-destructive way on the first two wire planes (Induction-1 and Induction-2), then it was finally collected by the last one (Collection plane). Wires were oriented on each plane at a different angle (0°, +60° , -60°) with respect to the horizontal direction. Therefore, combining the wire/drift coordinates on each plane at a given drift time, a three-dimensional reconstruction of the ionizing event could be obtained. A remarkable resolution of about 1 mm$^3$ was uniformly achieved over the whole detector active volume (340 m$^3$ corresponding to 476 t). The measurement of the absolute time of the ionizing event, combined with the electron drift velocity information ($v_{drift} \sim 1.6$ mm/$\mu$s at $E_{drift} = 500$ V/cm), provided the absolute positioning of the track along the drift coordinate.
The determination of the absolute time of the ionizing event was accomplished by the prompt detection of the scintillation light produced in LAr by charged particles. To this purpose, arrays of cryogenic Photo Multiplier Tubes (PMTs), coated with wavelength shifter (TetraPhenyl Butadiene, TPB) to allow the detection of Vacuum Ultra-Violet (VUV) scintillation light, were installed behind the wire planes.
The electronics was designed to allow continuous read-out, digitization and independent waveform recording of signals from each wire of the TPC. The read-out chain was organised on a 32-channels modularity. Signals of the charge sensitive front-end amplifiers were digitized with 10-bits ADCs with 400 ns sampling time. The overall gain was about 1 ADC count every 1000 electrons, setting the signal of minimum ionizing particles (m.i.p.) to $\sim$ 15

ADC counts. The average electronic noise was 1500 electrons, compared with the $\sim$ 15000 free electrons produced by a m.i.p. in 3 mm, leading to a signal to noise ratio S/N $\sim$ 10. The gain uniformity was measured with an accuracy of about 5%, mainly determined by the uncertainties on the capacitors adopted to generate the calibration pulses [64].
Digitised data were read out by the DAQ every time a trigger occurred. The main ICARUS T600 trigger for detecting CNGS beam related events required the coincidence of the PMT local trigger in at least one of the four TPC chambers within a 60 $\mu$s gate opened in correspondence of the proton spill extraction, delayed for the $\sim$ 2.44 ms CERN to LNGS neutrino time of flight. The PMT local trigger was obtained, separately for each TPC, as the linear sum of the collected PMT signals, properly discriminated in order to account for the different number of devices deployed in the two modules [66]. The analysis of the performance of the PMTs trigger system demonstrated an almost full efficiency for CNGS neutrino events above 300 MeV energy deposition on the full T600 active volume. Efficiency remained at $\sim$ 98.5% down to 100 MeV. The stability of the trigger system was verified within the measurement uncertainty, comparing different data sets collected during the CNGS run [66].

## 2.2 Operation and results at LNGS

During the operation at LNGS, the ICARUS T600 detector collected events from the CNGS beam, in order to study neutrino oscillations. From the technological point of view, this run was a complete success, featuring a smooth operation, high live time, and high reliability as described in [67, 68].
The CNGS neutrino facility [70, 71, 72] provided an almost pure $\nu_\mu$ beam with energy peaked in the range $10 \leq E_\nu \leq 30$ GeV, with a spectral contamination from $\overline{\nu}$ of about 2% and a $\nu_e$ component of slightly less than 1% [77].
From October $1^{st}$ 2010 to December $3^{rd}$ 2012 ICARUS T600 collected 19990 triggered events (see Tab. 2.1) [75].

| Event type | Number of events |
|---|---|
| $\nu$ | 2650 |
| Rock $\mu$ | 9245 |
| External | 3568 |
| Empty | 4527 |
| Total | 19990 |

Table 2.1: Classification of the CNGS events among neutrinos, $\mu$ from the rock, external interaction and empty [75].

Empty events inside the recorded CNGS sample were rejected by means a dedicated automatic filter based on total charge deposition, whose efficiency

close to 100% was checked on a sample of few thousands visually scanned events. A few neutrino interactions/day with vertex in the fiducial volume were recorded, as expected.
The classification of the events was performed visually, through a two level scanning [73]. The first level scanning was meant to identify [73]:

- neutrino interaction, by looking for neutral particle interaction vertices inside the detector active volume;
- muons from the rock (rock muons), i.e. $\mu$ from $\nu_\mu$ interaction inside the upstream rock, by looking for straight muon tracks along the beam directions entering the detector walls;
- residual of $\nu$ interaction with vertex outside the instrumented volume, by looking for events with physical activity close to the detector walls and without an interaction vertex clearly visible.

Furthermore, a preliminary classification of neutrino events was attempted by means of a visual scanning on the basis of simple criteria [73]:

- **muon candidate**: if a long or isolated muon track exits from the vertex without re-interactions;
- **e.m. candidate**: if an electromagnetic shower is recognised close to the interaction vertex;
- **NC candidate**: if neither electromagnetic shower close to the vertex nor muon tracks are clearly visible;
- doubt between muon and NC (**XC** in the following) in all the other cases.

The results of this scanning was inserted in a dedicated event database where the main characteristics of events, like run and event numbers, event classification and interaction vertex coordinates, were recorded.
A second level scanning was then performed focusing on the neutrino interactions only, to better define the data sample. For this purpose a Scanning Fiducial Volume (SFV) was defined by subtracting, from the instrumented volume of each TPC, 20 cm in the longitudinal beam direction (5 cm upstream and 15 cm downstream) and 3 cm in the drift and vertical dimension (1.5 cm per side). The $\nu$ induced event with vertex inside the SFV are then classified as [73]:

- $\nu_\mu$ **CC candidate**: if a muon track, longer than 2.5 m, exits from the vertex without re-interactions;
- **e.m. candidate**: if an electromagnetic shower is recognised with a distance from the vertex lower then 2 wires both in Collection and Induction 2 views and a muon track is not clearly visible;

- **NC candidate**: if neither electromagnetic shower close to the vertex nor muon track are clearly visible and if the event is not well balanced in the drift and vertical dimension;
- doubt between $\nu$ CC or NC (**XC**) event in all the other cases.

Results are reported in Tab. 2.2 [75].

| $\nu$ interaction type | Number of events |
|---|---|
| $\nu_\mu$ candidates | 1517 |
| e.m. candidates | 407 |
| NC candidates | 413 |
| XC | 313 |
| Total | 2650 |

Table 2.2: Second classification of the CNGS neutrino interactions [75].

The identification of the primary vertex of two-dimensional objects, like tracks and showers, was performed visually. The obtained clusters and reference points were fed to the three dimensional reconstruction algorithm, that will be described in Chap. 3.
The collected charge was calculated for each hit (a point in the wire-drift projection) in the Collection view after automatic hit finding and hit fitting (see Chap. 3). Each hit was corrected for the signal attenuation along the drift, according to the purity value as continuously monitored with cosmic muons.
Stopping tracks were processed for particle identification through specific ionization [76]. The total deposited energy was obtained by calibrated sum of hit charges in the region spanned by the event, with an average correction factor for signal quenching in LAr. In order to reproduce the signals from the actual events, a sophisticated simulation package dedicated to the ICARUS T600 detector was developed [77].

### 2.2.1 Search for LSND anomaly

The search for $\nu_\mu \rightarrow \nu_e$ events due to the LSND anomaly was based on $7.93 \times 10^{19}$ pot with a total of 2650 observed neutrino events collected in the whole period of data taking with the CNGS beam, in good agreement, within 6%, with the Monte Carlo expectation [75].
After the visual scanning classification (see Tab. 2.2), the number of neutrino events that showed an electromagnetic shower near the vertex (e.m. candidates in Tab. 2.2) was 407. It is a high number of electron neutrino candidates, therefore a more strict selection was performed.
To the initial sample, a more stringent fiducial volume cut was applied, compared with the SFV: the interaction vertex position was required to be at a distance of at least 5 cm from each side of the active volume and at least 50 cm

from its downstream wall. These cuts allowed for the identification of electron showers, but are not stringent enough neither for the reconstruction of neutrino energies, nor for the identification of $\nu_\mu$ CC vs NC events. Furthermore, only events with a deposited energy smaller than 30 GeV were included in the analysis, in order to optimise the signal over background ratio. Indeed, the oscillated events were expected to have energies in the 10-30 GeV range, like the bulk of the muon neutrino spectrum, while the beam $\nu_e$ contamination extends to higher energies. The radiation length of LAr is 14 cm ($\approx$ 45 readout wires), corresponding to a $\gamma$-conversion length of 18 cm. The ionization information of the early part, i.e. before the occurrence of the e.m. track showering, was examined wire by wire in order to tag the presence of an initial electron emitted in the neutrino interaction, as a powerful filter for $\gamma$-converting pairs, which are generally separated from the vertex and generate double minimum ionizing tracks. The rejection factor based on ionization increased dramatically with the photon energy increase, while the electron identification efficiency was almost constant. Indeed, the possible photon misidentification was essentially due to photons undergoing Compton scattering, whose cross section becomes negligible with respect to the pair production above a few hundreds MeV. Monte Carlo studies indicated a residual contamination of about 0.18% for the energy spectrum of photons from pion decays in CNGS events, rising to a few percent in the sub-GeV energy region. The loss in efficiency for electron showers was only 10% [77, 78].
In the analysis the electron signature was defined by the following requirements [77, 78]:

- vertex of the event inside the restricted fiducial volume;
- visible event energy smaller than 30 GeV, in order to reduce the beam $\nu_e$ background;
- presence of a charged track starting directly from the vertex, fully consistent, over at least 8 wire hits, with a minimum ionizing particle, i.e. average dE/dx lower than 3.1 MeV/cm after removal of visible delta rays, and subsequently building up into a shower;
- visible spatial separation from other ionizing tracks within 150 mrad in the immediate proximity of the vertex in at least one of the two transverse views ($\pm$ 60°), except for short proton like recoils due to nuclear interactions.

The electron selection efficiency $\eta$ has been determined using a sample of MC $\nu_e$ events were generated according to the $\nu_\mu$ CC spectrum. A simulated event is shown in Fig. 2.4.
Out of an initial sample of 171 $\nu_\mu \rightarrow \nu_e$ reconstructed MC events, 146 events had a visible energy smaller than 30 GeV, 122 of which satisfy the fiducial volume cuts. These events were visually and independently examined by three

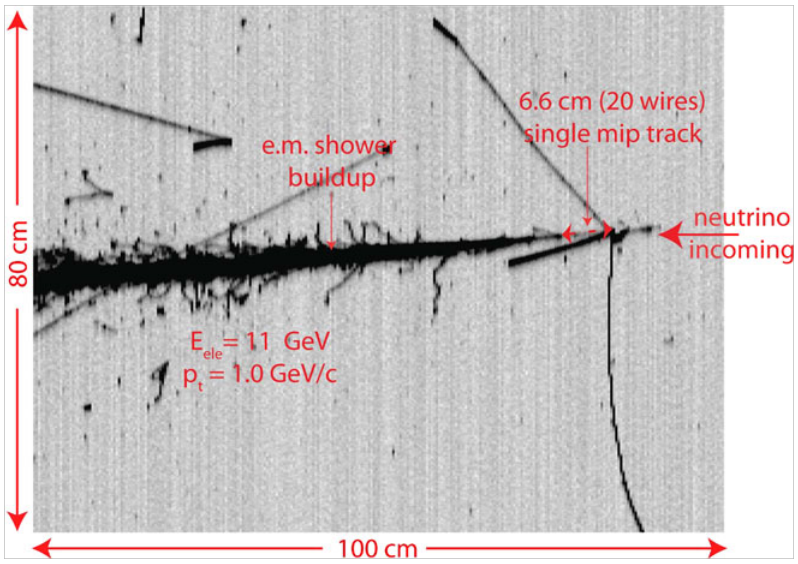


Figure 2.4: Typical Monte Carlo generated $\nu_e$ event with $E_e = 11$ GeV and $p_T = 1.0$ GeV/c [77].

different people, and an excellent agreement was found with differences in less than 3% of the sample. As a result, the average number of positively identified electron-like neutrino events was 90, corresponding to a selection efficiency $\eta = 0.74 \pm 0.05$.
The same analysis was carried out on a sample of 300 simulated event induced by the intrinsic $\nu_e$ contamination, giving the slightly lower value $\eta = 0.65 \pm 0.06$, as $\nu_e$ contamination events generate an harder spectrum than expected for the LNSD anomaly. An agreement better than 2.5% was found between the measured and the predicted scale of the dE/dx for muons in $\nu_\mu$ CC; then the systematic error on $\eta$, induced by the dE/dx cut, resulted to be smaller than 1%. A similar analysis on 800 MC neutral current events showed no presence of apparent $\nu_\mu \rightarrow \nu_e$ events, consistent with an estimated upper limit of 0.3 events, including possibly misidentified $\nu_\mu$ events [77, 78].
An example of real $\nu_e$ is shown in Fig. 2.5. The event has a total energy of $E_t = 11.5 \pm 2.0$ GeV and an electron induce e.m. shower of $E_{ele} = 10 \pm 1.8$ GeV, taking into account a partially missing component of the e.m. shower. The single electron shower in the transverse plane is opposite to the remaining of the event, with the electron transverse momentum of $1.8 \pm 0.4$ GeV/c. Fig. 2.6 displays the actual dE/dx of the electron shower along individual wires, in the region $\geq 4.5$ cm from primary vertex, where the track is well separated from other tracks and heavily ionizing nuclear prongs.
The expected number of $\nu_e$ events due to conventional sources in the energy range and fiducial volumes defined before and for the total analysed statistics was:

- $4.9 \pm 0.7$ events due to the estimated $\nu_e$ beam contamination;

- $2.2 \pm 0.4$ $\nu_e$ events due to the presence of $\theta_{13}$ oscillations from $\sin(\theta_{13}) = 0.0234 \pm 0.0020$ [79];

- $1.3 \pm 0.1$ $\nu_\tau$ with $\tau \to e$ from the three neutrino mixing standard model predictions [80],

giving a total of $8.4 \pm 1.1$ expected events, where the uncertainty on the NC and CC contaminations has been included and the selection efficiency reduction has been applied.
Given the smallness of the number of electron like signal expected in absence of LSND anomaly, the estimated systematic uncertainty on the predicted number is clearly negligible with respect to its statistical fluctuation. In the recorded experimental sample, 7 events, in which a $\nu_e$ signature have been identified, were found, to be compared with the above expectation of $8.4 \pm 1.1$ events from conventional sources [75]; the probability to observe a statistical under-fluctuation resulting in 7 or less $\nu_e$ events is $\simeq 33\%$.

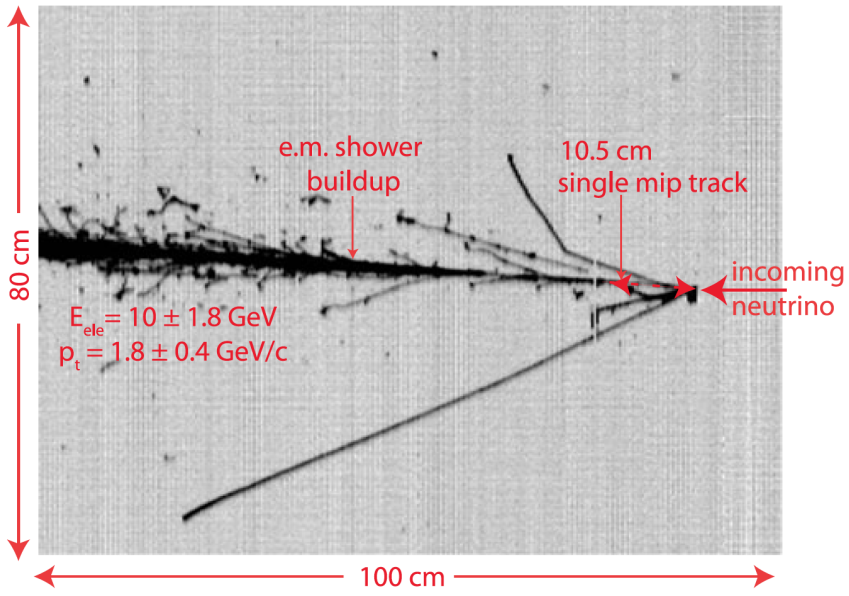


Figure 2.5: Picture of a real event with a clearly identified electron signature. Event has a total energy $E_t = 11.5 \pm 1.8$ GeV, and a transverse electron momentum $p_t = 1.8 \pm 0.4$ GeV/c. The single electron shower in the transverse plane is clearly opposite to the remaining of the event [77].

Within the range of ICARUS observations, the result is then compatible with the absence of a LSND anomaly. Following the statistical analysis of [81], at confidence levels of 90% and 99% and taking into account the detection efficiency $\eta$, the limits due to the LSND anomaly are respectively 5.7 and 11.4 events. According to the above described experimental sample and the number of recorded events, the corresponding limits on the oscillation probability

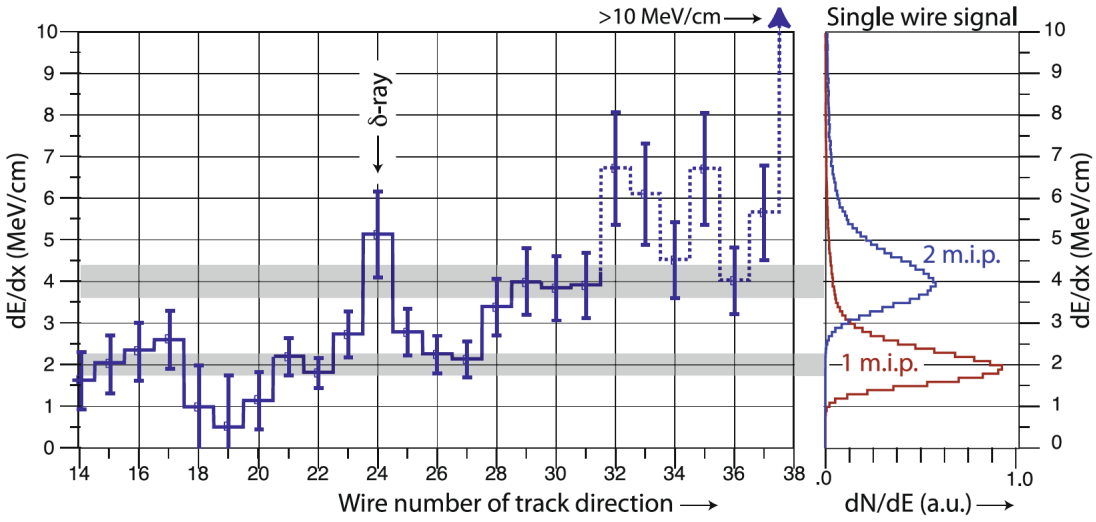


Figure 2.6: Display of the actual dE/dx along individual wires of the electron shower shown in Fig. 2.5, in the region $\geq 4.5$ cm from primary vertex, where the track is well separated from other tracks and heavily ionizing nuclear prongs. As a reference, the expected dE/dx distribution for single and double minimum ionizing tracks are displayed and the dE/dx evolution from single ionizing electron to shower is shown [77].

are $\langle P(\nu_\mu \to \nu_e)\rangle \leq 3.92 \times 10^{-3}$ and $\langle P(\nu_\mu \to \nu_e)\rangle \leq 7.83 \times 10^{-3}$, respectively. The exclusion area of the ICARUS experiment referred to neutrino-like events is shown in Fig. 2.7, in terms of the two dimensional plot of $\sin^2(2\theta_{new})$ and $\Delta m^2_{new}$ [75]. The same region has been expanded by successive results by OPERA [83], that operated with the same CNGS beam as ICARUS (see Fig. 1.1) and IceCube [84].
In the interval $\Delta m^2_{new} \simeq 0.1$ eV$^2$ to $\Delta m^2_{new} > 10$ eV$^2$ the exclusion area is independent from $\Delta m^2_{new}$ with $\sin^2(2\theta_{new}) = 2.0\langle P(\nu_\mu \to \nu_e)\rangle$. In the $\Delta m^2_{new}$ interval from $\simeq 0.1$ eV$^2$ to $\simeq 0.01$ eV$^2$, the oscillation is progressively growing and averages to about the above value of twice $\langle P(\nu_\mu \to \nu_e)\rangle$. For even lower values of $\Delta m^2_{new}$, the longer baseline strongly enhances the oscillation probability with respect to the one of the previous short baseline experiments.

### Antineutrino analysis

The LSND result was based on antineutrino events. A small $\simeq 2\%$ antineutrino event contamination is also present in the CNGS beam as experimentally observed [82].
According to a detailed neutrino beam calculation, the $\overline{\nu}_\mu$ CC event fraction is $(1.2 \pm 0.25)\%$ for $E_\nu < 30$ GeV, where a 20% uncertainty has been conservatively assumed. In the limiting case in which the whole effect is due to $\overline{\nu}_\mu \to \overline{\nu}_e$, the absence of an anomalous signal registered gives a limit of 4.2 events at 90% CL. The corresponding limit on the oscillation probability is

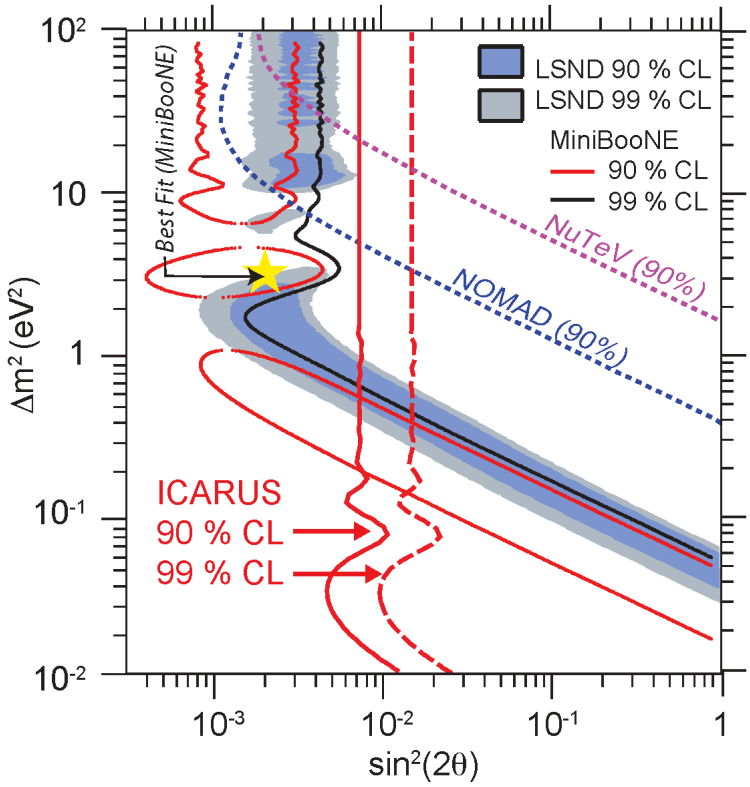


Figure 2.7: Two dimensional plot with $\Delta m^2$ as a function of $\sin^2(2\theta)$ for the main experiments sensitive to the $\nu_\mu \to \nu_e$ anomalies and for the present ICARUS result (continuous red lines). The ICARUS limit on the $\nu_\mu \to \nu_e$ oscillation probability are $\langle P(\nu_\mu \to \nu_e)\rangle \leq 3.92 \times 10^{-3}$ and $\langle P(\nu_\mu \to \nu_e)\rangle \leq 7.83 \times 10^{-3}$ at 90% and 99% CL.

$\langle P(\overline{\nu}_\mu \to \overline{\nu}_e)\rangle \leq 0.32$. The resulting (small) exclusion area is shown in Fig. 2.8.

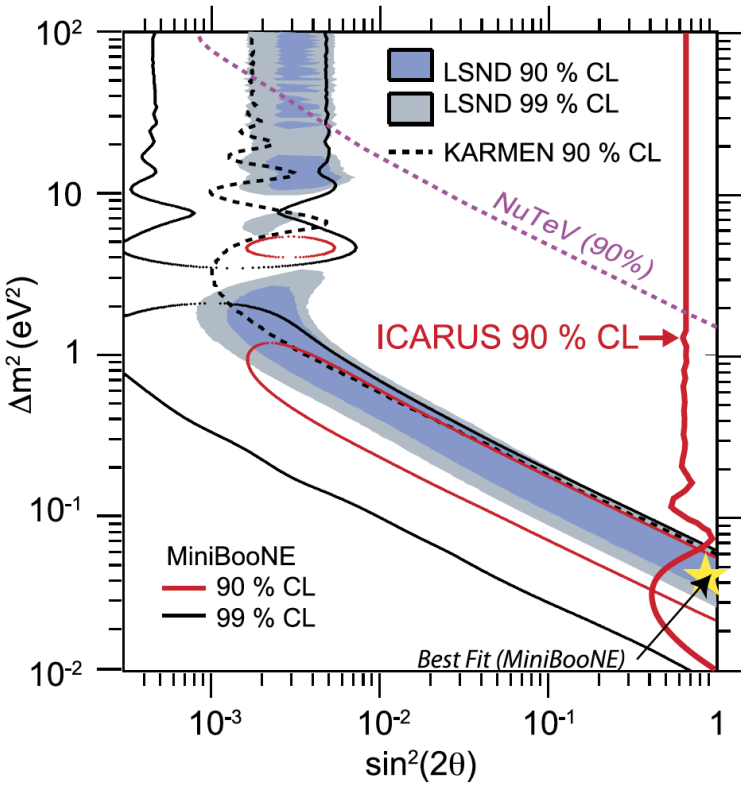


Figure 2.8: Two dimensional plot with $\Delta m^2$ as a function of $\sin^2(2\theta)$ for the main experiments sensitive to the $\overline{\nu}_\mu \to \overline{\nu}_e$ anomalies and for the present ICARUS result (continuous red lines). The ICARUS limit on the $\overline{\nu}_\mu \to \overline{\nu}_e$ oscillation probability is $\langle P(\overline{\nu}_\mu \to \overline{\nu}_e)\rangle \leq 0.32$ at 90% CL .

## 2.3 Short Baseline Neutrino program

A new experimental phase of the ICARUS T600 detector will foresee its employment at Fermi National Laboratory (FNAL), where it will be part of the Short Baseline Neutrino (SBN) program [87].
SBN program scientific purpose is a $\sim 5\sigma$ confidence level analysis of the possible sterile neutrino existence in the parameter space suggested by LSND (see Chap. 1), by precisely and independently measuring both $\nu_e$ appearance and $\nu_{mu}$ disappearance oscillation channels, assuming the three years of data taking. It is proposed to include three LAr-TPC detectors located at different on-axis position along the Booster Neutrino Beam (BNB), as shown in Fig. 2.9. The near one (SBND) will be located at 110 m from the BNB target while the MicroBooNE apparatus will be located at 470 m. The far detector will be the improved ICARUS-T600, located at 600 m from the BNB target.
The different locations have been chosen to optimise sensitivity to neutrino

oscillations and to minimize the impact of flux systematic uncertainties. The ICARUS T600 detector will provide the signal for the LSND-like oscillation analysis, while the existing MicroBooNE detector will investigate the source of unexplained excess of low energy electromagnetic events observed in MiniBooNE. The role of the near detector will be to precisely measure the unoscillated neutrino flux, to significantly reduce systematical errors on prediction of expected neutrino flux in the far sites: in case of absence of LSND anomaly, the three detector signals should be a copy of each other for all experimental signature. A summary of the three detectors locations and masses can be found in Tab. 2.3.

| Detector | Distance from BNB Target | LAr Total Mass | LAr Active Mass |
|---|---|---|---|
| SBND | 110 m | 220 t | 112 t |
| MicroBooNE | 470 m | 170 t | 89 t |
| T600 | 600 m | 760 t | 476 t |

Table 2.3: Summary of the SBN detector locations and masses (total LAr masses and active ones).

### 2.3.1 The Booster Neutrino Beam

The Booster Neutrino Beam (BNB) is created by extracting protons from the Booster accelerator with momentum $p = 8.89$ GeV/c and impacting them on a $1.7\lambda$ beryllium target to produce a secondary beam of hadrons, mainly pions. Charged secondaries are focused by a single toroidal aluminium alloy focusing horn that surrounds the target. The horn is supplied with 174 kA in 143 $\mu$s pulses coincident with proton delivery. The horn can be pulsed with either polarity, thus focusing either positive or negative particles and de-focusing the other. Focused mesons are allowed to propagate down a 50 m long, 0.91 m radius air-filled tunnel where the majority will decay to produce muon and electron neutrinos. The remainder are absorbed into a concrete and steel absorber at the end of the 50 m decay region. Suspended above the decay region, at 25 m, are concrete and steel plates which can be deployed to reduce the available decay length, thus systematically altering the neutrino fluxes.
The Booster spill length is 1.6 $\mu$s with nominally $\sim 5 \times 10^{12}$ protons per spill delivered to the beryllium target. The main Booster RF is operated at 52.8 MHz, with 81 buckets filled out of 84. The beam is extracted into the BNB using a fast-rising kicker that extracts all of the particles in a single turn. The resulting structure is a series of 81 bunches of protons each $\sim 2$ ns wide and 19 ns apart. While the total operating rate of the Booster is 15 Hz, the maximum allowable average spill delivery rate to the BNB is 5 Hz, set by the design of the horn and its power supply.
The composition of the flux in neutrino mode (focusing positive hadrons) is energy dependent, but is dominated by $\nu_\mu$ ($\sim 93.6\%$), followed by $\overline{\nu}_\mu$ ($\sim 5.9\%$),

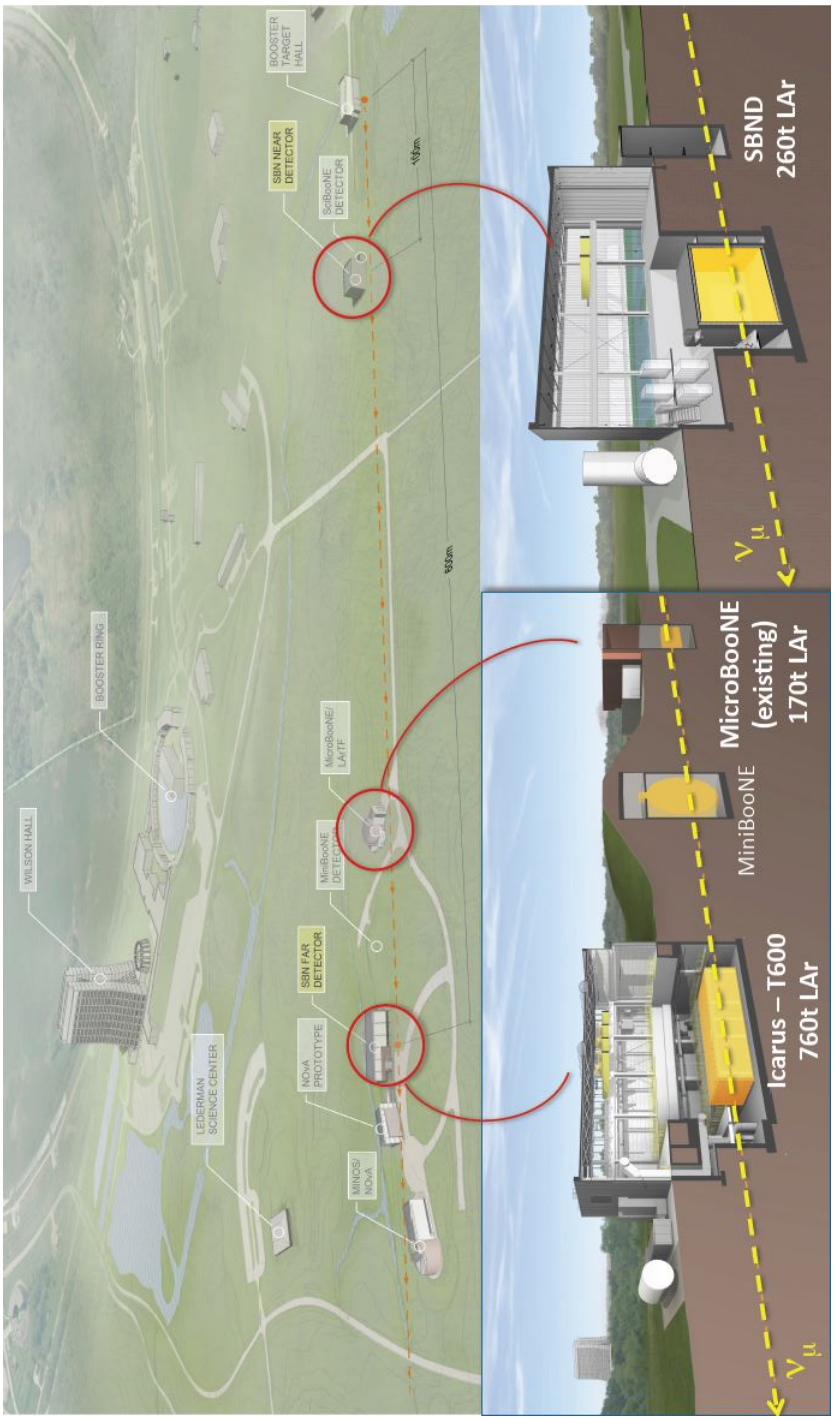


Figure 2.9: Map of the Fermilab neutrino beam line area showing the axis of the BNB (red dashed line) and approximate locations of the SBN detectors at 110 m, 470 m and 600 m. The detectors locations are also depicted.

with an intrinsic $\nu_e/\overline{\nu}_e$ contamination at the level of 0.5% at energies below 1.5 GeV.
Neutrino energy is peaked at ∼1 GeV, with tail till to 3 GeV.
The majority of the $\nu_\mu$ flux originates from pion decay in flight, except above ∼ 2 GeV where charged kaon decay is the largest contributor. A substantial portion of the intrinsic $\nu_e$ flux, 51%, originates from the pion to muon decay chain, with the remaining portion from $K^+$ and $K^0$ decays [87].

### 2.3.2 SBND

The Short Baseline Near Detector (SBND) [87] will house a CPA (Cathode Plane Assembly) and four APAs (Anode Plane Assemblies) to read out ionization electron signals (see Fig. 2.10). The active TPC volume will be 4.0 m × 4.0 m × 5.0 m, containing 112 tons of LAr. The two APAs located near the beam-left and beam-right walls of the cryostat will each hold 3 planes of wires with 3 mm wire spacing. TPC signals will be read out with banks of cold electronics boards placed at the top and on the two outside edges of the frame. The total number of readout channels will be 2816 per APA (11264 in the entire detector). The CPA will have the same dimensions as the APAs and it will be centred between them. It will be made of a stainless-steel framework, with an array of stainless steel sheets mounted over the frame openings. Each pair of facing CPA and APA hence will form an electron-drift region. The open sides between each APA and the CPA will be surrounded by 4 FCAs (Field Cage Assemblies), constructed from FR4 printed circuit panels with parallel copper strips, to create a uniform drift field. The drift distance between each APA and the CPA will be 2 m, such that the cathode plane will need to be biased at -100 kV for a nominal 500 V/cm field. The SBND design will additionally include a light collection system for detecting scintillation light produced in the LAr volume.

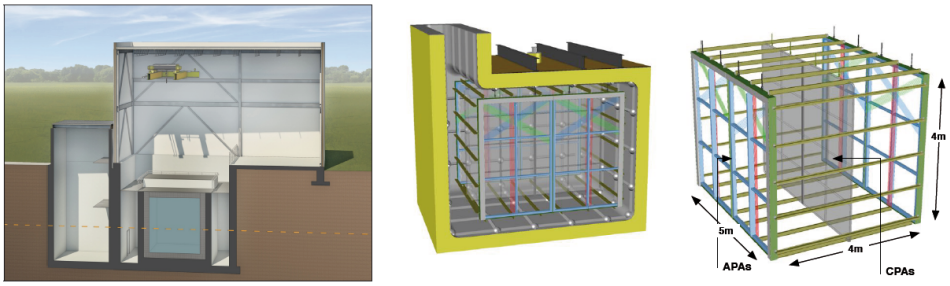


Figure 2.10: (Left) The SBND detector building concept. The neutrino beam centre is indicated by the orange dashed line and enters from the left. (Right) The SBND TPC conceptual design.

### 2.3.3 MicroBooNE

The Micro Booster Neutrino Experiment (MicroBooNE) [85] detector is a 170 ton total mass (89 ton active mass) LAr TPC contained within a conventional cryostat. It started the data taking in October 2015, as stand alone detector, to verify the excess of $\nu_e$ induced events in LSND and MiniBooNE data and to measure low energy neutrino cross section.
The active region of the TPC is a rectangular volume of dimensions 2.33 m $\times$ 2.56 m $\times$ 10.37 m (see Fig. 2.11). The TPC cathode plane forms the vertical boundary of the active volume on the left side of the detector when viewed along the neutrino beam direction (beam left side). The MicroBooNE TPC design allows ionization electrons from charged particle tracks in the active liquid argon volume to drift up to 2.56 m to a three-plane wire chamber. Three readout planes, spaced by 3 mm, form the beam right side of the detector, with 3456 wires arrayed vertically and two planes of 2400 wires oriented at $\pm$60 degrees with respect to vertical. An array of 32 PMTs are mounted behind the wire planes on the beam right side of the detector to collect prompt scintillation light produced in LAr.

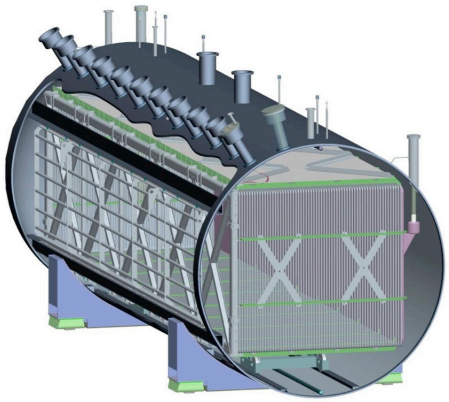

Figure 2.11: The MicroBooNE detector. The high-voltage feedthrough enters on the right and supplies the voltage for the cathode plane. One side of the field cage can be seen on the face of the cut-away (supported by the X braces). The sense and induction wires are on the right, and behind them is the support structure for the PMT array.

### 2.3.4 ICARUS T600 at FNAL

Once moved to FNAL, the ICARUS T600 detector will be placed at a distance of 600 m from the target of the BNB, on-axis (see Fig. 2.9).
The T600 detector was designed for the low background, deep underground conditions of LNGS laboratory, where the single prompt trigger has always ensured the unique timing connection to the main image of the event. However, the situation at FNAL will be substantially different for a detector of this size

if placed at shallow depth, i.e. a few meters deep under a 3 m concrete cup to shield the soft cosmic radiation (see Fig. 2.12): several additional and uncorrelated tracks, due to cosmic rays, will be generally occurring continuously and at different times during the $\sim$ 1 ms duration of the T600 readout window. This represents a new problem since, to reconstruct the true position of the track, it is necessary to precisely associate the different timings of each element of the image to their own specific delay with respect to the trigger. For this reason, an overhauling is necessary in order to deal with the new experimental conditions and background.

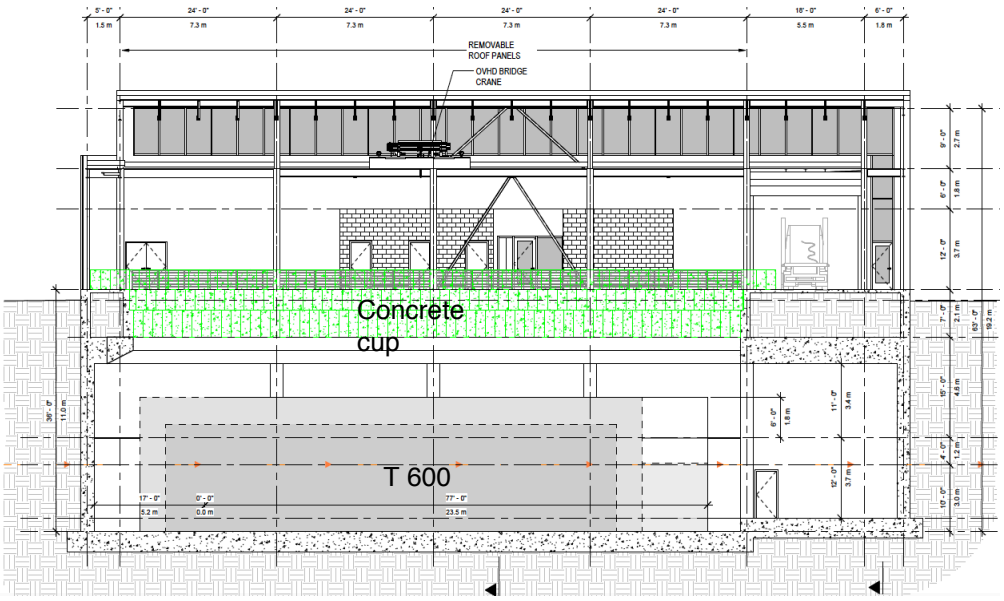


Figure 2.12: Scheme of ICARUS-T600 detector building. The 3 m concrete cup is enlightened in green. The neutrino beam centre is indicated by the orange dashed line and enters from the left.

The specific investigation of the oscillation anomalies at shallow depths is based on the search of a signal with the presence of a neutrino-induced, single ionizing electron (or positron). High energy cosmic muons, creating secondary showers, may also produce single ionizing background electrons or positrons with similar energies. At the neutrino energies of the FNAL BNB ($\sim$ GeV), the intrinsic $\nu_e$ CC contamination occurs at the very low rate of $\sim$ 500 $\nu_e$ CC/y, while a possible LSND-like oscillation signal will produce a few hundred $\nu_e$ CC/y. On the other hand the cosmic ray background is very prolific of events: in a pit covered by 3 m of concrete, i.e. the condition of T600 at FNAL, cosmic muon rates in coincidence with the beam trigger window of 1.6 $\mu$s, will produce the huge rate of 0.83 $\times$ $10^6$ cosmics per year (c/y) [87]. During the 1 ms long duration of each readout window, $\sim$ 12 cosmic ray tracks are expected over the full T600, in agreement with the ICARUS measurements at surface carried out in 2001 test run [64]. It can be concluded that in its original configuration the ICARUS LAr TPC detector can not perform a practical search for LSND-

like anomalies at shallow depths, since the cosmic trigger events are too much frequent.
To overcame this problem, a complete overhauling of the ICARUS T600 detector is ongoing at CERN with the project name WA104 [88]. During this refurbishing, most of the existing operational equipment will be preserved, while some components are being upgraded with up-to-date technology in view of future non-underground operation.
The refurbishing include the following main activities:

- implementation of a new light collection system, to allow a more precise event localization and disentangle beam events from the background induced by cosmic rays;
- implementation of new readout electronics;
- implementation of new trigger and DAQ system;
- substitution of the present cathodes with new ones of improved planarity;
- other internal TPC updating: slow control system and cabling;
- realisation of new vessels for LAr containment and new thermal insulation;
- complete review and maintenance of the cryogenics and purification systems;

The realisation of a Cosmic Ray Tagger (CRT) system, external to the LAr fiducial volume, is also foreseen, to identify entering charged tracks with position and timing information: this would facilitate the reconstruction and identification of cosmic muon tracks entering in the detector [87].
According to the present status of the overhauling plan, the two T300 modules are expected to arrive at FNAL at the beginning 2017 for the installation in the new hall, followed by the commissioning, the preparation and activation of DAQ and trigger to start the data taking [88].

### New light collection system

The future operation of the T600 detector requires an improved light collection system, able to detect with full efficiency the prompt scintillation light from events with energy depositions down to $\simeq 100$ MeV. The renovated T600 photodetector arrangement should again collect the VUV scintillation signal which is present in the LAr simultaneously to the ionization, converting it to visible light.
Due to cosmic rays background, the new light collection system has to be able also to localize the track associated with every light pulse along the 20 m of the longitudinal detector direction, with an accuracy better than 1 m, which

is smaller than the expected average spacing between cosmic muons in each TPC image. In this way, the light collection system would be able to provide unambiguously the absolute timing for each track; and to identify, among the several tracks in the LAr-TPC image, the event in coincidence with the neutrino beam spill. The time accuracy of the incoming event with the new light collection system is expected to be at 1 ns level, allowing the exploitation of the bunched beam structure, lasting 1.15 ns (FWHM $\sim$ 2.7 ns) every 19 ns, to reject cosmic events out of bunch [86] and also a first discrimination of event topology [89].
The T600 light detection system upgrade is based on a total of 360 PMTs, 8 in. diameter, Hamamatsu R5912-MOD, corresponding to 90 PMTs behind each wire chamber (the layout is shown in Fig. 2.13). The PMTs were tested before the installation in the T600, in order to verify their compliance with the required functioning specifications. Then they were coated with the TPB. All PMTs for the first T300 module have been installed, as shown in Fig. 2.14 [88].

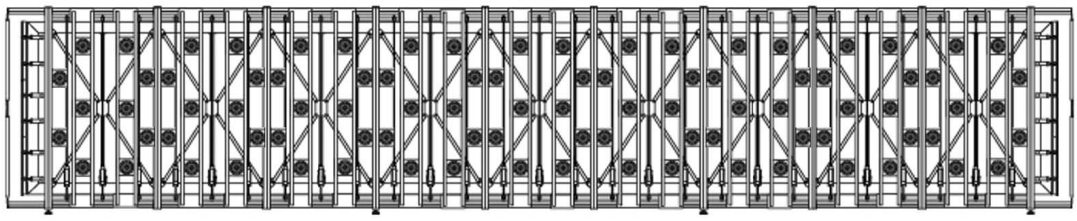

Figure 2.13: The drawing shows the 90-PMTs layout behind the wire planes. PMTs are depicted as dark circles.The coverage area corresponds to 5% of the wire plane surface [89].

**New readout electronics**

The present ICARUS T600 electronics was designed starting from an analogue low noise warm front-end amplifier followed by a multiplexed (16 to 1) 10-bit A/D converter and by a digital VME module that provided local storage, data compression and trigger information. The analogue front-end amplifier, used in the T600 LNGS configuration, is perfectly adequate: the only change will be the adoption of a smaller package for the BiCMOS custom dual channel amplifier. A relevant change concerns the adoption of serial ADCs (one per channel) instead of the multiplexed ones used at LNGS. The main advantage is the synchronous sampling time (400 ns) of all channels of the whole detector. Performance, in terms of throughput of the read-out system, will be improved replacing the VME (8-10 MB/s) and the sequential access inherent to the shared bus architecture, with a modern switched I/O. Such I/O transaction is carried over optical Gigabit/s serial links [87]

Figure 2.14: Picture of PMTs installed in the first T300 module.

### Trigger and DAQ

The trigger system of the T600 detector will exploit the coincidence of the prompt signals from the scintillation light in the LAr TPC, recorded by the PMT system, with the proton spill extraction of the BNB within a 1.6 $\mu$s gate. PMT signal will be acquired and digitized by CAEN V1730 boards,with 500 MHz sampling frequency. PMT digitized pulses will be processed by FPGA modules, requiring a logic on multiple PMT signals for the generation of the trigger. The PMT trigger signal will be then sent to the T600 Trigger Manager, where it will be combined with the time information from the beam spill to initiate the readout of all the TPCs. A multi-buffer event recording will be adopted with a 3-level veto, as in the case of the CNGS beam exploitation, able to give different priorities to different trigger sources, thus minimizing DAQ dead-time [87]. A continuous communication between trigger and DAQ (see Fig. 2.15) will prevent the generation of new triggers in case the detector is busy, while a multi-veto configuration will minimise dead-time. A common clock, synchronized with the BNB, will be shared among TPC, PMT and CRT to guarantee the ns level relative timing needed to exploit the fine bunched beam structure [88].

### TPC updates

For what concerns the T600 TPC internal structure, minor changes are being implemented. Small deviations from the linearity of the drift field have been found in the region close to the cathode plane on both modules. This is due to

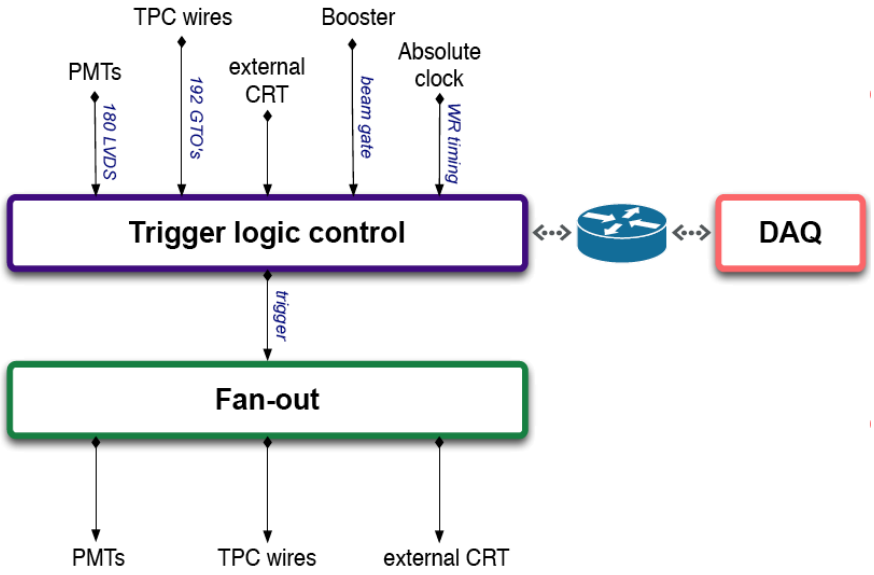


Figure 2.15: Scheme of the trigger and DAQ system.

the not perfect planarity of the cathodes, owing to their pierced structure. It has been decided to restore the present cathodes improving their planarity with a thermal treatment, including local pressing and heating. This mechanical intervention has been concluded with success for the first T300 module [88] and the panels have been reinstalled in the detector (see Fig. 2.16) after suitable cleaning (electro-polished).
Other activities on the T600 TPCs concern the updating of the slow control system for temperature, pressure and cryostat wall deformation monitor, as well as the design of new cabling for internal wires, PMTs and slow control sensors [87].

### New cryogenic and purification systems

New cryostats will host the refurbished T600 detector. LAr will be contained in two mechanically independent vessels, of about 270 $m^3$ each. They will be parallelepipedal in shape with internal dimensions 3.6 m $\times$ 3.9 m $\times$ 19.6 m. Aluminium welded extruded profiles will be used: they are requested to be high vacuum tight and to stand a 1.5 bar maximal operating internal overpressure. Use of aluminium LAr vessels is particularly attractive as it offers very good shielding against external electronic noises, and it provides large thermal conductivity that improves the temperature uniformity inside the LAr. Walls will be double-layered and with the possibility to be evacuated, leading to efficient leak detection and repair. The cold vessels will be enclosed inside a common heat exchanger (thermal shield) in which two-phase, gas and liquid, nitrogen will be circulated. As in the past run, a mass ratio less than 5:1 will be kept between the liquid and the gas phases, which ensures temperature uniformity

Figure 2.16: Cathode panels after flattening, cleaning and reinstallation for the first T300 module.

all along the shield. The first T300 module cold vessel is in advance stage of final assembly, as shown in Fig. 2.17 [88]. The scheme of ICARUS T600 cryogenics and LAr purification systems will be mainly preserved, with the difference that the cooling circuit will be operated in open loop, instead of using re-liquefaction [87].

### Cosmic Ray Tagger system

At shallow depth conditions, the detector will be exposed to high cosmic ray flux: a segmented, fast anti-coincidence with $4\pi$ coverage detector (Cosmic Ray Tagger, CRT), may record each charged particle crossing the outer boundaries of the LAr volume. The positions and the timings of all muon tracks crossing the walls of the CRT during the T600 imaging window will be recorded. Each muon track reconstructed in the TPC may be then correctly determined by associating the charge image with the corresponding absolute drift time $t_0$ coming both from the CRT and from the internal light collection system, matching the track geometry with the CRT recorded positions. This would be achieved by means of a system which provides signals, independently from the LAr-TPC and the light collection system, that indicate the passage of charged particles through the surface of the LAr sensitive volume. These signals would be used as anti-coincidence to identify and recognise the interactions generated by ex-

Figure 2.17: First cold vessel in the present stage of assembly at CERN. In this picture, the top part of the vessel, already completely assembled, lies on the bottom.

ternal particles [87]. The CRT will be realised by plastic scintillation counters read-out by Silicon PhotoMultipliers [88].

Chapter 3

# Reconstruction of events in ICARUS

Charged particles crossing the LAr sensitive volume of the ICARUS T600 produce ionization electrons and scintillation light along their path, in a number proportional to the energy transferred from the particle to the LAr.
The ionization electrons drift with a constant speed in a uniform electric field toward the anode, that is composed of three wire planes, as shown in Fig. 3.1(a).
The goal of the reconstruction procedure is to extract the physical information contained in the wire output signal, i.e. the energy deposited by the different particles and the point where the deposition occurred, to build a complete 3D spatial and calorimetric picture of the event.
The signal is induced in a non-destructive way on the first two wire planes, *Induction1* and *Induction2*, which are practically transparent to the drifting electrons. The signal on the third wire plane, *Collection*, is instead formed by collecting the ionization charge, which is also the source of the calorimetric measurement. Different orientation of the wires in the anodic planes (0° , +60° , -60° with respect to the horizontal, with 3 mm wire spacing in each plane) allows localization of the signal source in the $xz$ plane, as shown in Fig 3.1(b). The distance from the wire planes, i.e. the $y$ coordinate, is calculated from the wire signal timing and the electron drift velocity. The absolute event timing, $t_0$, is provided by the prompt signal from the photomultipliers collecting the scintillation light.
Wire signals are amplified and digitized with 400 ns sampling time which results in 0.64 mm spatial resolution along the drift coordinate using a 500 V/cm electric field.
Finally, digitized waveforms from consecutive wires form 2D projection images of an event, like the example of CNGS neutrino interaction in Fig. 3.2.
The basic energy deposition unit is the *hit*, defined as the segment of track whose energy is read by a given wire. Therefore, the hits contain the spatial and calorimetric information of the track segment, and are the basis of the

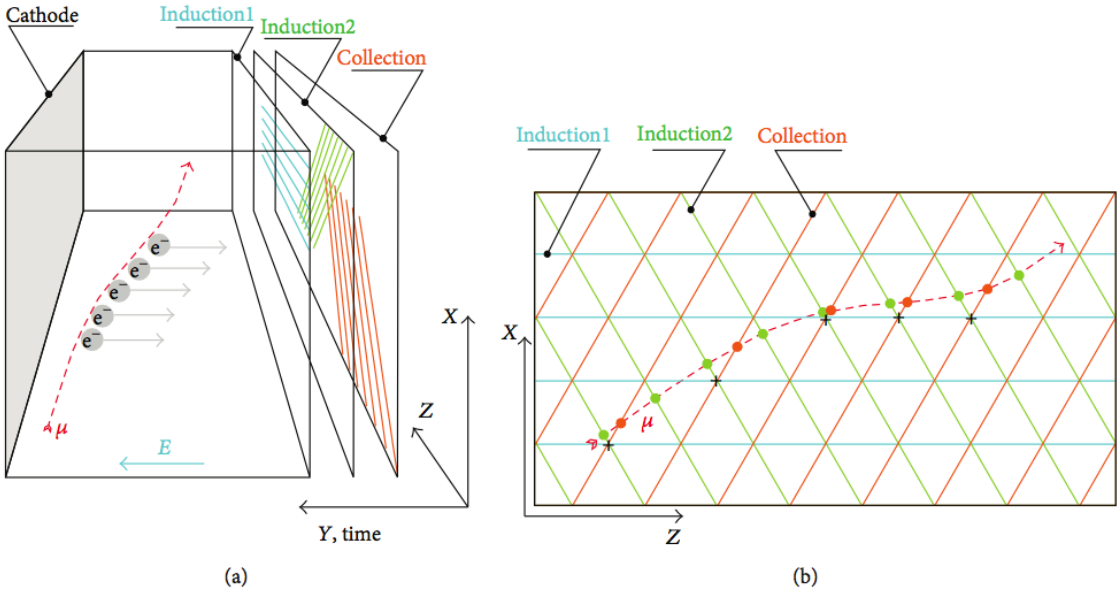


Figure 3.1: Schematic view of the ICARUS T600 readout principle; one of four TPCs is shown: (a) 3D view with marked $\mu$ track (red) and the ionization electrons $e^-$ drifting in the electric field $E$ toward the readout wire planes; (b) the $xz$ projection with marked actual intersections of the particle track and readout wires (green and orange points) and an example of points on the reconstructed track that may be obtained by associating wire signals from Induction2 and Collection planes using drift timing (black crosses).

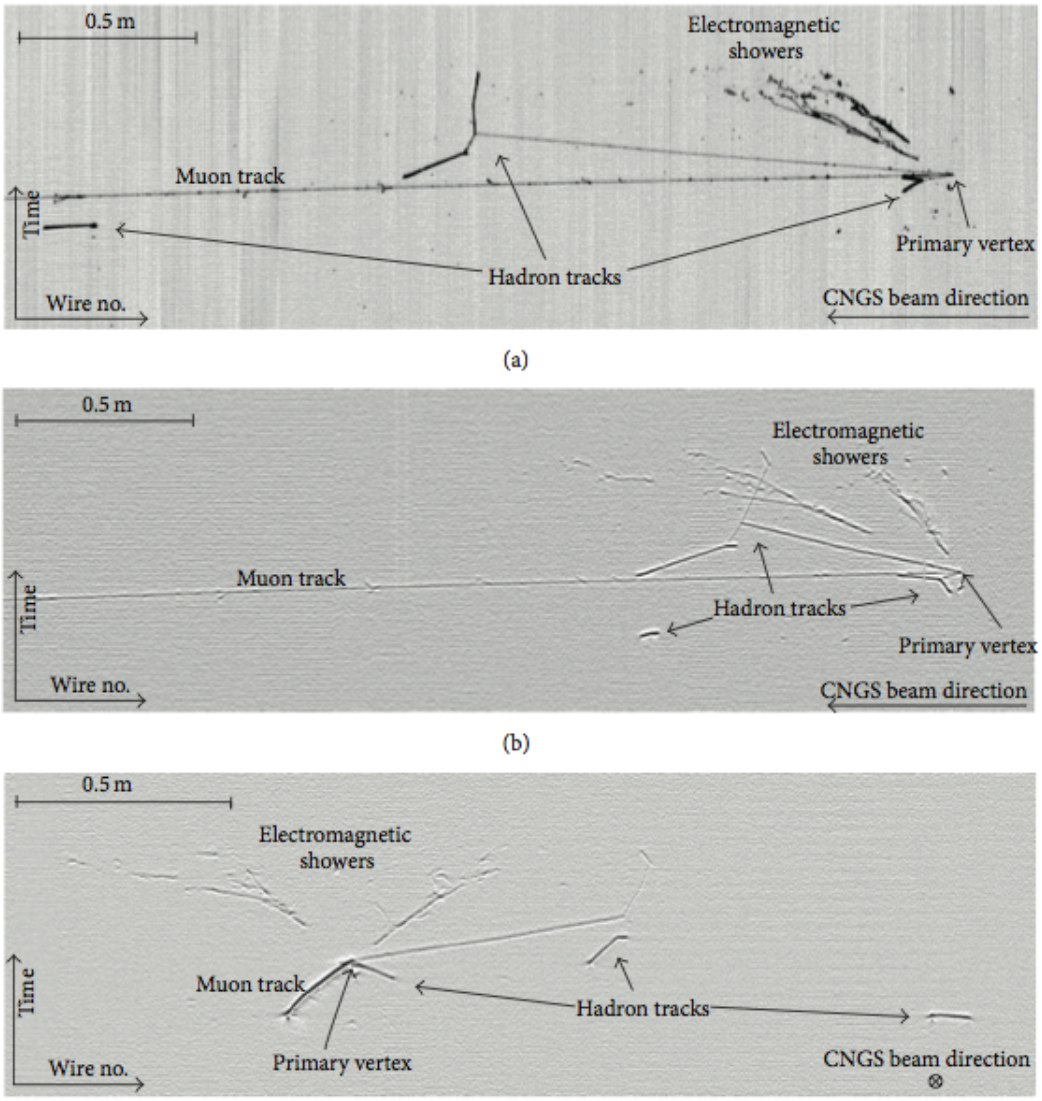


Figure 3.2: Example of real CNGS $\nu_\mu$ charge current interaction in one of the T300 module, as seen in the three different wire planes: (a) Collection plane; (b) Induction2 plane; (c) Induction1 plane. The horizontal wires of the Induction1 plane form the projection on $xy$ plane and give the frontal view of the event while the Collection and Induction1 planes form $yz$ projections and give the top views of the event seen at two different angles. Particles involved in this interaction are enlightened.

reconstruction procedure.
The reconstruction of an event is divided into several steps realised with independent algorithms[76, 64]:

1. **hit reconstruction**: the hits are independently searched for in every wire. They are defined as signal regions of a certain width above a baseline value. In this step also the parameters which contain the physical information are determined;

2. **2D cluster reconstruction**: hits are grouped into common charge deposition distributions based on their position in the plane to form 2D structures;

3. **3D reconstruction**: three dimensional objects are reconstructed using 2D hit clusters associated in at least two wire planes.

These algorithms are implemented in the ICARUS data processing software library. The ICARUS Collaboration developed an analysis framework, called `Qscan`, that permits the graphical visualization and the full reconstruction of events. An example of how `Qscan` looks like, is the Fig. 3.3.

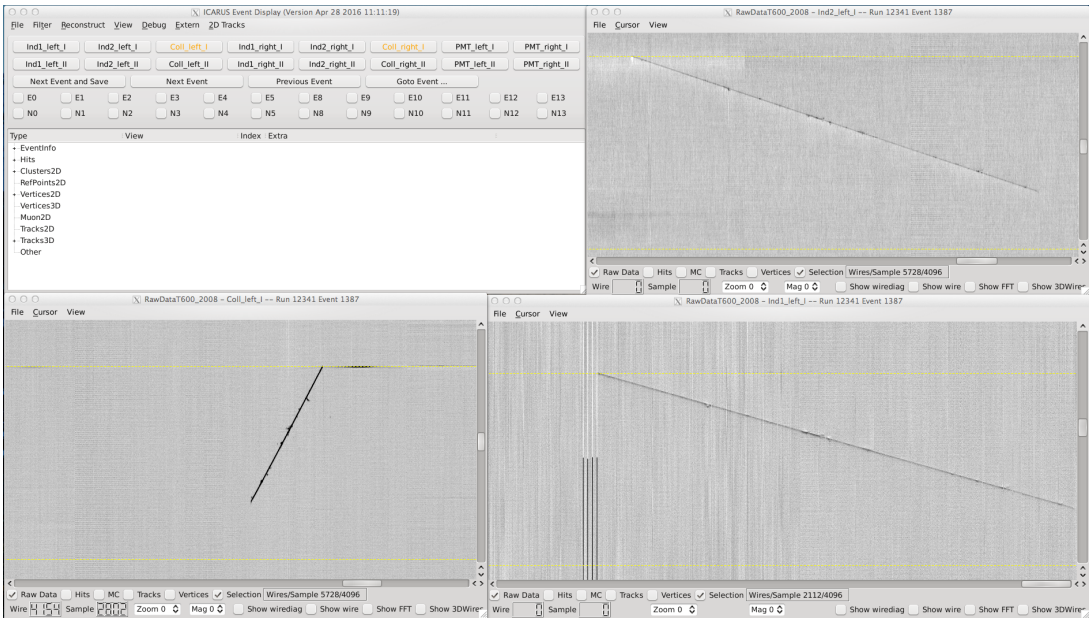

Figure 3.3: Event visualization using the `Qscan` graphical interface: the main `Qscan` window (top left) and the three event views.

## 3.1 Hit reconstruction

The essential element for the spatial and calorimetric measurements is the hit. The hit identification aims to distinguishing signals produced by ionization

electrons from electronic noise and it is based on geometrical features of the wire output signal in a given region, i.e. the presence of a relatively broad region of signal values above an appropriate threshold.
The search algorithm loops over the whole wire plane, skipping those wires with signal identification problems. It includes some free parameters different for each wire plane.

Each signal sample is compared to its *local mean*, i.e. the *baseline* of the signal. A value above the local mean by more than *threshold* ADC counts, triggers a hit candidate. The hit candidate is built with all the subsequent signal samples above the threshold and is characterized by its *width*, defined as the duration (in drift samples) between the hit starting and ending points. Rejection of fake (noise) candidates is achieved by imposing a minimal width value. Further rejection can be carried out for Collection and Induction1 wires, where the hits are expected to have an exponential falling slope. Therefore, an extra requirement on the minimum duration from the peak position to the hit end (represented with the *fall* parameter) is imposed.
Once the hit has been detected, its reconstruction is performed with the aim of extracting the parameters defining the hit (position, height, area) which contain the physical information of the original associated track segment. The hit spatial reconstruction is entirely based on the determined hit peak position, whereas the hit area in Collection wires is proportional to the energy deposited by the ionizing particle, and therefore constitutes the base of the calorimetric reconstruction.
In this second stage of the algorithm, hits are fitted with a functional form, assuming a model of the readout electronics. Single hit, related to a particle track crossing the wire, is represented with a function $p(t)$, above the baseline $B$, which is assumed as [91] :

$$p(t) = A\frac{e^{-(t-t_0)/\tau_1}}{(1+e^{-(t-t_0)/\tau_2})}, \tag{3.1}$$

where $A$ is the hit amplitude, $t_0$ is the time shift within the fit window and $\tau_1$ and $\tau_2$ are the rising and falling time constants, respectively. The parameters included in the fit function are represented in Fig. 3.4 and its representation is in Fig. 3.5. The wire signal in real data conditions may contains hits originating from many particles tracks. Wire signal corresponding to such a configuration may be represented by a sequence of $N_p$ hits. Therefore, the general fit function is:

$$f(t) = B + \sum_{i}^{N_p} A_i\frac{e^{-(t-t_{0i})/\tau_1}}{(1+e^{-(t-t_{0i})/\tau_2})}, \tag{3.2}$$

where $B$ is again the baseline level and $i$ indicates the $i$-th hit recorded on that wire.

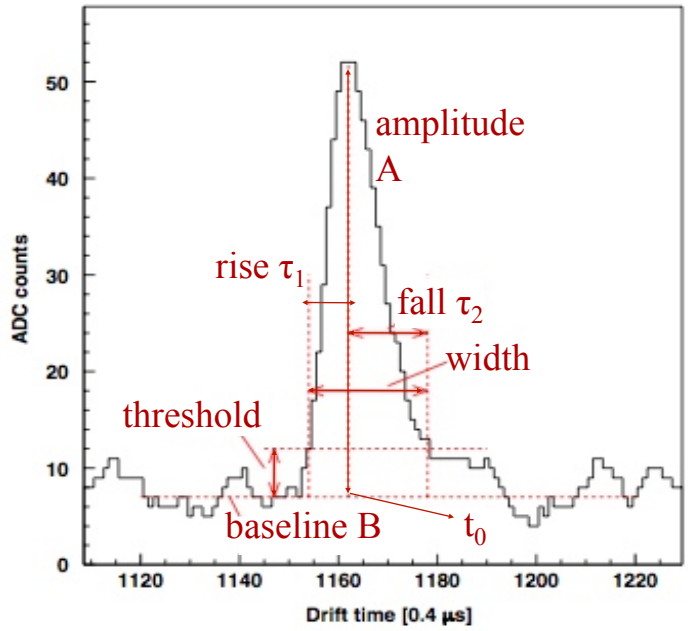


Figure 3.4: Example of a hit produced by a minimum ionizing particle on a Collection wire; parameters involved in the hit finding and in the fit function are marked.

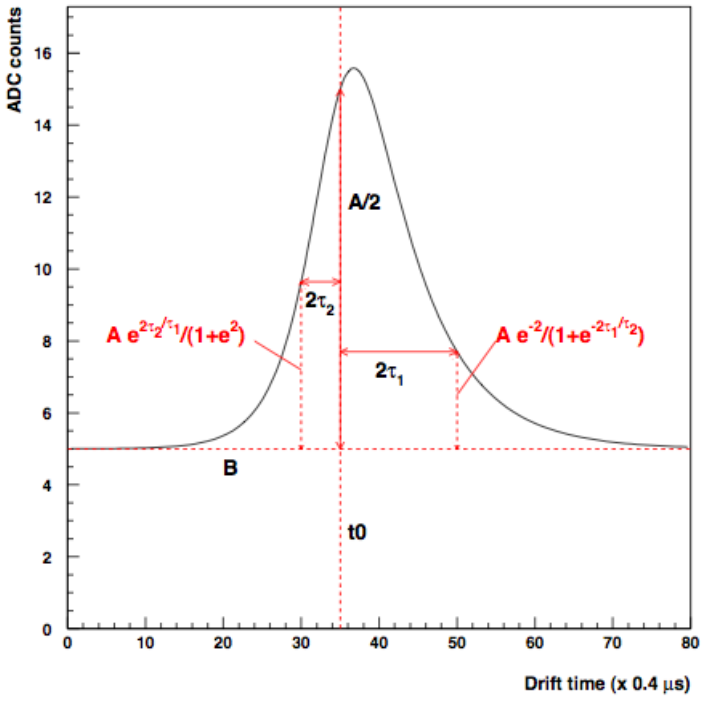


Figure 3.5: Function used in the hit fit (see Eq. 3.2) for only one hit, considering the following parameters as example: $B = 5$ ADC counts, $A = 20$ ADC counts, $t_0 = 14$ $\mu$s, $\tau_1 = 3$ $\mu$s and $\tau_2 = 1$ $\mu$s.

This improves the hit positioning, resolves overlapping hits and allows the reconstruction of the individual hit energy deposits, as we can see in the Fig. 3.6. Using the fit function in Eq. 3.2, hits with adjacent drift time windows form a group that is fitted as it would be for a single window.

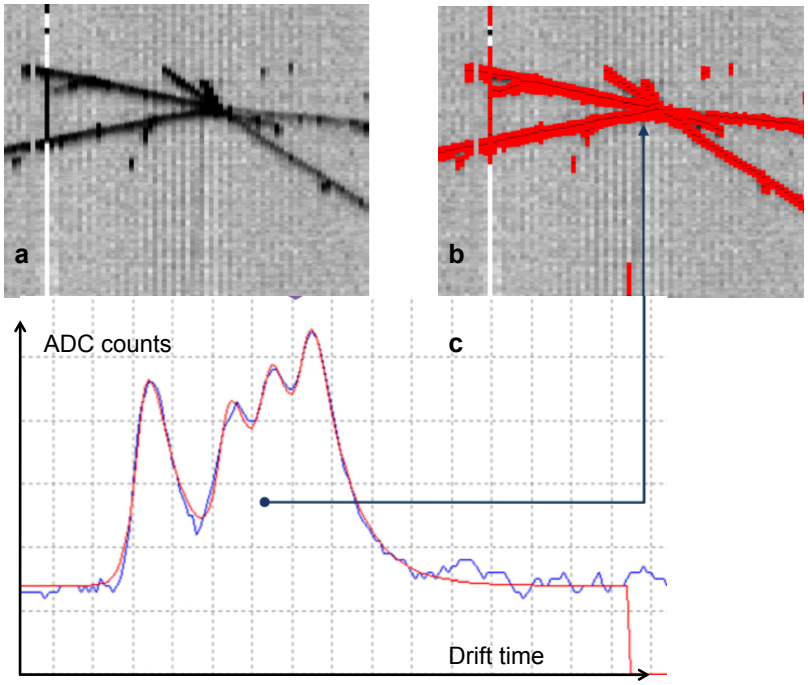


Figure 3.6: Example of many tracks on one wire, typically in the vertex region (a); (b) hits identified by the hit finding procedure; (c) signal recorded by the wire (blu line) and the resulting fit (red line). In this case, the singal is due to the sum of four independent hits.

The fit parameter values and the number of hits $N_p$, are iteratively optimised to minimize $\chi^2$ using the MINUIT [92] package. Hits $p_i(t)$resulting from the optimization procedure, become the new hits that replace those initially found at the first stage hit identification. The positions of the maxima of each $N_p$ hit are considered as the drift coordinate positions of the new hits. Example of hit finding and hit fitting procedure is shown in Fig. 3.7.
The particle energy deposit $q_E$ observed in a single hit is calculated as:

$$q_E = q_C W e^{\tau_d/\tau_e}, \tag{3.3}$$

where $q_C$ is the hit charge calculated as the integral of the corresponding hit $p(t)$, multiplied by the calibration factor evaluated in [93], $C = (152 \pm 2) \cdot 10^{-4}$ fC/(ADC $\mu$s). $W$ is the average energy needed for the creation of an electron-ion pair, $W = 23.6^{+0.5}_{-0.3}$ eV [94], and $\tau_e$ is the free electron lifetime, which is continuously monitored during the detector operation [65].

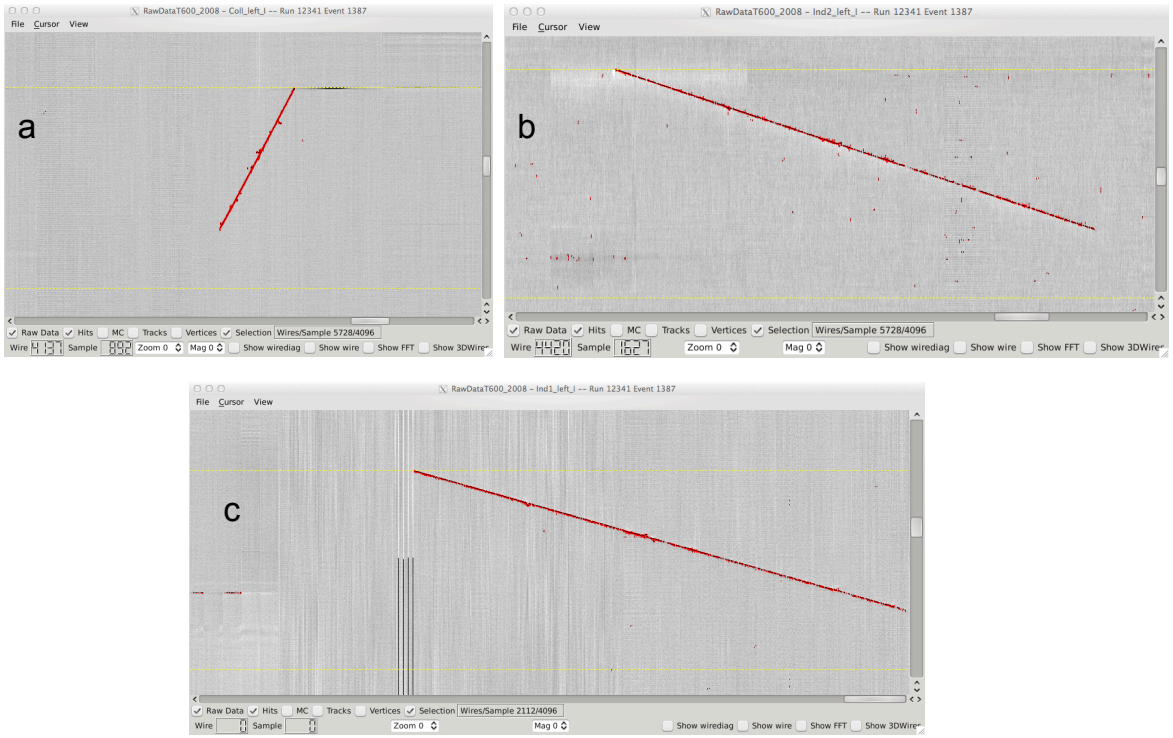


Figure 3.7: Example of hit reconstruction of a cosmic muon event: the red points correspond to hits in: (a) Collection view, (b) Induction2 view and (c) Induction1 view. The yellow lines correspond to the wire plane and cathode positions.

## 3.2 Cluster reconstruction

The aim of clusterization is to have a coarse aggregation of hits in an event and it is a prerequisite to 3D reconstruction. The clusterization results in a rough identification of regions between those where clear and separate tracks are present and those where, instead, hits density is high, like the case of showers, either electromagnetic or hadronic, giving a first event topology [90].
A cluster is defined as a group of adjacent hits within the wire/drift coordinate plane which have a common charge deposition distribution. The clusterization algorithm takes as input a list of hits from a given wire plane, and constructs all possible clusters out of them, using the information obtained by the hit finding algorithm.
Firstly, preliminary clusters are built as groups of hits being connected by links, defined as pair of hits found on adjacent wires and having overlapping drift coordinate intervals, i.e. drift range in which the hit is found.
Then, there is the attempt to expand and merge cluster fragments, in order to reduce fragmentation and the number of the resulting clusters. It proceeds as follows: the regions around the cluster borders are examined, where a cluster border is defined as a hit linked at most with one hit within the cluster. When no clusters are found, new hits are searched in the region close to the cluster borders and are added to the cluster, hence reducing the cluster fragmentation caused by hit misidentification. Once no further expansion along the wire coordinate is possible for any of the existing clusters, the merging of clusters along the drift coordinate direction is attempted. For that, the hits at the maximal and minimal drift coordinate values are compared among different clusters. Cluster merging is carried out for those pairs of clusters for which the respective minimal and maximal drift coordinate hits are in the same or adjacent wires, and whose drift coordinate ranges overlap [90].
Example of cluster reconstruction is shown in Fig. 3.8, where a cosmic muon track is depicted.

## 3.3 3D reconstruction

The general approach is the optimisation of 2D projections in the wire views, in order to build 3D objects. It follows the Polygonal Line Algorithm [95], which is an efficient algorithm for the principal curve finding problem. In this case, the problem is finding the best track that fits real data [76].
The particle real track $T$ is observed in the detector as a set of three 2D projections $P_{I1}(T)$, $P_{I2}(T)$, $P_C(T)$ from Induction1, Induction2, and Collection wire planes, respectively. The idea of the algorithm is represented in the Fig. 3.9.
The 3D fit trajectory $F$ may be projected on each wire planes according to the operators $P(F)$.
The fit $F$ is built by minimizing a measure of the distance $D$ between the fit

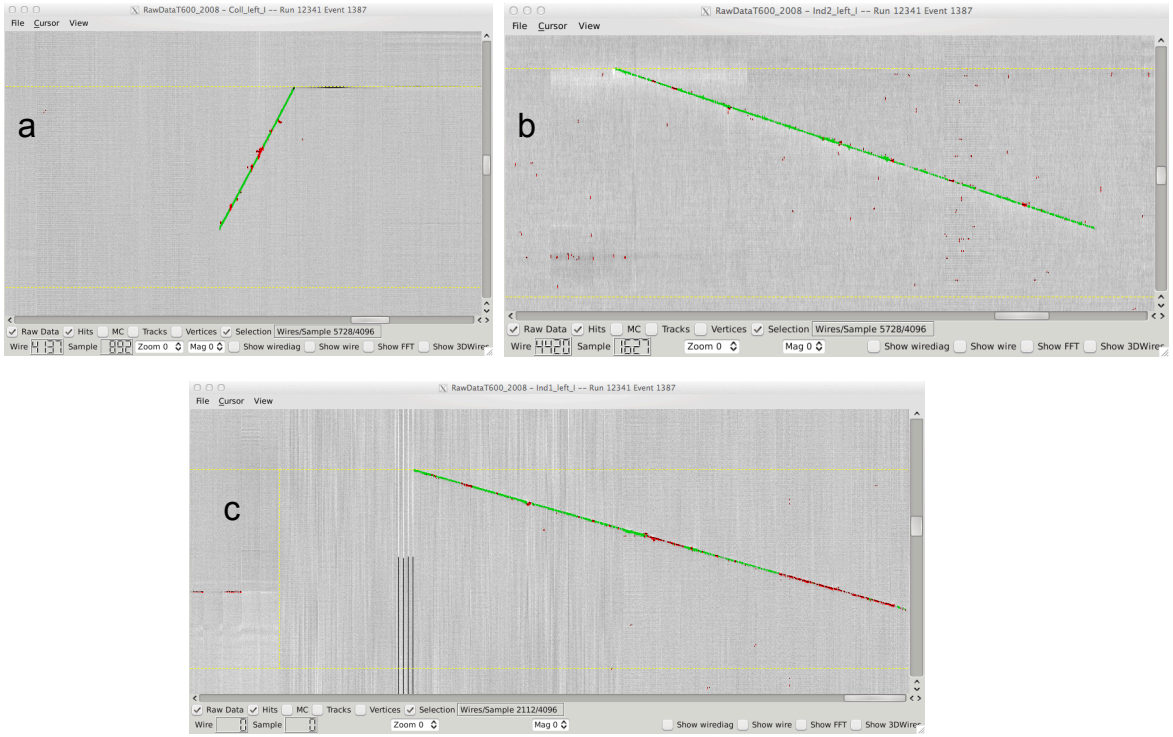


Figure 3.8: Example of clusterization in a cosmic muon event: the green points correspond to the muon cluster in (a) Collection view, (b) Induction2 view and (c) Induction1 view. The red points are the hits not included in the muon cluster (delta rays or misidentification). The yellow lines correspond to the wire plane and cathode positions.

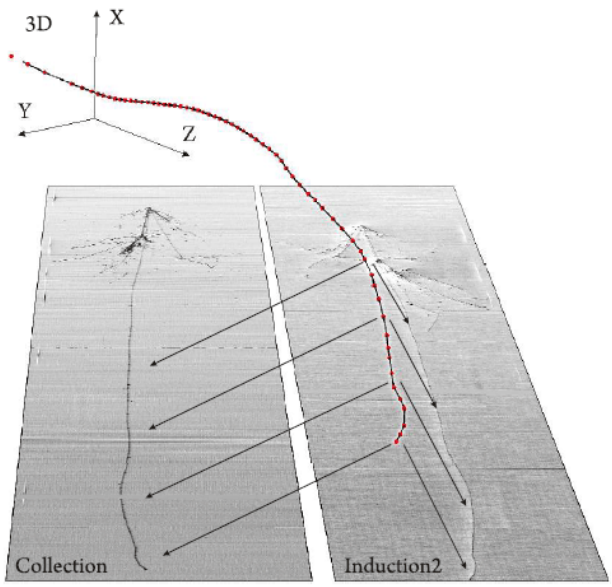


Figure 3.9: General idea of the 3D reconstruction: build a 3D object using optimisation of the event 2D projections in the wire planes.

projections and the track hits in all wire planes simultaneously, with constraints $C_j(F)$ that may include factors such as trajectory curvature and distance to the already identified and reconstructed interaction vertices. This may be expressed with an objective function $G(F)$ [76]:

$$G(F) = \sum_i \alpha_i D\left[P_i(T), P_i(F)\right] + \sum_j \beta_j C_j(F), \tag{3.4}$$

where wire planes, denoted with the index $i$, and constraint factors, denoted with the index $j$, have a weighted impact on the overall $G(F)$ value according to the $\alpha_i$ and $\beta_i$ coefficients.
The best fit track $F$ is approximated with the polygonal line determined by 3D points, called later *nodes*, interconnected with straight 3D segments.
The algorithm starts from two nodes connected with a single segment. The initial 3D positions of the first two nodes should roughly correspond to the track end points. Generally, hits in the individual wire views are not ordered and the exact matching of hits corresponding to the actual track end points is not possible. The initial node positions are evaluated as follows: a straight line is fitted to the hits within the wire plane using the linear regression; two outermost projections of hits to the fitted line are considered as 2D end points; end points from two wire planes are paired by the minimal drift time difference to obtain 3D node positions.
Then the minimization of the objective function $G(F)$ is performed to find the optimal positions of the first nodes.
The track fit $F$ is constructed in an iterative way by adding new nodes and rebuilding segments: the positions of all node $n_k$ and the $F$ are optimised and updated when a new node is added.
The 2D projections of the track fit $F$ are determined by the node 2D projections, $P_i(n_k)$, which also describe segment 2D projections. The algorithm stops when the maximum number of nodes $K$ is reached, that is calculated considering the length of the track and the number of hits.
Every 2D hits are assigned to the fit segment or node. This is done by finding the segment/node 2D projections with the minimal distance to the 2D hit, as it is illustrated in Fig. 3.10.
Then the node positions are update to minimize the function in Eq. 3.4. To reduce the computational complexity, it is convenient to expressed $G(F)$ as sum of independent components [76]:

$$G(F) = \sum_k g(n_k), \qquad g(n_k) = d(n_k) + \beta_v c_v(n_k) + \beta_a c_a(n_k). \tag{3.5}$$

The first component $d(n_k)$ of this function is the average of the squared distance of the fit projection to the 2D hits that are assigned to the $k$-th node and segments connected to that node, in all wire planes.
The term $c_v(n_k)$ is the average squared distance of the fit to the 3D vertices

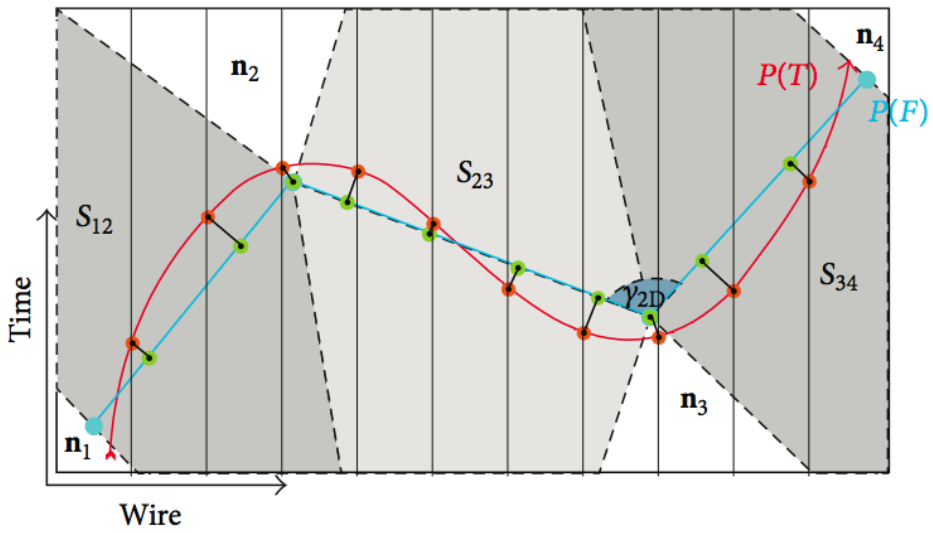


Figure 3.10: Schematic view of the track $P(T)$ (red) and fit $P(F)$ (blue) projections in the wire plane. 2D hits (orange dots) are marked on the track projection intersections with wires; hit projections to $P(F)$ are marked as green dots; hit distances to $P(F)$ are marked with black sections. Hits from grey shaded regions $s_{xy}$ are assigned to segments; hits from white regions $n_x$ are assigned to nodes. Indicated angle $\gamma_{2D}$ is the 2D projection of the $\gamma$ angle between the fit segments in 3D [76].

created independently from the track reconstruction algorithm, such as points that tag the particle interactions, decay points or delta rays identified along the particle track.
Constraint on the angles $\gamma$ between the consecutive 3D segments and on the length of the outermost segments where the angle $\gamma$ cannot be calculated are included in the last term of the function, $c_a(n_k)$.
Coefficients $\beta_v$ $\beta_a$ allow to keep balance between overfitting to the noise in hit/vertex positions and ability to reconstruct correctly the significant track features. The actual values of these coefficients depend on the noise conditions of the readout wire planes and were adjusted empirically to maximize the reconstruction efficiency: $\beta_v$= 1.0 and $\beta_a$= 2.0 for each wire plane.
The algorithm stops when the minimization of $G(F)$ converges to a stable value: the relative change of $G(F)$ is calculated after each step of the minimization algorithm, which updates all node positions. The value of $G(F)$ is considered as stable when the relative change is below $10^{-4}$ [76].
Finally, the 3D positions corresponding to the 2D hits are calculated.
Tests of this algorithm were made on Monte Carlo sample produced with FLUKA simulation package [118, 119] and then applied on real data. Results are described in [76]. One example of 3D reconstruction on real data is shown in Fig. 3.11,

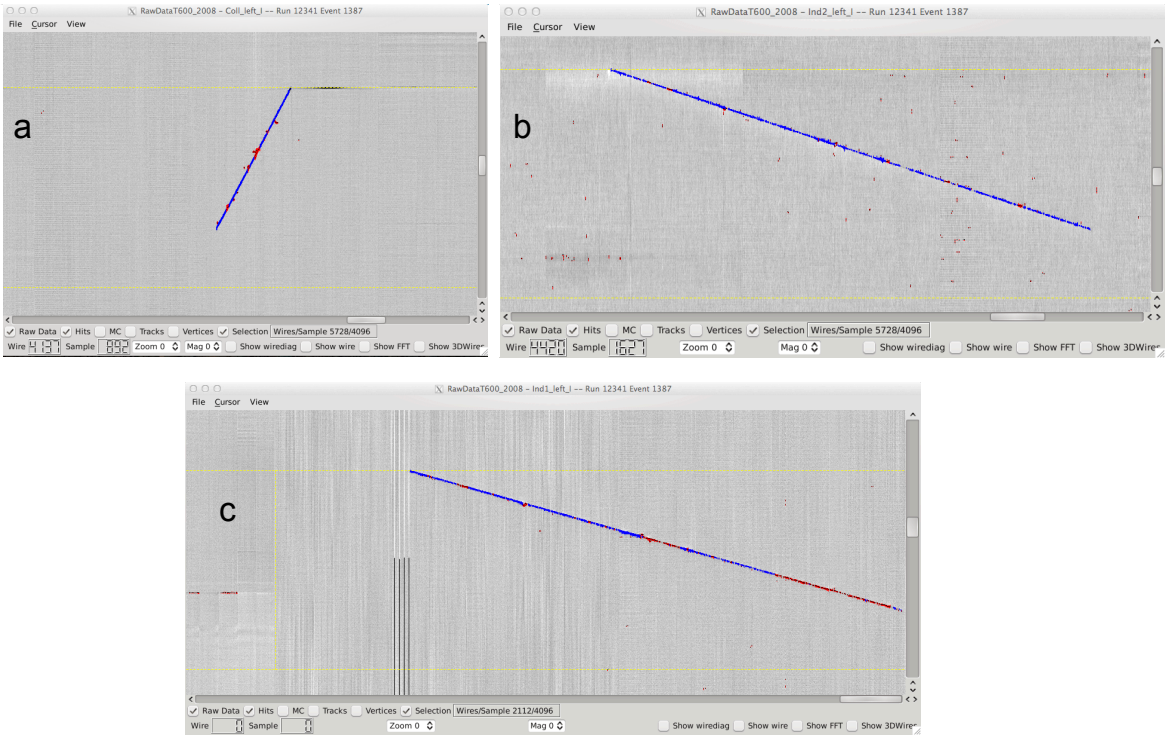


Figure 3.11: Example of 3D reconstruction of a cosmic muon event: the blue points correspond to the muon track in (a) Collection view, (b) Induction2 view and (c) Induction1 view. The red points are the hits not included in the muon track (delta rays or misidentification). The yellow lines correspond to the wire plane and cathode positions.

### 3.3.1 Calorimetric measurements

Thanks to the properties of LAr TPC, it is possible to perform the calorimetric reconstruction of events [76].
The sequence of the ionization charge $dQ$ collected per track $dx$ length, $dQ/dx$, is evaluated from the charges and the 3D positions of the Collection plane hits. The hit charge is assigned to the $\delta x$ length surrounding the hit, calculated as $\delta x = (x_1 + x_2)/2$, where $x_1$ and $x_2$ are the distances to the preceding and subsequent Collection hits, respectively. Hit charges and $\delta x$ lengths are summed up until the minimum value of $dx$ is reached.
Since tracks nearly parallel to the drift direction can contain several hits within a small range along the drift direction, it is convenient to limit the minimal $dx$ length to a value close to the wire spacing distance: in this case 2.7 mm [76]. In this way $dx$ values are comparable for any track orientation with respect to the Collection wires direction. Then the correction due to the recombination effect [69] may be applied to obtain the actual value of the energy deposit per track $dx$ length, $dE/dx$, according to the Birk semiempirical formula, which can be expressed as:

$$dE = \frac{dQ}{R}, \tag{3.6}$$

where $R$ is the correction factor, $R = 0.71$ [69], calculated as:

$$R = A - \frac{k}{\epsilon \cdot \rho} \cdot \frac{dQ}{dx}. \tag{3.7}$$

which values are [69]: $A = 0.81$, $k = 0.055$ (kV/cm)(g/cm$^2$)/MeV, $\epsilon = 0.5$ kV/cm and $\rho = 1.4$ g/cm$^2$. Applying this formula to real data, it is possible to perform a particle identification comparing the $dE/dx$ of each track with the theoretical one obtained with the Bethe Bloch curves [96].
One example is presented in Fig. 3.12, where a decaying kaon is observed in the CNGS data [76].

## 3.4 Delta ray removal

Delta rays are secondary electrons with enough energy to escape a significant distance away from the primary radiation track and produce further ionization. In a LAr TPC, they can be seen as small tracks coming from the primary track (see Fig 3.13).
In the reconstruction of a muon, delta rays could be a source of uncertainty, because they interfere with the actual energy and 3D reconstruction of the event. Therefore, an algorithm to remove them from the principal muon track has been developed.
After the clusterization (see Fig. 3.14a), this algorithm proceeds to analyse wires where two or more hits appear; these hits are delta rays candidates.
A linear fit of the other hits included in the cluster is performed, in order to

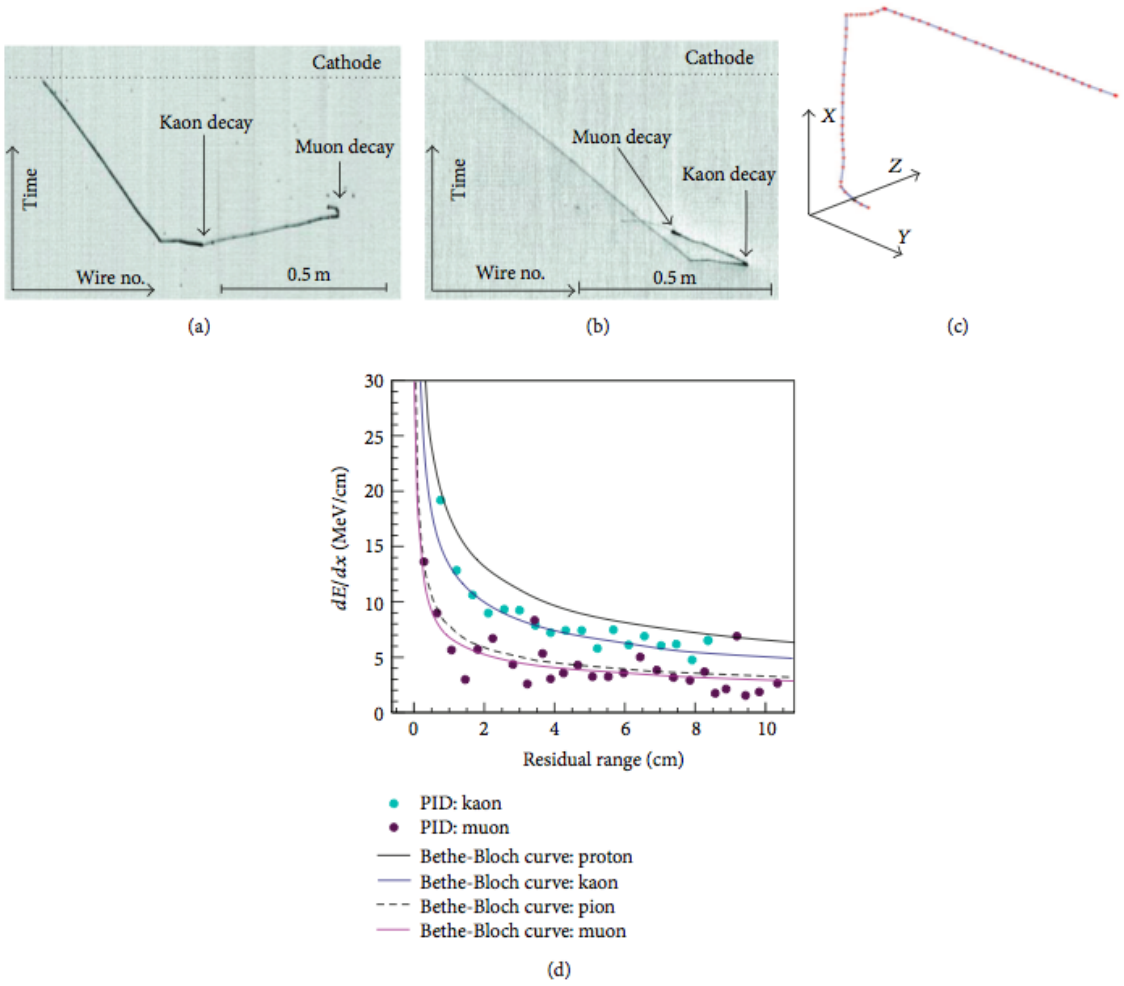


Figure 3.12: Example of a decaying kaon candidate observed in the CNGS data ($K$:$l$ = 90 cm, $E$ = 325 MeV; $\mu$:$l$ = 54 cm, $E$ = 147 MeV; $e$:$l$ = 13 cm,$E$ = 27 MeV): (a) the Collection view; (b) the Induction2 view; (c) the 3D reconstruction (fit nodes are marked with the red dots). (d) $dE/dx$ sequence for the kaon track (blue dots) and the muon track (violet dots) superimposed on the theoretical Bethe-Bloch curves. The muon data points with the high $dE/dx$ are due to the additional energy of delta rays. Their energy contribution is in agreement with the energy loss distribution expected for a muon track [76].

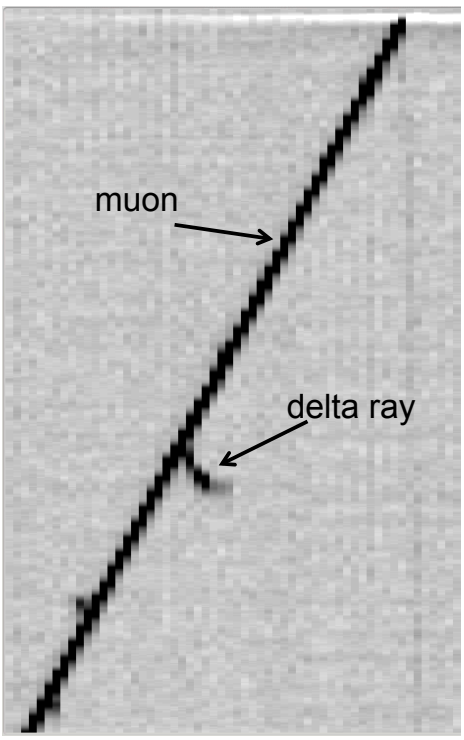


Figure 3.13: Example of delta ray originating from a muon track.

evaluate the direction of the track. At this point, the average distance $d_{mean}$ between every non delta ray hit and the line is evaluated (see Fig. 3.14b). Also the standard deviation $\sigma$ is calculated.
Then, in order to decide if the candidate is a delta ray, the distance $d_\delta$ between this hit and the line is evaluated. If $d_\delta > d_{mean} + \sigma$, the candidate is recognised and tagged as delta ray.
Once a hit is tag as delta ray, it is possible to exclude it from the cluster and so preserve only effective hit belonging to the muon track, as shown in Fig. 3.14c.

## 3.5 Conclusions

The ICARUS Collaboration developed and tested during many years of work a reconstruction procedure that permits to have a complete description of the event collected by the ICARUS T600 detector at underground conditions.
The essential element for the spatial and calorimetric measurements is the hit. Its identification aims to distinguishing signals produced by ionization electrons from electronic noise and it is based on geometrical features of the wire output signal in a given region. Once the hit has been detected, its reconstruction is performed with the aim of extracting the parameters defining it (position, height, area) which contain the physical information of the original

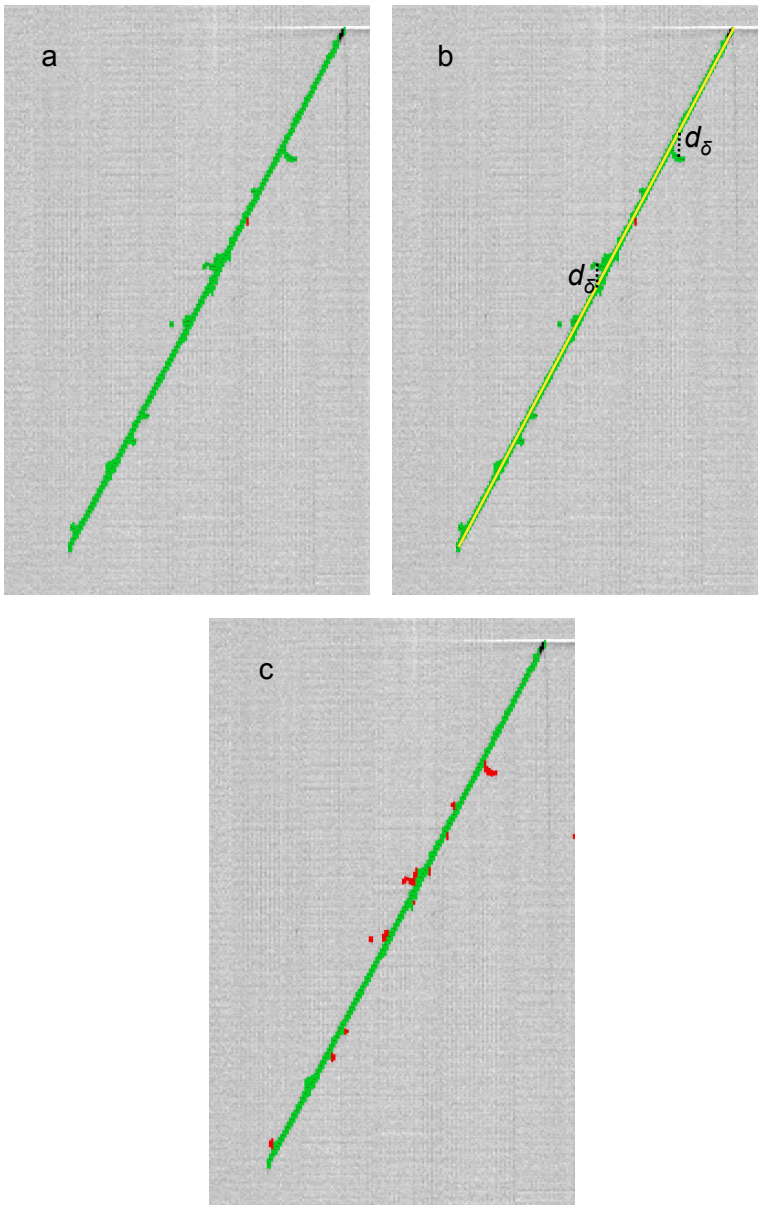


Figure 3.14: Example of delta ray tagging and removal procedure: in (a) the cluster (green points) contains hit belonging to muon track and delta rays; in (b) delta ray tagging procedure is depicted: the yellow line is the linear fit of no delta ray candidate, while the dotted lines correspond to the distances $d_\delta$; in (c) delta rays removal is applied and only the muon track cluster (green points) is selected.

associated track segment.
A group of adjacent hits within the wire/drift coordinate plane which have a common charge deposition distribution form a cluster. The clusterization algorithm takes as input a list of hits from a given wire plane, and constructs all possible clusters out of them, using the information obtained by the hit finding algorithm. The particle real track is observed in the detector as a set of three 2D projections from the three wire planes; in order to build 3D objects a dedicated algorithm has been developed, that finds the best track gradually minimizing the distance between the 2D projections of the reconstructed event and the real ones.
To ensure a faithful event reconstruction, it is mandatory to understand everything that could distort space and charge and to taking into account in the algorithms.
Some example are the possible presence of space charge effects inside the detector, a not well known drift electron diffusion parameter and the introduction of a magnetic field. In order to understand the influence of these effects in the detector, I made dedicated studies, that I will present in the next chapters.

Chapter 4

# Space charge effects in the ICARUS T600 detector

In a TPC detector the electric field is thought to be uniform along the drift direction: in fact, only an uniform electric field ensures an uniform drift velocity and thus the proportionality between drift time and drift coordinate and reliable reconstruction of the events.
When a charged particle crosses the detector, both electrons and positive ions are created. Under the influence of the electric field, ionization electrons are drifted toward the anode, where they are quickly collected, while positive ions are slowly drifted to the cathode.
These positive ions do not usually play an important role in the operation of ionization detectors, because the signal is due to electrons. Commonly their presence is negligible, but a local accumulation of positive ions, called *space charge*, could be relevant, especially for detectors operating with a high ionizing particle flux. Due to the presence of this space charge, electric field distortion may arise, not ensuring anymore the possibility to produce faithful images of the ionizing events.
The space charge effect could be relevant for detectors with long drift length and exposed to high particle fluxes. This is the case of detectors placed at surface or shallows depths, and so exposed to high cosmic ray flux, like the ICARUS T600 detector at FNAL (see Chap. 2).
A study of space charge effects in the T600 before its installation at FNAL is made possible analysing real data collected with cosmic rays at surface [97]. In fact this is not the first time for the detector to be exposed at high cosmic ray fluxes: a test run was performed at surface in Pavia, with a single T300 module, operating from April to August 2001 collecting a large sample of cosmic ray events with different trigger configurations [64, 63].
Each T300 is an independent unit housing an internal detector composed two TPCs, a field-shaping system, monitors and probes, and by two arrays of PMTs. Externally the cryostat was surrounded by a set of thermal insulation layers. The TPC wire read-out electronics was located on the top side of the

cryostat. The detector layout was completed by a cryogenic plant made of a liquid nitrogen cooling circuit to maintain uniform the LAr temperature, and of a system of LAr purifiers, to keep the LAr purity at a sufficiently high level. The Pavia test was performed with the first half-module fully assembled, instrumented and filled with LAr, while the second one was left empty, with no inner detector and purification systems installed, although functional from the point of view of cryogenics [64].
Some upgrades and improvements in the cryogenic plant were introduced after the 2001 test run for the long term operation at LNGS. In particular new solutions for cooling, insulation and re-circulation systems were adopted [68]. So cryogenic conditions between the two period were different; obviously during LNGS run both T300 modules were filled with LAr and cryogenic, temperature and pressure were improved with respect to Pavia run.

## 4.1 Electric field with space charge effects

The electric field $\vec{E}$ and the space charge density $\rho$ in a ionization detector, can be described by these two equations:

$$\nabla \cdot \vec{E} = \frac{\rho(x,y,z)}{\epsilon}, \tag{4.1}$$

$$\nabla \cdot \vec{J} + \frac{\partial \rho}{\partial t} = R_i. \tag{4.2}$$

The first one is one of the Maxwell equations, where $\epsilon = \epsilon_0 \epsilon_r$ is the dielectric constant of the ionization medium; the second one is the charge continuity equation, where $\vec{J} = \rho\vec{v}$ is the current density of positive ions and $R_i$ is the ionization density rate that correspond to the rate of charge injected in the detector (injection of charge rate).
To combine and solve 4.1 and 4.2 equations, we can assume that:

- the detector is described as an infinite parallel plate capacitor, whose electrodes are perpendicular to $y$ coordinate and parallel to $xz$ plane;
- the charge density $\rho$ is related to the ionization density rate $R_i$ that, under stationary conditions, is uniform over the detector;
- the ion drift velocity is determined by the positive ion mobility coefficient $\mu_i$ and the electric field $\vec{E}$ :

$$\vec{v} = \mu_i \vec{E}. \tag{4.3}$$

Under the assumptions above, the electric field depends only on the $y$ coordinate ($\vec{E} = E(y) \cdot \vec{y}$) and on the time $t$. Thus, by using the definition of $J$, Eq. 4.1 and Eq. 4.2 become :

$$\frac{\partial E(y)}{\partial y} = \frac{\rho}{\epsilon}, \tag{4.4}$$

$$\frac{\partial(\rho v)}{\partial y} + \frac{\partial \rho}{\partial t} = R_i. \tag{4.5}$$

Combining this two equations and remembering the Eq. 4.3, we obtain the general expression for the time evolution of space charge:

$$\frac{\partial \rho}{\partial t} + \mu_i E(y)\frac{\partial \rho}{\partial y} + \rho\mu_i \frac{\partial E(y)}{\partial y} = R_i. \tag{4.6}$$

Therefore, the time evolution of the space charge is related to the ion drift, represented by the second term on the left-hand side, and to the rate of charge injection $R_i$. The third term on the left-hand side is due to the distortion induced by drift across regions with variable electric field, and it is relevant only for relatively large $R_i$ and $\rho$.
At this point, the stationarity of $R_i$ allows us to find a simple solution for Eq. 4.6. In fact, if $R_i$ is constant, $\rho$ and E evolve towards a stationary case and Eq. 4.2 can be simplified as:

$$\frac{\partial \rho v}{\partial y} = R_i, \tag{4.7}$$

whose solution is:

$$\rho v = R_i C, \tag{4.8}$$

considering the anode at $y = 0$ and the cathode at $y = \mathrm{C}$. The steady state ion density $\rho$, in a volume element at position $y$, is then equal to the positive ion density created in that volume element during time $y/v$, i.e. the time during which positive ions have drifted from the anode to their present position.
Remembering the expression of drift velocity in terms of ion mobility $\mu_i$, we can express the ion density as:

$$\rho = \frac{R_i y}{\mu_i E(y)}, \tag{4.9}$$

that permits to rewrite Eq. 4.1 as :

$$\frac{\partial E(y)}{\partial y} = \frac{R_i y}{\epsilon \mu_i E(y)}. \tag{4.10}$$

This can be directly solved as:

$$E(y) = \sqrt{E_A^2 + \frac{R_i y^2}{\epsilon \mu_i}}. \tag{4.11}$$

where $E_A$ denote the field at the anode ($y$=0) and it is determined by the boundary condition of the voltage $V$ between anode and cathode. This means

that without ionization rate, i.e. $R_i$=0, the field is defined by the potentials on the electrodes and it is constant. On the contrary, the presence of a small ionization rate introduces a distortion of the electric field which increase rapidly with the drift length $y$.
It is convenient to use the dimensionless variable $\alpha$ [100]:

$$\alpha = \frac{C}{E_0}\sqrt{\frac{R_i}{\epsilon\mu_i}}, \tag{4.12}$$

where $E_0 = V/C$ is the nominal electric field in absence of space charge and $C$ is again the cathode position. In this way, Eq. 4.11 becomes:

$$E(y) = E_0\sqrt{\left(\frac{E_A}{E_0}\right)^2 + \alpha^2\frac{y^2}{C^2}}. \tag{4.13}$$

Fig. 4.1 provides the value of normalised electric field at the anode and the cathode as a function of $\alpha$: the distortion of electric field due to space charge build up can be completely described by this parameter.

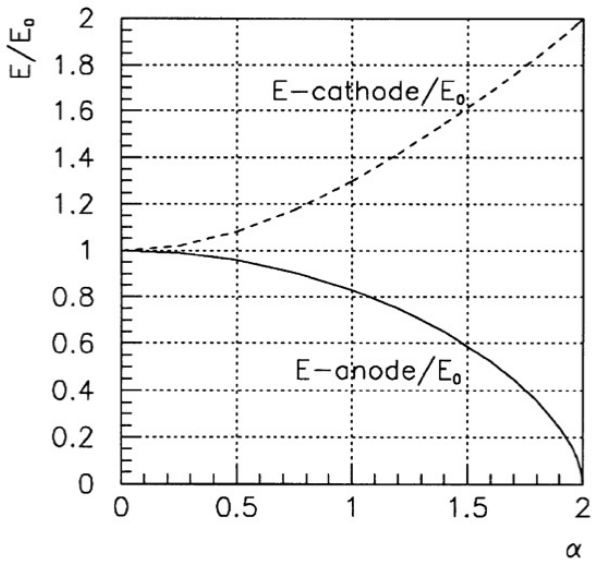


Figure 4.1: Normalised electric field values at anode and cathode in function of the dimensionless parameter $\alpha$ [100].

An analytic expression for the field $E_A$ can be obtained from Eq. 4.13 by calculating the voltage between the anode and the cathode,

$$V = \int_0^C E(y)dy = \frac{\alpha E_0 C}{2}\left[\sqrt{1+\left(\frac{E_A}{\alpha E_0}\right)^2} + \left(\frac{E_A}{\alpha E_0}\right)^2 ln\left(\frac{\alpha E_0}{E_A} + \sqrt{1+\left(\frac{\alpha E_0}{E_A}\right)^2}\right)\right]. \tag{4.14}$$

This expression enlighten the fact that the treatment exposed above fails at large $R_i$ intensities: if $\alpha = 2$, the quantity in brackets must be 1, which implies that $E_A = 0$. But, if the anode goes to zero, the electrons are no longer collected there, and we can not ignore space charge due to electrons. Thus, the present solution is valid only for $E_A > 0$ and $\alpha < 2$: outside of this region of values the ionization detector would not work effectively [100].

### 4.1.1 Space charge in a LAr TPC at surface

The example of a LAr TPC with a nominal electric field of $E_0$=500 V/cm is considered to understand the effect of space charge in the T600 detector. Ionizing particles that cross the detector, produce positive ions ($Ar^+$) that survive in the drift region for a very long time. They flow very slowly toward the cathode, because their mobility in LAr at the nominal electric field, $\mu_i \sim 1.6 \cdot 10^{-3}\ cm^2 s^{-1} V^{-1}$, is much smaller then the free electrons one $\mu_e \sim 500\ cm^2 s^{-1} V^{-1}$ [98]. The positive ion nominal drift velocity is $v_0 = 0.8$ cm/s: this means that it takes ∼125 s to them to drift 1 m; under this conditions, the amount of space charge could be significant.
High energy cosmic muons are the dominant ionizing radiation at Earth's surface; their rate is roughly [99]:

$$\frac{dR}{dcos\theta} \approx \begin{cases} 0.045\ \ cos^2\theta/cm^2/s & 0 < \theta < \pi/2 \\ 0 & \pi/2 < \theta < \pi. \end{cases} \tag{4.15}$$

Considering a horizontal area $A$ and thickness $h$, the total path length of cosmic muon, traversing the surface with an angle $\theta$ with respect to the vertical in one second is:

$$\int_0^1 \frac{Ah}{cos\theta} \frac{dR}{dcos\theta} dcos\theta; \tag{4.16}$$

which implies that the total path length (in cm) of cosmic ray muons in one second inside a cube of volume 1 $cm^3$ is [99]:

$$\int_0^1 \frac{1}{cos\theta} \frac{dR}{dcos\theta} dcos\theta \approx 0.022\ cm. \tag{4.17}$$

Therefore, assuming $dE/dx \sim$ 2MeV/cm and a ionization yield (including recombination in LAr) of ∼ 4 fC/MeV [64], the rate of creation of positive ion density results $R_i = 1.8 \times 10^{-10}$ C m$^{-3}$ s$^{-1}$. At the nominal electric field of 500 V/cm, the $\alpha$ parameter for liquid argon at surface is : $\alpha = 0.17\ C$, for a detector with drift length $C$ expressed in m. If we consider a detector with $C = 1.5$ m, the effects are not so high, being $\alpha \approx 0.26$; for longer drift detector, i.e. with $C > 2.5$, the effects could be noticeable.
Substituting the numbers into Eq. 4.11, one obtain how much the electric field is distorted by space charge, as a function of the drift length $y$ (as depicted in Fig. 4.2):

$$E(y) \approx E_A \sqrt{1 + \left(\frac{1.8\ y/cm}{1000}\right)^2}. \tag{4.18}$$

Using this relation, it is possible to evaluated the approximate electric field distortion $E_{dis}(y)$ as :

$$E_{dis}(y) \approx \frac{E(y) - E_A}{E_A}. \tag{4.19}$$

Given $E_A = 500$ V/cm, for various drift lengths $y$, we obtain the values in Tab. 4.1.

| drift lenght $y$ [cm] | $E_{dis}$ |
|---|---|
| 50 | 0.04 % |
| 100 | 1.61 % |
| 150 | 3.58 % |
| 200 | 6.29 % |
| 250 | 9.65 % |
| 300 | 13.64 % |

Table 4.1: Electric field distortion $E_{dis}$ calculated for different drift lengths $y$ using the Eq. 4.19 with $E_A = 500$ V/cm.

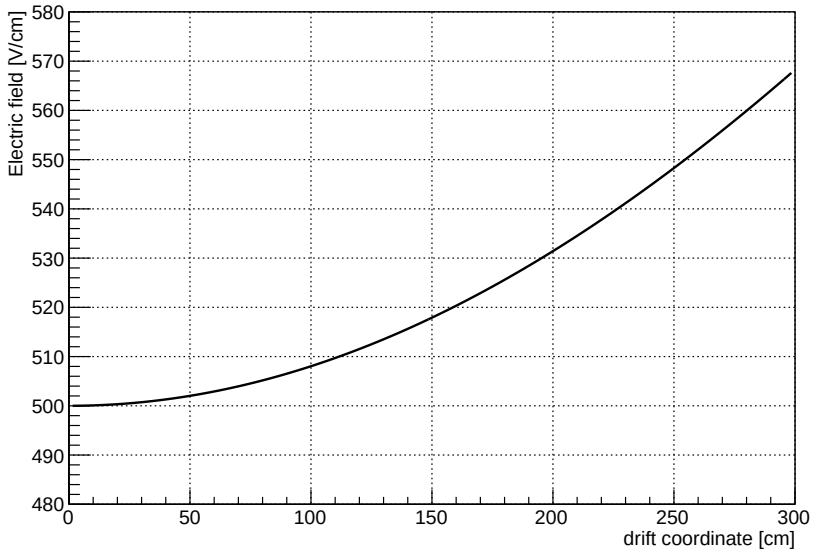


Figure 4.2: Electric field values as a function of drift coordinate $y$ for $E_A = 500$ V/cm, calculated with Eq. 4.18.

It is important to point out that this calculation is made neglecting thermal-induced convective motion, that could modify the positive ions drift velocity and their density inside the detector.

## 4.2 Space charge effects in ICARUS T600 detector

As touched upon it above, during it operation at FNAL, there could be the possibility for the ICARUS T600 detector to be affected by space charge, being at shallow depths condition. The detector had similar experimental conditions during a test run in Pavia, where only one T300 operated at surface [63, 64]. Analysing cosmic muons collected during this run, it is possible to estimate space charge effects and to evaluate if they can affect the event reconstruction procedure. In particular, to study the possible space charge effects, I consider a sample of cosmic muon bundles because they are composed of high energy parallel muon, with no observable multiple scattering and so they can be assimilated with straight lines, as we can see in Fig. 4.3.

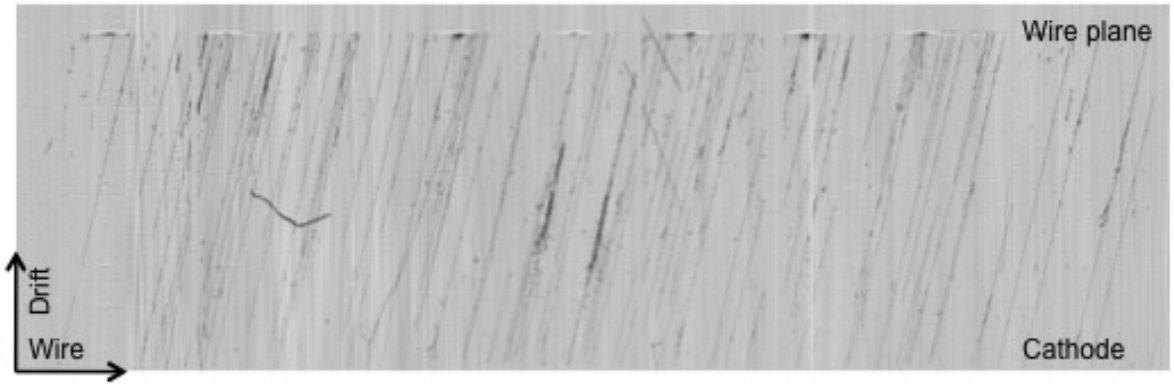


Figure 4.3: Example of a muon bundle recorded at surface with the ICARUS T600 detector. Anode and cathode are enlighten, such as wire and drift coordinates.

The whole sample used in this analysis includes 129 muons that cover entirely the drift volume, because it is important to study completely this path . I select each muon track by visual scanning; hit finding, fitting and clusterization procedures are then performed within the `Qscan` analysis framework, as described in Chap. 3 and depicted in Fig. 4.4. In each muon track, I remove delta rays (as described in Chap. 3), in order to have a pure muon sample. First and last 1.5 cm of each track are removed from the muon cluster, to avoid possible boundary disuniformities due to the presence of the wires and of the cathode plane.
Muon tracks observed to bend, following a parabola, could suggest the presence of a possible positive ion accumulation: in fact, due to the dependence of the electron drift velocity on the electric field, the ionization electron arrival time on the anode in presence of space charge effects will be delayed with respect to the time observed in case of uniform electric field.
The bending of muon tracks can be estimated through this time delay, that can be defined as:

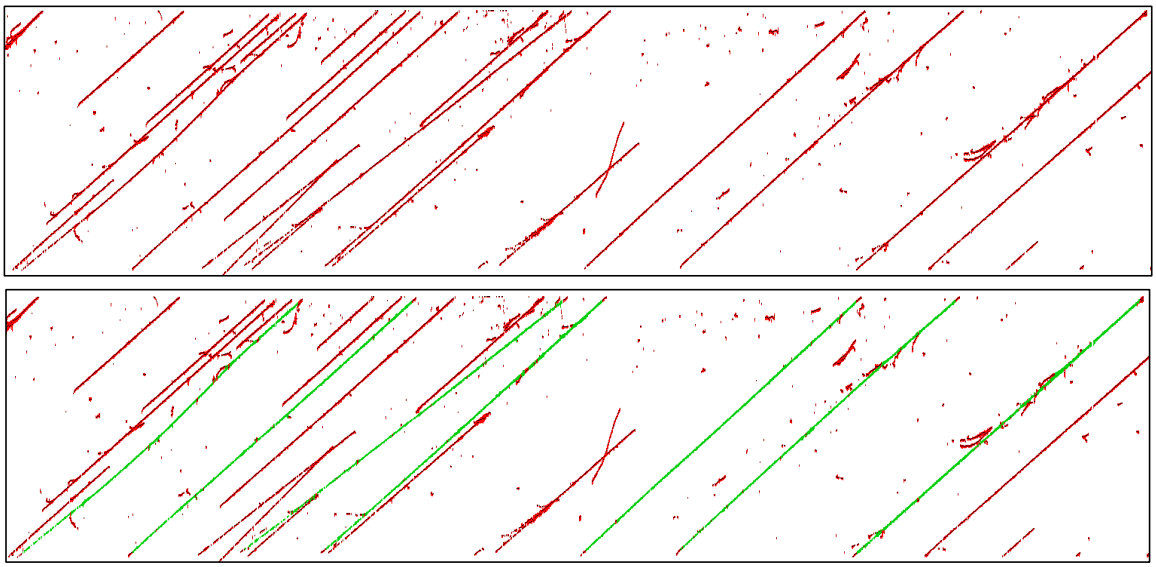

Figure 4.4: Enlarged view of a muon bundle event recorded in one chamber. Top: hits identified for all tracks are shown. Bottom: green points correspond to muon tracks that passed both cathode and wire planes. As we can see from the picture, the muon clusters do not include the first and last 1.5 cm in order to avoid boundary disuniformities due to wire and cathode planes.

$$\Delta T = T_{sc} - T_u, \tag{4.20}$$

where $T_{sc}$ is the electron arrival time on the anode when space charge effects are present, while $T_u$ is drift time in the case of uniform electric field. In Fig.4.5 left there is a schematic explanation of what $\Delta T$ represents: the ionizing track is the muon track in case of uniform electric field corresponding to arrival time $T_u$, while the apparent track is the muon track, whose reconstruction is bent by space charge, that correspond to $T_{sc}$.
In practice, we can suppose that the muon track is bent, so the drift time registered corresponds to $T_{sc}$ of the Eq. 4.20, while $T_u$ corresponds to the time that a straight muon would have. This straight muon track is obtained fitting the first and the last parts of the track, where the electric field is fixed by boundary conditions. Then, for the remaining part of the track, the bending parameter $\Delta T$ is calculated hit by hit (as shown in Fig. 4.6). In this calculation, for convenience, $\Delta T$ is expressed in unit length, i.e. the drift time is multiplies for the drift velocity.
The algorithm for the evaluation of $\Delta T$ is within the `Qscan` analysis framework, in which I develop new classes. The linear fit is performed by means of `pol1` included in `ROOT` Data Anlysis Framework [101].
Results presented in the following are obtained fitting linearly the first and last 5 cm of tracks. This value is a good compromise in order to use, for the linear fit, points in regions where the electric field is surely uniform and, at the same time, to have an adequate number of points for the $\Delta T$ calculation. Tests with

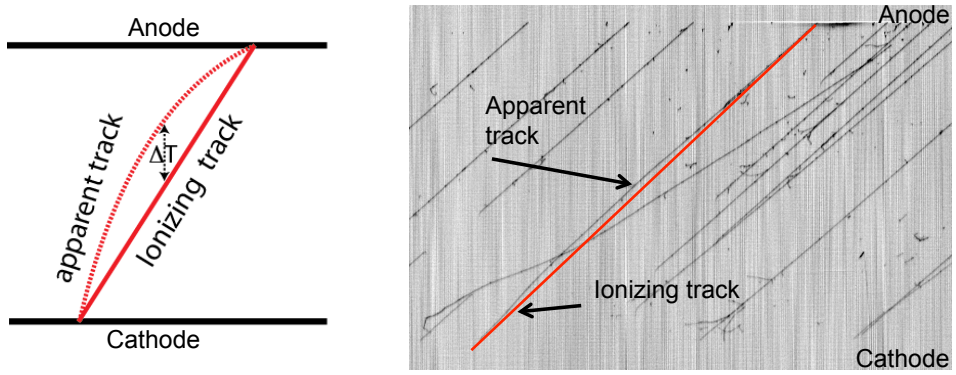


Figure 4.5: Left: schematic view of the bending parameter $\Delta T$. Right: example of muon track bending on real data.

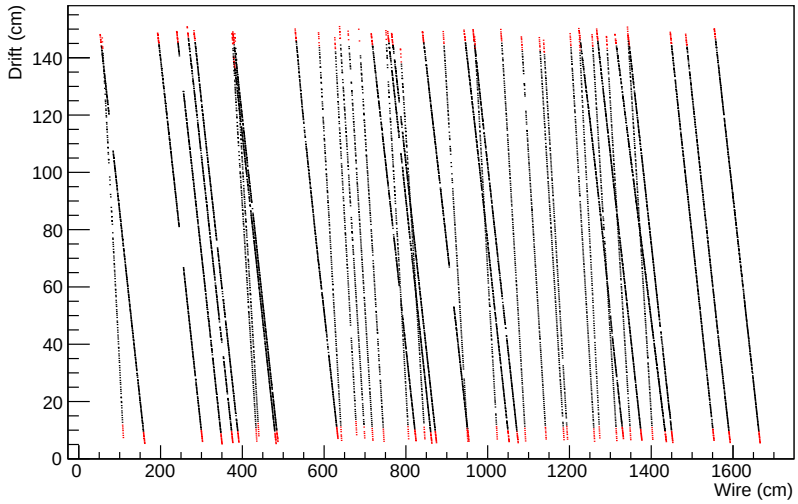


Figure 4.6: Example of muon bundle event (in both chambers) where the red points are the hits at the track edges used for the linear fit, while the black points are the hits used for the $\Delta T$ calculation.

shorter length have been done, however in this case not all the muons result properly fitted; on the contrary with longer length, no benefits on the fit are obtained, reducing the points for the $\Delta T$ calculation.

### 4.2.1 Results on Pavia data

As a first attempt to identify the possible bending of the tracks using the procedure described above, the $\Delta T$ parameter is evaluated as a function of the drift time. In the following, the anode position corresponds to the 0 in drift coordinate, while the cathode position is at $y = 150$ cm.
At a first sight, the scatter plot in Fig. 4.7 shows that some muons present a curvature of their track: especially for two of them, the curvature is clearly visible also with a visual scan. From this plot, it is possible to evaluate the distribution of $\Delta T$, that we can see in Fig. 4.8. As expected, the distribution is not perfectly peaked to zero: its mean value is $\Delta T_{mean} \sim 0.18$ cm with a RMS given by $\Delta T_{error} \sim 0.67$ cm.

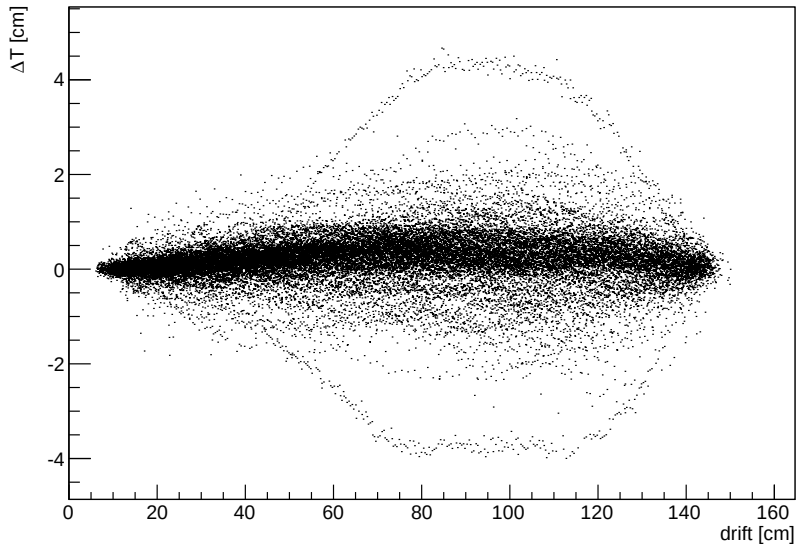


Figure 4.7: Plot of bending parameter $\Delta T$ in function of drift coordinate for all the Pavia track separately. The anode position corresponds to the 0 cm in drift coordinate, while the cathode position is at 150 cm.

As a second method, the drift path is divided into intervals 1 cm width and the average $\Delta T$ for all tracks is calculated for each of them, as shown in Fig. 4.9. The effect of space charge presence in ICARUS T600 seems to be confirmed: points in Fig. 4.9 follow a parabola, suggesting a distortion of the tracks. The maximum deviation from the linear fit on the graph is found to be $\Delta T_{max} = 0.34$ cm.
In order to verify the hypothesis of a effective space charge effect, I fit the curve with a parabola, defined with the `pol2` `ROOT` function as $f(x) = p_2\, x^2 + p_1\, x + p_0$.

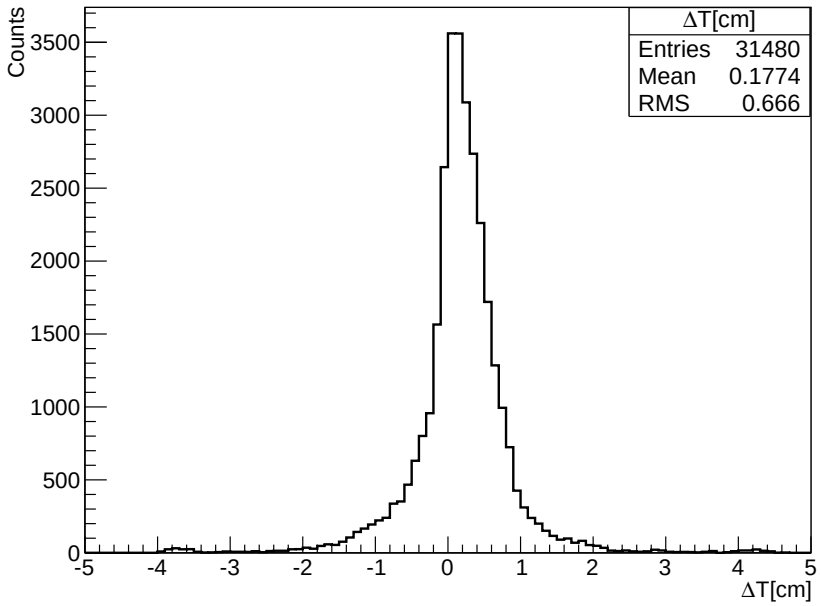


Figure 4.8: Distribution of bending parameter $\Delta T$ for the whole sample of muon tracks recorded in Pavia.

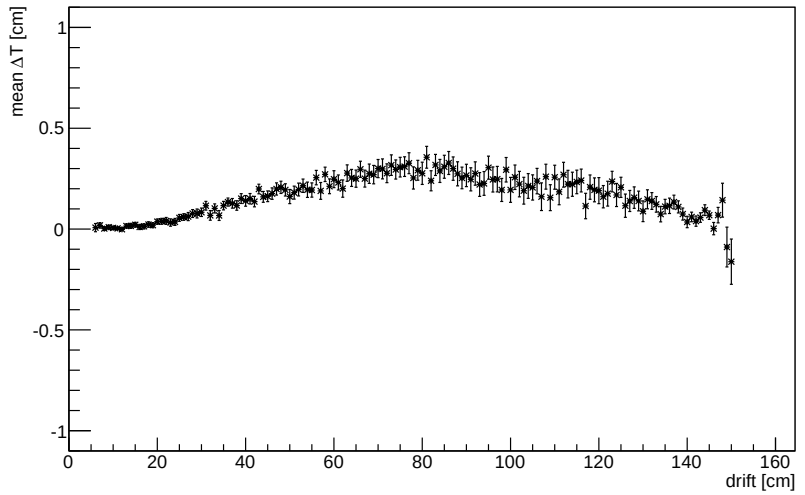


Figure 4.9: Average $\Delta T$ calculated for each centimetre of the drift path, considering the whole Pavia muon sample. The anode position corresponds to the 0 in drift coordinate, while the cathode position is at 150 cm.

For my purposes, the important parameter is the curvature of the parabola, that is represented by the parameter $p_2$. Fitting the data with this function, as shown in Fig.4.10, I find $p_2 \sim$ (-4.6 $\pm$ 0.15) $\cdot$ $10^{-5}$.

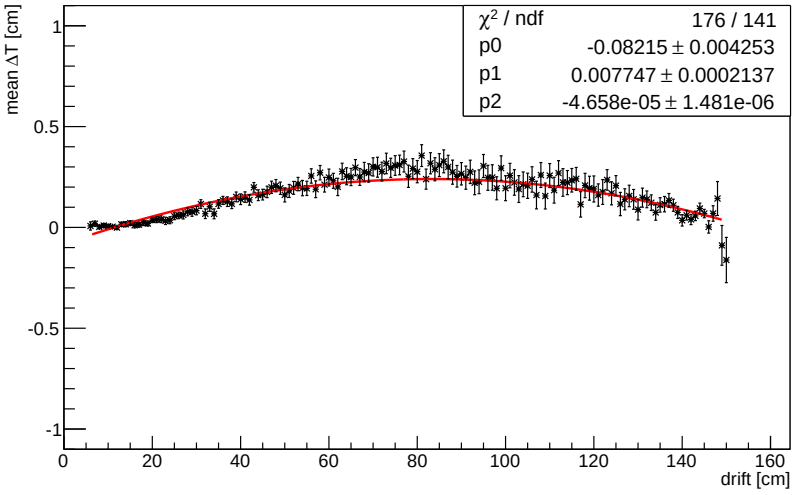


Figure 4.10: Average $\Delta T$ calculated for each centimetre of the drift path, considering the whole Pavia sample. This curve is then fitted with a parabolic function (red line): f(x) = $p_2\ x^2 + p_1\ x + p_0$ . The anode position corresponds to the 0 in drift coordinate, while the cathode position is at 150 cm. The resulting fit parameters are also shown.

I try also to fit only the central part of the drift path in the range [30, 130] cm, in order to evaluate $p_2$ where the curve seems more evident (see Fig. 4.11): in this case, $p_2$ has the same order of magnitude as considering the entire range, $p_2 \sim$ (-7.1 $\pm$ 0.55)$\cdot$ $10^{-5}$.
It is also possible to fit every muon track with a parabola, using `pol2` defined in `ROOT`, and calculate the mean value of the $p_2$ distribution. In this case the mean parameter is retrieved by the distribution in Fig. 4.12: $p_{2mean} \sim$ -2.0 $\cdot$ $10^{-4}$ with an error given by the RMS of the distribution $p_{2error} \sim 2.3 \cdot 10^{-3}$. It results compatible with zero.
These results are hints that space charge effects can be negligible, because considering both the whole sample or each track separately, the curvature is approximatively 0 and well below the detector spatial resolution.
To better investigate the problem, I decided to compare the results of $\Delta T$ as a function of the drift coordinate with a numerical simulation, in which possible electric field distortions caused by space charge are calculated as a function of the drift path, as expressed in the Eq. 4.18.
As we can see in Fig. 4.13, data follow the simulation curve and seems to be in good agreement with the simulation, apart from the first and last sections, due to the $\Delta T$ calculation method.
The trend is slightly different: the maximum deviation from the straight line

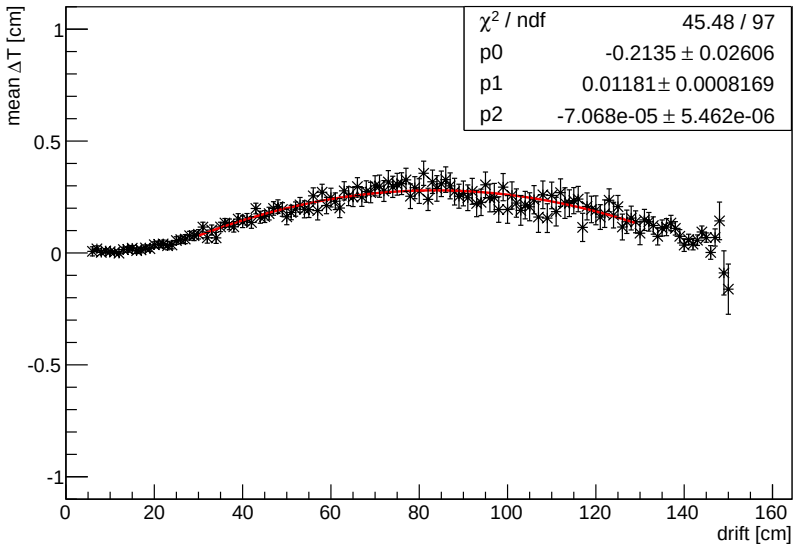


Figure 4.11: Average $\Delta T$ calculated for each centimetre of the drift path, considering the whole Pavia sample. This curve is then fitted with a parabola (red line) in the range [30, 130] cm, where the curvature seems more evident. The anode position corresponds to the 0 in drift coordinate, while the cathode position is at 150 cm. The resulting fit parameters are also shown.

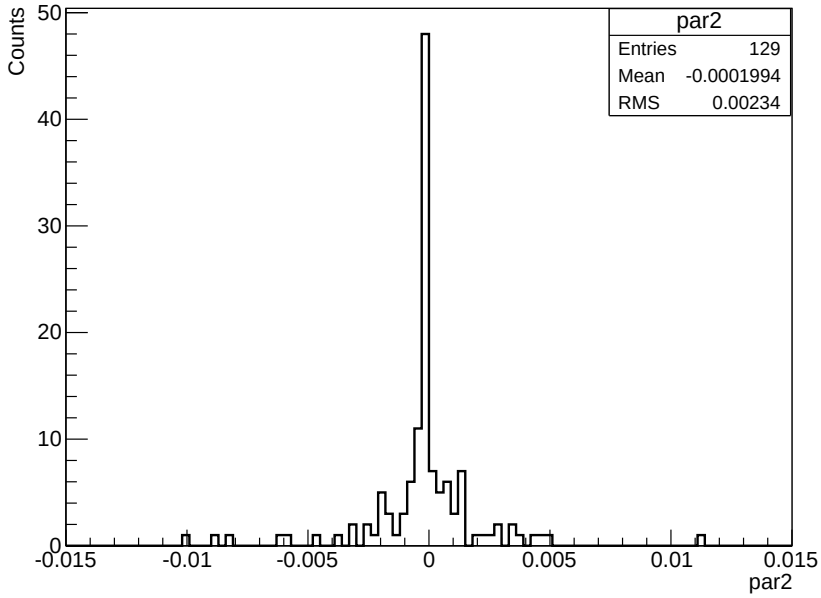


Figure 4.12: Distribution of second order parameters $p_2$ obtained fitting each muon track of Pavia sample with a parabola.

is reached at a distance $d \sim 90$ cm (corresponding to 60 cm from the cathode) for the simulation, while in real data it is shifted of 10 cm towards the anode ( $d \sim 80$ cm).

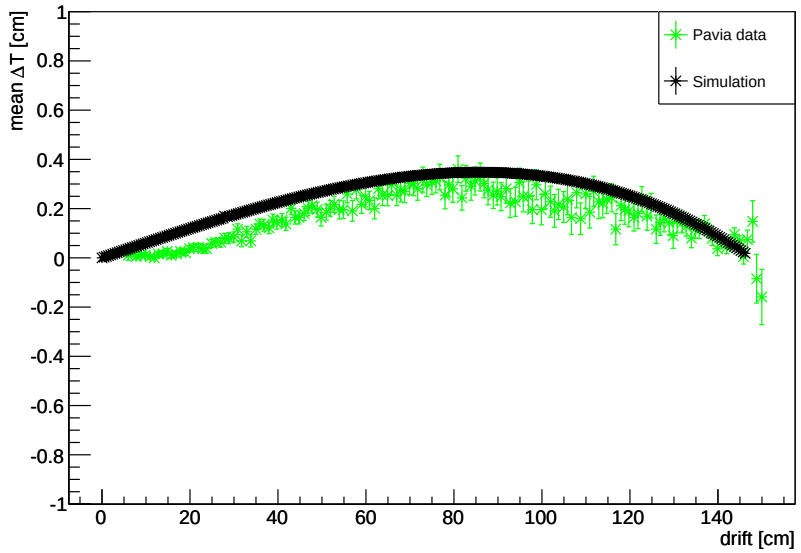


Figure 4.13: Comparison between Pavia data sample (green points) and simulation of space charge effects due to high cosmic ray flux at surface (black points). The anode position corresponds to the 0 in drift coordinate, while the cathode position is at 150 cm.

### 4.2.2 Results on LNGS data

The easiest way to link the previous results to space charge effects is to analyse cosmic ray data collected underground at LNGS, where the cosmic ray flux is much smaller then at surface and these effects should be negligible. In underground conditions muon bundles are not frequent as at surface, so I used single muon events, like that in Fig. 4.14.
A sample of 76 muon tracks have been then analysed with the same method and `Qscan` classes described in Sec. 4.2. As expected, in LNGS sample, the result is compatible with the absence of space charge effects. In fact, as shown in Fig. 4.15, where the $\Delta T$ parameter is plotted as a function of the drift coordinate, points are well distributed along a straight line. The corresponding distribution of bending parameters showed in Fig. 4.16 confirms this result, with a $\Delta T_{mean} \sim 0.04$ cm and a RMS of $\Delta T_{error} \sim 0.37$ cm.
Another confirmation of absence of space charge effects in the LNGS run, is the curve obtained averaging $\Delta T$ for each centimetre of the drift path: no relevant deviations from the straight track are observed along the entire drift path (Fig. 4.17).

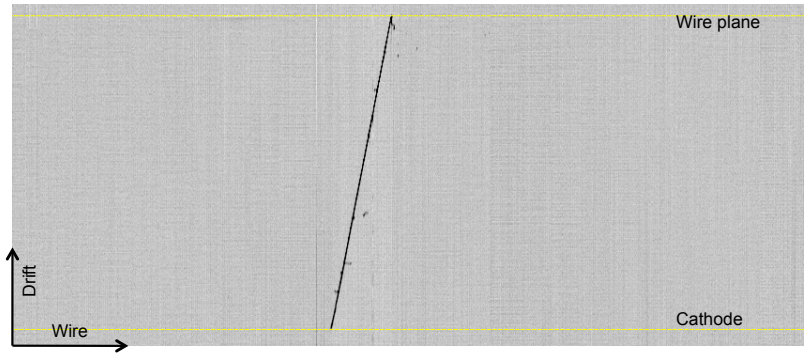


Figure 4.14: Example of cosmic muon recorded in Gran Sasso National Laboratories.

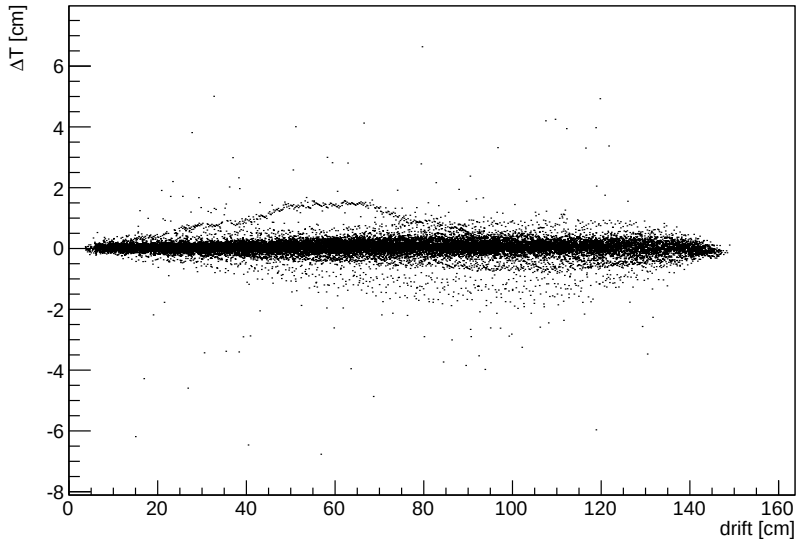


Figure 4.15: Plot of bending parameter $\Delta T$ in function of drift coordinate for all the track separately, for LNGS data sample. The anode position corresponds to the 0 in drift coordinate, while the cathode position is at 150 cm.

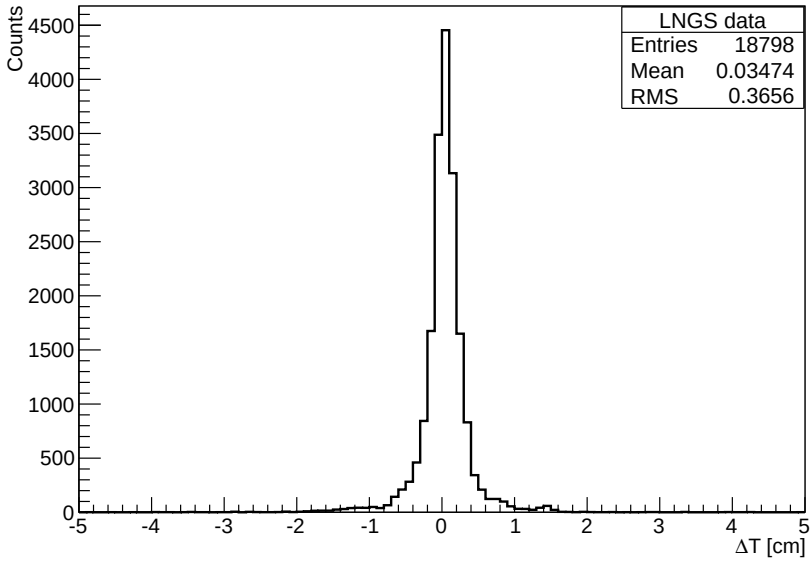


Figure 4.16: Distribution of bending parameter $\Delta T$ for the whole LNGS sample.

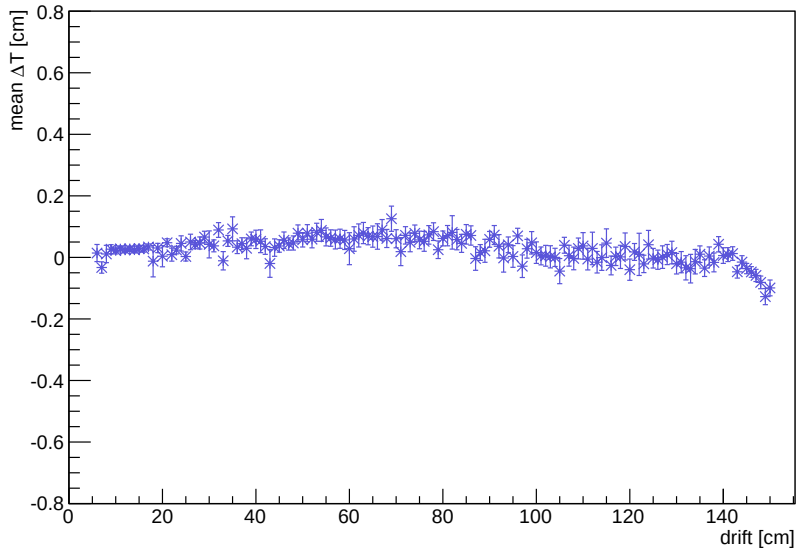


Figure 4.17: Average $\Delta T$ calculated for each centimetre of the drift path, considering the whole LNGS sample. The anode position corresponds to the 0 in drift coordinate, while the cathode position is at 150 cm.

### 4.2.3 Results considering Pavia data in the two chambers separately

To better understand if the curvature measured in the Pavia surface sample is due to space charge or to other effects, the analysis is repeated considering separately the left and right TPC chambers of the T300 module. The number of muon tracks are similar: 69 muon for the left chamber and 60 muons for the right chamber. The two chambers show a different behaviour: in the right chamber the bending is marginal, while in the left one the effect is more accentuated, as we can see in Fig. 4.18-4.22.

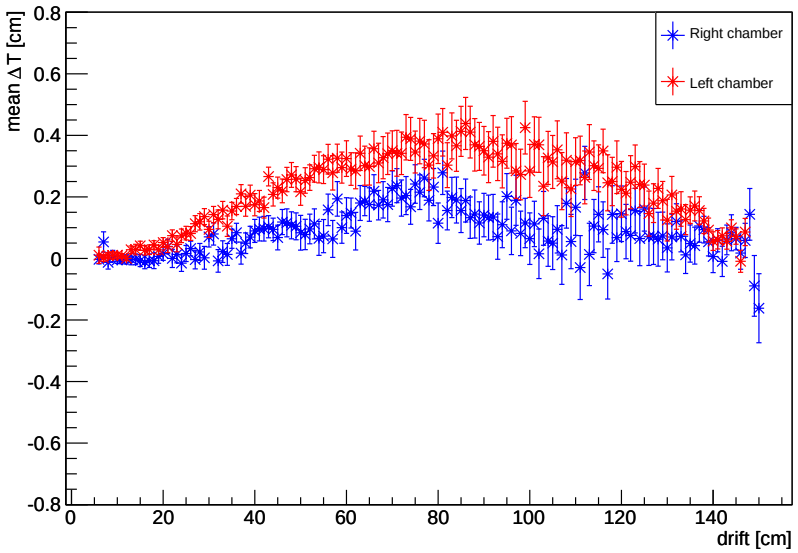


Figure 4.18: Results for Pavia data sample divided between left and right TPC chamber of T300 module. The anode position corresponds to the 0 in drift coordinate, while the cathode position is at 150 cm.

This different result can not be explained in terms of space charge. However, the two TPC chambers were at different thermal conditions: only the right one was close to the other T300 module that was cooled down, even if it was not filled by LAr. These different conditions created a temperature gradient that could cause convective motion and thus different distribution of positive ions in the two chambers.

## 4.3 Conclusions

Results here presented suggest the presence of small space charge effects inside the ICARUS T300 detector operated at surface in Pavia 2001 run, with a maximum track bending $\Delta T_{max} \sim 0.34$ cm. The analysis of a cosmic muon sample

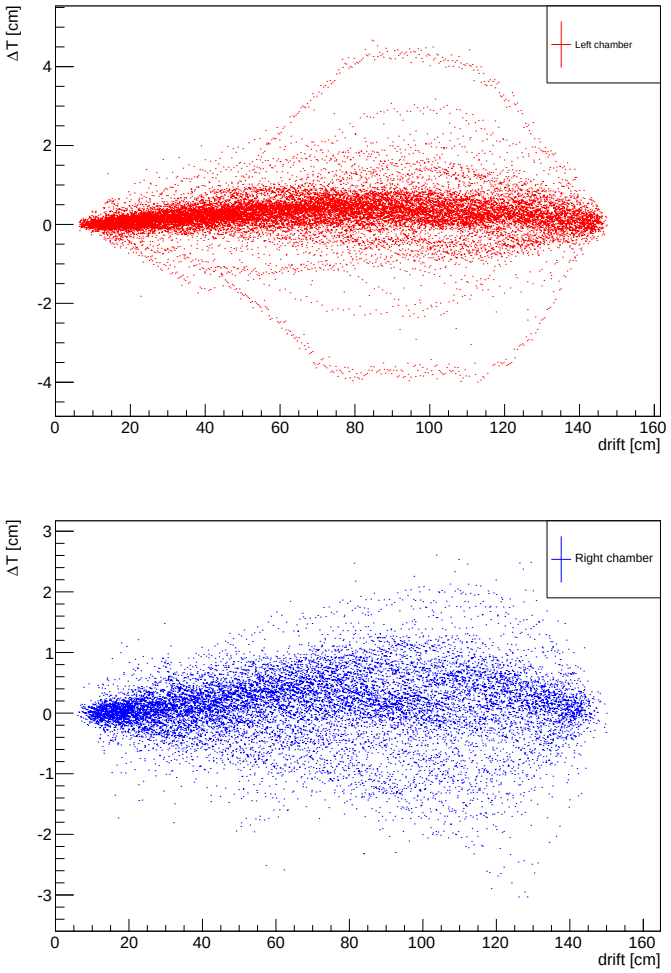


Figure 4.19: $\Delta T$ bending parameters for Pavia data sample evaluated separately for left chamber (top) and right chamber (bottom) of the T300 module. The anode position corresponds to the 0 in drift coordinate, while the cathode position is at 150 cm.

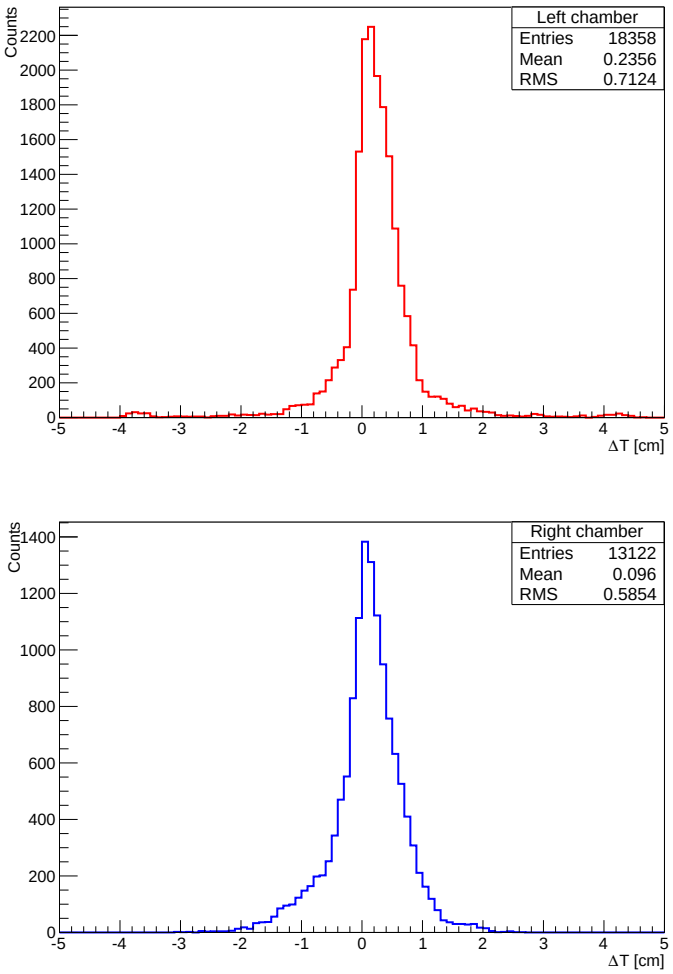


Figure 4.20: Distribution of $\Delta T$ parameters for Pavia data sample evaluated separately for left chamber (top) and right chamber (bottom) of the T300 module.

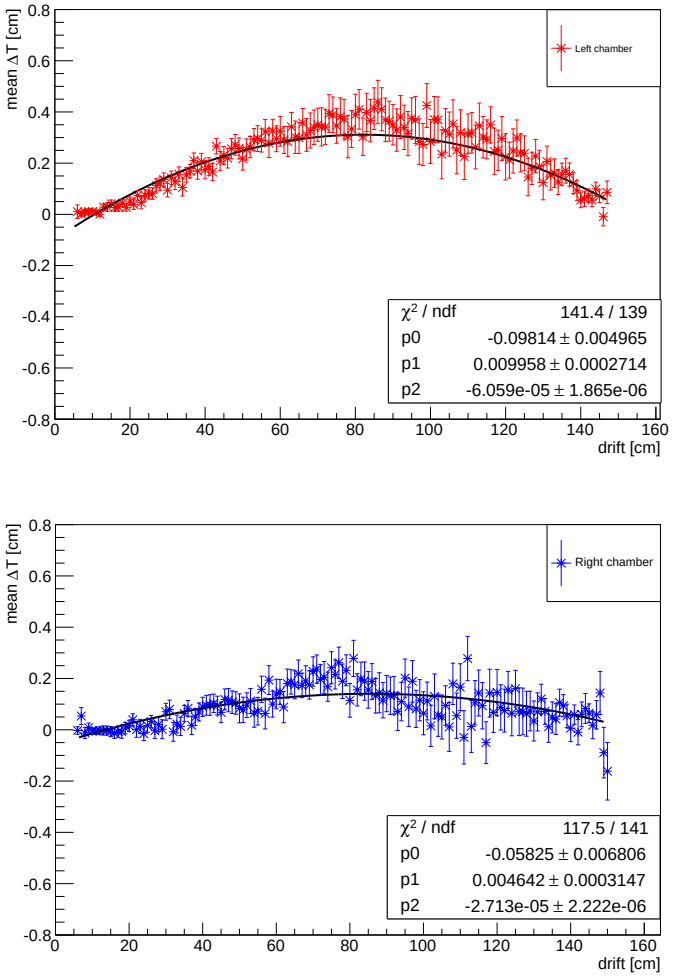


Figure 4.21: Average $\Delta T$ parameters evaluated for Pavia data sample separately for left chamber (top) and right chamber (bottom) of the T300 module. The results are fitted by a parabolic function (black lines) and fit parameter are shown. The anode position corresponds to the 0 in drift coordinate, while the cathode position is at 150 cm .

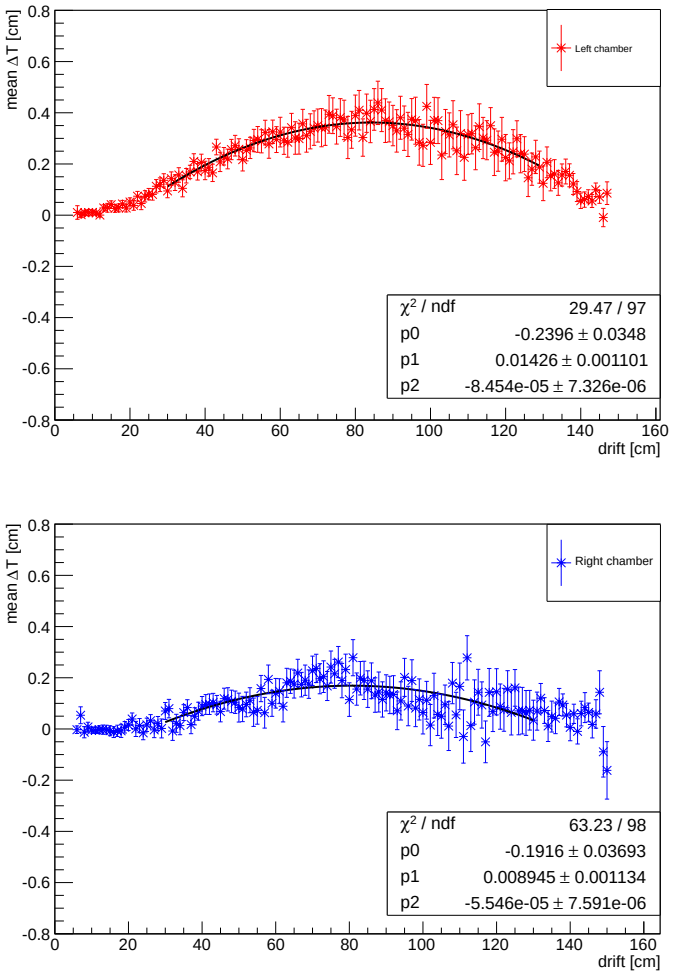


Figure 4.22: Average $\Delta T$ parameters evaluated for Pavia data sample separately for left chamber (top) and right chamber (bottom) of the T300 module. These curves are then fitted with a parabolic function (black line) in the range [30, 130] cm, where the curvature seems more evident. The anode position corresponds to the 0 in drift coordinate, while the cathode position is at 150 cm. The fitting parameters are also shown.

collected underground at LNGS, where this effect should not be present, produced a $\Delta T$ flat distribution, confirming that the track distortion observed at surface could be indeed due to space charge effects.
On the other hand, by analysing the left and the right T300 chambers separately, the bending clearly appears only in the left chamber: this behaviour can not be directly ascribed to space charge effects, but it can be due to the different conditions in which the two chamber worked in Pavia.
I can conclude that space charge effects should not be a problem for the ICARUS T600 detector at surface, because the observed track bending $\Delta T$ is however within the spatial resolution. But this effects could be important for detectors with longer drift path, such as MicroBooNE (see Chap. 2) or ProtoDUNE, a prototype for the future Deep Underground Neutrino Experiment (DUNE) (see [102] and Chap. 6) both of them placed at surface. The first one has a drift length of 2.56 m, while the second one of 3.6 m, dimensions much larger than the ICARUS ones.
The MicroBooNE Collaboration performed a Monte Carlo simulation in which the space charge effects results to modify the electric field by roughly 5% in both the drift and transverse direction [103]. The same simulation have been performed for ProtoDUNE, where these effects are estimate to induce distortion of $\sim 5$ cm in every track [104].

Chapter 5

# Electron diffusion measurement

To fully optimise the extraction of the intrinsic physical information from the signal recorded by the TPC it is essential to know the transport process of electrons in LAr. In particular, the diffusion of electron drifting in the electric field from the point of ionization to the anode plane represent an important term affecting the spatial resolution of the detector.
Diffusion process is described by Fick's law, where the diffusion parameter depends on electron mobility in the medium and on its temperature. From experimental point of view, diffusion can be measured considering the width of the signal recorded with different values of electric field.
For this purpose, dedicated measurements were performed with the ICARUS T600 detector during its operation at LNGS (see Chap. 2): in this case the diffusion measured is the longitudinal one, because the transversal diffusion is hidden by the detector geometric characteristics (i.e. the 3 mm wires pitch).
The longitudinal diffusion parameter was already evaluated by the ICARUS collaboration in 1994, when a 3 ton prototype of the T600 detector was placed at surface for a R&D run, but with different LAr temperature and pressure conditions with respect to the LNGS installation [59].

## 5.1 Theory of electron diffusion in electric field

Let's consider a group of electrons drifting in a uniform electric field region containing a medium at a given density. Electrons that survive the recombination process with the associated positive ions, are drifted under the action of the electric field and spread by diffusion. The diffusion process is illustrated in Fig. 5.1.
In general, the initial electron energy distribution has not steady state characteristic in that medium, and diffusion as well as drift rates will change as the cloud moves away from the initial point. Most of these changes occur until the electrons travel a distance which permits a balance between electrons gaining energy from electric field and losing energy through elastic collisions with the

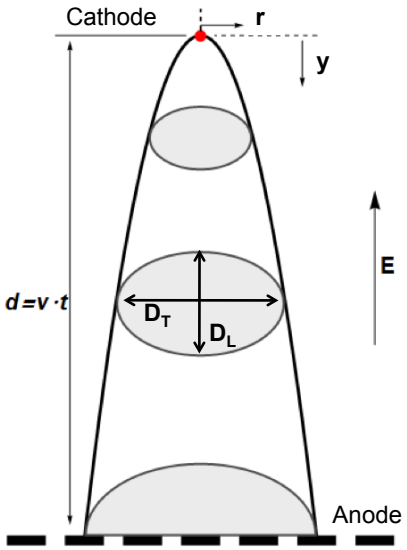


Figure 5.1: Illustration of the diffusion process starting from a point $r$ to the anode plane. The shaded ellipses in the figure are the shapes of the electron cloud. The two components longitudinal and transversal ($D_L$ and $D_T$ respectively) of the diffusion process are also enlightened.

medium molecules. At this point the electron cloud reaches a steady state described by the so called conventional approach (see Sec. 5.1.1).
This two component balance is applicable when electron density is spatially uniform, but, when it is not, diffusion current is present. Thus the balance has to include also the effects of the electron gaining energy through the field acting on the diffusion current, modifying the conventional transport theory. This situation is described by the semiquantitative model (see Sec. 5.1.2).

### 5.1.1 The conventional approach

The conventional approach theory describes the electron cloud when the rate at which electrons gain energy from the field is equal to the rate at which they lose energy through elastic collisions with medium atoms, reaching thus a steady state [105]. In this case, the electron density inside the cloud is spatially isotropic and follows the equation of continuity (Fick's equation [106, 107]):

$$\frac{\partial \rho}{\partial t} = D_T \left( \frac{\partial^2 \rho}{\partial x^2} + \frac{\partial^2 \rho}{\partial z^2} \right) + D_L \frac{\partial^2 \rho}{\partial y^2} - v \frac{\partial \rho}{\partial y}, \tag{5.1}$$

where $\rho \equiv \rho(x, y, z, t)$ is the electron density distribution at position $(x, y, z)$ and time $t$; $D_T$ is the diffusion parameter perpendicular to the electric field $E$ supposed aligned along the $y$ direction, $D_L$ is the longitudinal one along $y$ direction and $v$ is the velocity in the longitudinal direction in which the cloud moves. In this approximation, the Coulomb repulsion between electrons is not considered and, most important, diffusion is considered isotropic, i.e.

$D_L = D_T = D$.
At low fields, the electrons gain a little amount of energy from the elastic collisions that they undergo to come to thermal equilibrium with the medium. In this case, the diffusion coefficient $D$ can be expressed by the Einstein-Smoluchowski relation [108, 109]:

$$D = \frac{\mu_e kT}{e}, \tag{5.2}$$

where $e$ is the electron charge, $k$ is the Boltzmann's constant, $T$ is the temperature of the medium and $\mu_e$ is the electron mobility (the electron drift velocity per unit of electric field $E$).
The solution of Eq. 5.1 represents the translation and spread of the cloud and it can be written as:

$$\rho(r, y, t) = \frac{N_0}{(4\pi Dt)^{3/2}} exp\left\{-\frac{r^2}{4Dt}\right\} exp\left\{-\frac{(y - vt)^2}{4Dt}\right\}, \tag{5.3}$$

where $r = x^2 + z^2$ is the transverse coordinate and $N_0$ is the total number of electrons in the cloud.
Integrating the electron density distribution 5.3 in the transverse coordinate, it is possible to obtain the linear density in electric field direction $y$:

$$\rho_L(y, t) = \frac{N_0}{(4\pi Dt)^{1/2}} exp\left\{-\frac{(y - vt)^2}{4Dt}\right\}. \tag{5.4}$$

When the drift path is large together with a small diffusion parameter, $\rho_L$ approaches a Gaussian distribution and it is possible to define the longitudinal spread of the electron cloud as its standard deviation:

$$\sigma = \sqrt{2Dt}. \tag{5.5}$$

This relation permits to calculate the diffusion parameter, measuring the spatial spread of the cloud as a function of the time: in fact, the cloud moves like a sphere that expands over time.

### 5.1.2 The semiquantitative model

As the field increases, the electrons gain energy from the field and the frequency of collision between electrons and atoms of the medium increases, such as the energy loss per collision. Therefore, the balance between gain and loss in energy is no more valid and inside the cloud an energy gradient is present, causing a disuniformity in electron density inside it. Therefore we can write [105]:

$$\frac{2m}{M}\nu\epsilon_m\rho = -e\vec{E}\cdot\vec{\Gamma}, \tag{5.6}$$

where $\nu$ is the electron collision frequency, $\frac{2m}{M}$ is the fractional energy loss per collision ($M$ and $m$ are the atomic and electron masses respectively) and $\epsilon_m$

is the electron mean energy. The particle current density $\vec{\Gamma}$ induces a density gradient inside the cloud:

$$\vec{\Gamma} = -\mu\rho\vec{E} - D\nabla\rho. \tag{5.7}$$

With these definitions and considering the electric field along $y$ coordinate ($E_x$=$E_z$=0) , the Eq. 5.6 becomes:

$$\frac{2m}{M}\nu\epsilon_m = e\mu E^2 - eED\frac{1}{\rho}\frac{\partial\rho}{\partial y}. \tag{5.8}$$

We consider that the collision frequency is constant, so the mobility is $\mu = e/m\nu$ and the diffusion $D = 2\epsilon_m/3m\nu$ . If the density gradient term is null, the electron energy is defined as:

$$\epsilon_0 = \frac{M}{2m^2}(\frac{eE}{\nu_0})^2, \tag{5.9}$$

where $\nu_0$ is the electron collision frequency evaluated with $\epsilon_0$. Assuming that the effect of density gradient on the electron energy is small, substituting the expression $\epsilon_m = \epsilon_0 + \Delta\epsilon$ and $\nu = \nu_0 + \partial\nu/\partial\epsilon|_0\Delta\epsilon$ into the Eq. 5.8 and solving for $\Delta\epsilon$, we can express $\epsilon_m$ as:

$$\epsilon_m = \epsilon_0\left[1 - \frac{2\epsilon_0}{3eE\left(\frac{\partial\nu}{\partial\epsilon}|_0\frac{\epsilon_0}{\nu_0}\right)}\frac{1}{\rho}\frac{\partial\rho}{\partial y}\right]. \tag{5.10}$$

The equation above expresses the fact that $\epsilon_m$ is grater then $\epsilon_0$ when the diffusion current is added to the drift current and is smaller when diffusion is subtracted to the drift current. Therefore, the electron energy becomes a function of the position.
Using this expression of $\epsilon_m$, the current density in Eq. 5.7 can be expressed as:

$$\vec{\Gamma} = \mu_0 E\rho\hat{k} - D_0\left(\frac{\partial\rho}{\partial x}\hat{i} + \frac{\partial\rho}{\partial z}\hat{j}\right) - D_0\left(1 - \frac{\gamma}{1+2\gamma}\right)\frac{\partial\rho}{\partial y}\hat{k}, \tag{5.11}$$

where $\mu_0$ and $D_0$ are referred to $\epsilon_0$ and the quantity $\gamma$ is defined as:

$$\gamma \;=\; (\epsilon_0/\nu_0)\;\partial\nu/\partial\epsilon\;|_0. \tag{5.12}$$

We can notice that while the coefficient describing transversal diffusion corresponds to the usual diffusion coefficient $D_T = D_0$, the coefficient for longitudinal diffusion is modified due to the dependence of $\mu$ on the derivative of $\rho$. Therefore it can be defined as :

$$D_L = D_T\left[1 - \frac{\gamma}{1+2\gamma}\right]. \tag{5.13}$$

It is evident that $D_L$ can be grater or smaller than $D_T$ depending on how the frequency collision $\nu$ changes with energy:

$$\begin{cases} D_L = D_T = D_0 & \text{if } \frac{\partial \nu}{\partial \epsilon} \mid_0 = 0 \text{ (conventional approach);} \\ D_L < D_T & \text{if } \frac{\partial \nu}{\partial \epsilon} \mid_0 > 0; \\ D_L > D_T & \text{if } \frac{\partial \nu}{\partial \epsilon} \mid_0 < 0. \end{cases} \tag{5.14}$$

Eq. 5.13 also indicates that $D_L$ can differ significantly from $D_T$ when $\nu$ varies by an appreciable fraction over an energy interval equal to $\epsilon_0$. If we take $\nu$ to vary as

$$\nu = \nu_0 (\epsilon_m / \epsilon_0)^{(l+1)/2} \tag{5.15}$$

where $l$ is an integer, then the ration $D_L/D_T$ becomes:

$$\frac{D_L}{D_T} = \frac{l+3}{2(l+2)}. \tag{5.16}$$

We can come back to the conventional approach $D_L = D_T$ if $l$ =-1, that means $\nu$ constant.
The difference between the two components of the diffusion arises from the change in drift velocity $v_{drift} = \mu E$, that is associated with the increase (or decrease) of the energy caused by the electric field acting on the diffusion part of the current. In this case, also the shape of the cloud changes.
The ratio of the longitudinal and transverse diffusion coefficient can be expressed also in terms of the Einstein's relation in Eq. 5.2:

$$\frac{D_L}{D_T} = 1 + \frac{E}{\mu_i} \frac{\partial \mu_i}{\partial E}, \tag{5.17}$$

considering a quantitative relation between diffusion and mobility for electrons at high electric field [110, 111]:

$$D_T = \frac{kT\mu_i}{e}, D_L = \frac{kT}{e} \left( \mu_i + E \frac{\partial \mu_i}{\partial E} \right). \tag{5.18}$$

## 5.2 Evaluation of electron diffusion parameter in the ICARUS T600 detector

In this section we will see how to evaluate longitudinal diffusion in a LAr TPC and some preliminary results: this evaluation is possible using the ICARUS T600 cosmic ray data collected during LNGS run.
After the shutdown of the CNGS beam, T600 detector was used to collect data with cosmic rays trigger; dedicated runs were performed to evaluate, among others, also the electron diffusion parameter. These runs collected data at six different electric field values: $E$ = [270, 360, 500, 600, 700, 978] V/cm.
The detector has been designed to have a wire pitch (0.3 cm) bigger than the

amount of transverse diffusion, so it is sensitive only to the longitudinal one, along the drift axis. The evaluation of diffusion parameter can be done with Eq. 5.5, that, expressed with measurable quantities, becomes:

$$\sigma_t^2 = \frac{2Dt}{v_{drift}^2}, \tag{5.19}$$

where $\sigma_t$ is the spread of the signal due to diffusion process, $v_{drift}$ is the drift velocity and $t$ is the drift time registered by the wire. This expression differs from Eq. 5.5, where the $\sigma$ is expressed in length unit, because here $\sigma_t$ is expressed in time unit; this leads to the presence of the drift velocity $v_{drift}$. The diffusion parameter $D$ can be expressed by the formula:

$$D = \frac{\sigma_t^2 v_{drift}^2}{2t}, \tag{5.20}$$

The sample used to evaluate $D$ consists of cosmic muons collected at different electric fields. I select each muon track by the visual scanning procedure and then 3D reconstructed as described in Chap 3. This sample is composed by roughly 33 muons for each electric field value.
Following the Eq. 5.20, the variables that we need to know are $v_{drift}$, $t$ and $\sigma_t$. The evaluation of these variables is made by proper classes that I developed within the`Qscan` analysis framework.
First of all, I have to calculate the drift velocity: from this value depends the calculation of the drift time and consequently the whole reconstruction procedure.

### 5.2.1 Drift velocity evaluation

The first step for the evaluation of diffusion parameter is the calculation of the drift velocity for each electric field value. In fact from this value depends a faithful reconstruction of events: with an higher value of the electric field, the drift time reduces because the drift velocity increases. This is shown in Fig. 5.2, where we can see muon tracks crossing the same drift distance from the cathode to the wire planes but at different electric fields: since the drift time depends on the drift velocity, the drift coordinate is shorter for muons recorded at higher electric fields [112, 113, 114, 115].
It is possible to obtain the drift velocity value, considering muon tracks that pass both wire and cathode planes, because they cover a fixed drift length of 1482 mm, due to the mechanical structure of the detector. A further selection is made by visual scanning, in order to consider only muon with this feature. Once I identify a good event, the values of the first and last hits are used to calculate the drift velocity, taking into account the fixed distance that muons travelled. Averaging the values found in every selected track, it is possible to calculate $\langle v_{drift} \rangle$ for each electric field value $E$, as tabulated in Tab. 5.1.
Along the drift path, the drift velocity follows the square root function of the electric field [112, 113, 114, 115], as we can see from the plot in Fig. 5.3, where

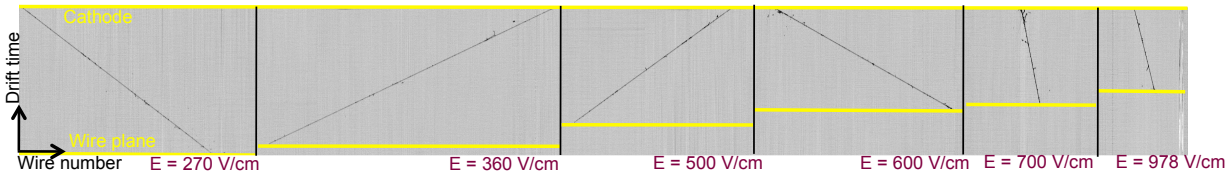


Figure 5.2: Muon tracks recorded underground at different electric field values. As enlightened in the pictures, the drift coordinate seems to reduce by increasing the electric field value, due to higher drift velocity.

| $E$ [V/cm] | $\langle v_{drift} \rangle$ [cm/$\mu$s] |
|---|---|
| 270 | 0.12 $\pm$ 0.01 |
| 360 | 0.13 $\pm$ 0.02 |
| 500 | 0.16 $\pm$ 0.01 |
| 600 | 0.17 $\pm$ 0.01 |
| 700 | 0.18 $\pm$ 0.01 |
| 978 | 0.21 $\pm$ 0.02 |

Table 5.1: Values of drift velocity $\langle v_{drift} \rangle$ calculated with different electric fields $E$.

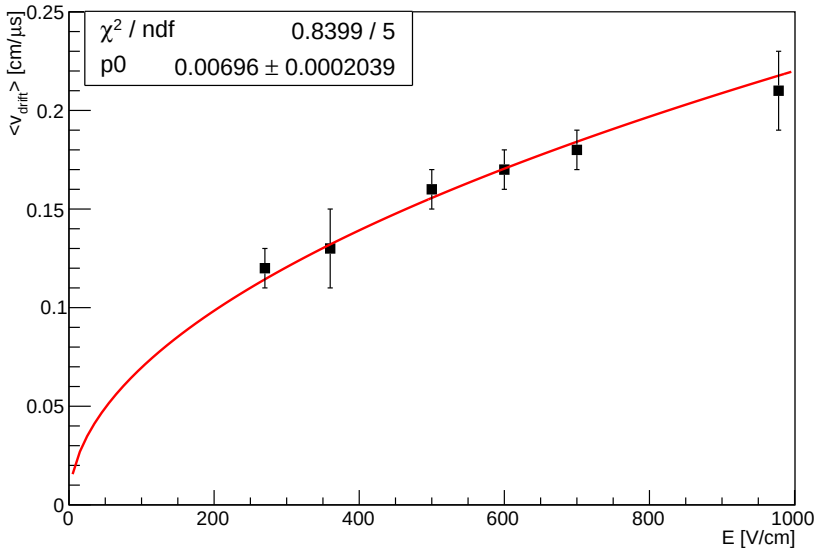


Figure 5.3: Electron drift velocity $\langle v_{drift} \rangle$ as a function of the electric field value $E$. The red line is the fit function $f(E) = p_0\sqrt{E}$.

the red curve corresponds to the ROOT fit line given by: $f(E) = p_0\sqrt{E}$. The drift velocities found in this step are used in the reconstruction algorithm (see Chap. 3).

### 5.2.2 Evaluation of longitudinal diffusion parameter

The longitudinal diffusion is calculated using the relation in Eq. 5.20, where the main role is played by the width of the signal.
After the calculation of the drift velocity, each muon sample is processed with the Qscan hit finding procedure. As described in Chap. 3, a hit is defined and fitted by the function:

$$f(t) = B + A\frac{e^{-(t-t_0)/\tau_1}}{(1+e^{-(t-t_0)/\tau_2})} \tag{5.21}$$

where $B$ is the fit baseline of the signal, $A$ is the amplitude, $t_0$ is the peak coordinate and $\tau_1$ and $\tau_2$ are rising and falling time constants, respectively. Once a hit is found, in order to retrieve the signal width information, it is convenient to compute numerically the integral of the hit function. The integral is then fitted by the sigmoid function:

$$f(t) = B + A\left(1 - \frac{1}{1+e^{\frac{t-t_0}{w}}}\right), \tag{5.22}$$

where $B$, $A$ and $t_0$ are defined as in fitting function in Eq. 5.21, while $w$ is the time width of the signal. Fitting every hit with this function, it is possible to retrieve the parameters that characterize the sigmoid function. Fig. 5.4 compares the signal fitted by function in Eq. 5.21 to the same resulting from the sigmoid fit in Eq. 5.22.
Each muon track is previously cleaned from delta rays (as explained in Chap. 3), otherwise the signal width can be overestimated.
The next step of this analysis is the identification of muon clusters and their 3D reconstruction: an example of cosmic muon registered at $E = 270$ V/cm and all steps of its complete reconstruction are shown in Fig. 5.5.
At this point it is possible to measure the signal width $w$, defined as the temporal distance between 5% and 95% of sigmoid maximum value, as depicted in Fig. 5.4.
Therefore, from the sigmoid function, I retrieve $w$: it is the quadratic sum of two contributions, one given by the diffusion process, $\sigma_t^2$, and the other by the electronics, $w_{el}^2$,

$$w^2 = w_{el}^2 + \sigma_t^2. \tag{5.23}$$

While $\sigma_t$ depends on the electric field value, the $w_{el}$ is a constant given by the electronic read-out.
Considering the Eq. 5.19, I notice that it is possible to fit linearly $\sigma_t^2$ as a function of drift time $t$ and retrieving $D$ as its slope. The use of $w^2$ instead

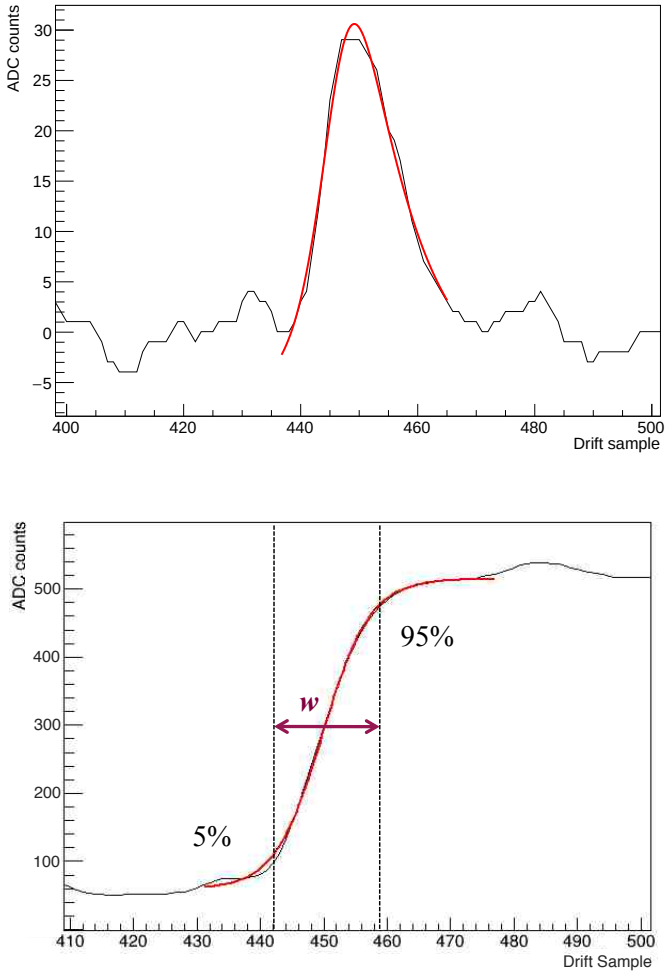


Figure 5.4: Signal of a cosmic muon event recorded at $E = 270$ V/cm, registered in single wire. Top: hit fitted by the function in Eq. 5.21. Bottom: integral of the wire signal, fitted with the sigmoid function in Eq. 5.22.

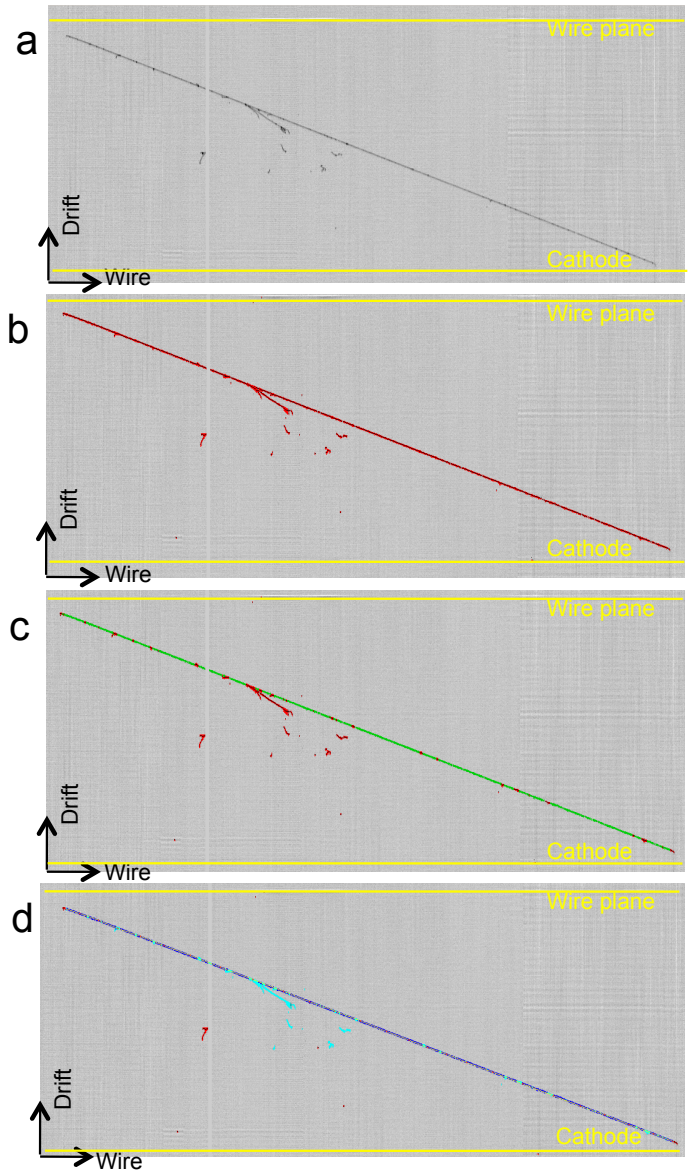


Figure 5.5: Example of cosmic muon recorded at $E = 270$ V/cm and steps for its reconstruction: (a) raw event; (b) result of hit finding procedure, with every track point corresponding to a hit (red points); (c) muon cluster building (green points), with the removal of delta rays; (d) muon track 3D reconstruction (dark blue points), with light blue points corresponding to delta rays.

of $\sigma_t^2$, however adds only a constant term, being $w_{el}^2$ independent by drift time and electric field; the slope, and so $D$, remains unaffected.
Considering $f(t) = w^2 \cdot v_{drift}^2$, it is fitted with the linear function `pol1` defined in `ROOT` [101]

$$f(t) = p_0 + p_1 \cdot t, \tag{5.24}$$

where $p_1 = 2D$ and $p_0$ accounts for the constant term.
I made the linear fit dividing the drift path in bins of 50 $\mu$s: the number of bin in not constant and it is tabulated in Tab. 5.2.
Considering the $w$ value given by the sigmoid fit for all the tracks, I calculate the mean $w$ in each bin. Then the linear fit of $w^2 \cdot v_{drift}^2$ as a function of the drift time is performed for each electric field values $E$, as show in Fig. 5.6 - 5.8.

| $E$ $[V/cm]$ | Number of bins |
|---|---|
| 270 | 25 |
| 360 | 22 |
| 500 | 18 |
| 600 | 17 |
| 700 | 15 |
| 978 | 14 |

Table 5.2: Number of bins used to calculate the diffusion for each electric field value. The width of every bin is constant: 50 $\mu$ s.

As we can see in Fig. 5.6 - 5.8, some error bars are big: this is probably due to the small sample I analysed. Nevertheless, considering each $p_1$ given by the fit, it is possible to calculate the diffusion parameter $D$ for each value of the electric field $E$, and the values are tabulated in Tab. 5.3 and shown in the plot in Fig. 5.9.

| $E$ $[V/cm]$ | $D$ [cm$^2$/s] |
|---|---|
| 270 | 4.38 $\pm$ 1.41 |
| 360 | 5.78 $\pm$ 2.28 |
| 500 | 3.84 $\pm$ 2.96 |
| 600 | 4.74 $\pm$ 3.51 |
| 700 | 6.27 $\pm$ 4.15 |
| 978 | 4.59 $\pm$ 5.35 |

Table 5.3: Diffusion parameter $D$ calculated for each electric field value $E$.

These values are compatible with a diffusion parameter, $D = 4.74 \pm 2.04$ cm$^2$/s, independent from the electric field values, as expected [105, 116]. The error is somewhat large, probably due to the small sample analysed, so analysis with more statistics will be performed.

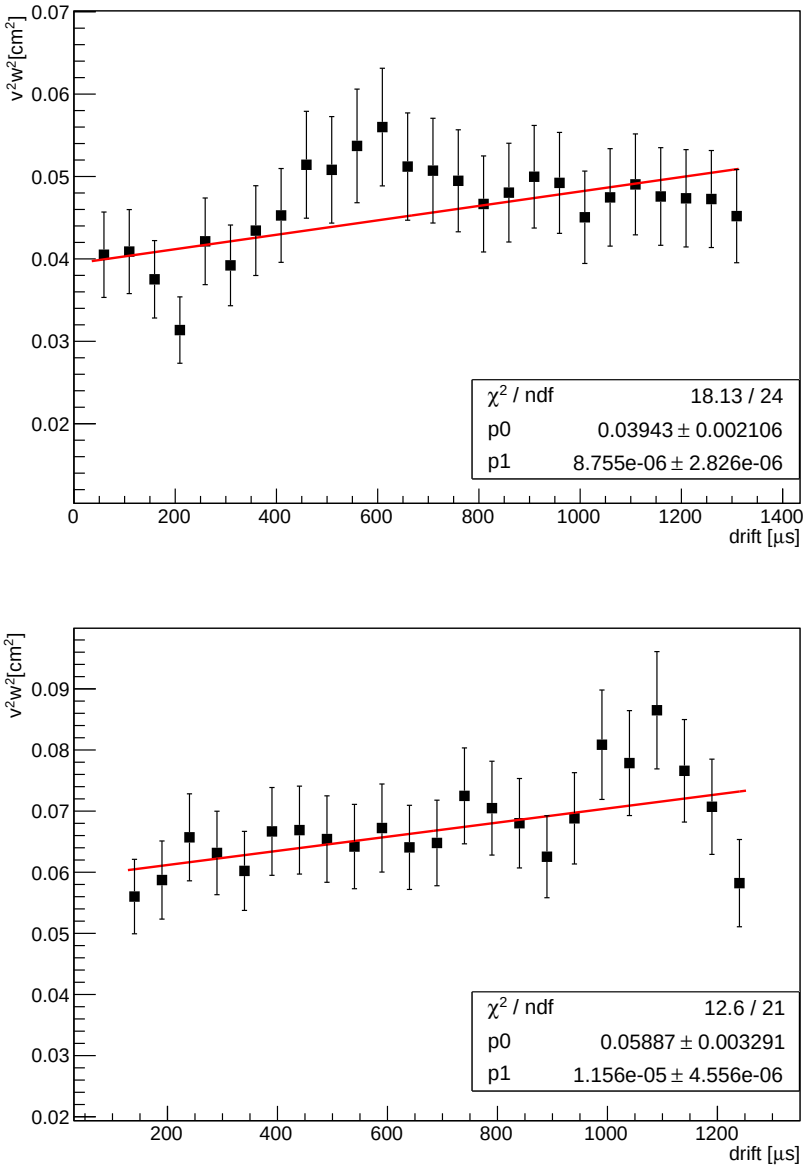


Figure 5.6: Signal width $w^2$ as a function of drift time for $E = 270$ V/cm (top) and $E = 360$ V/cm (bottom). Each drift time bin is 50 $\mu$ s large. Plots are fitted with a linear function and fitting parameter are shown.

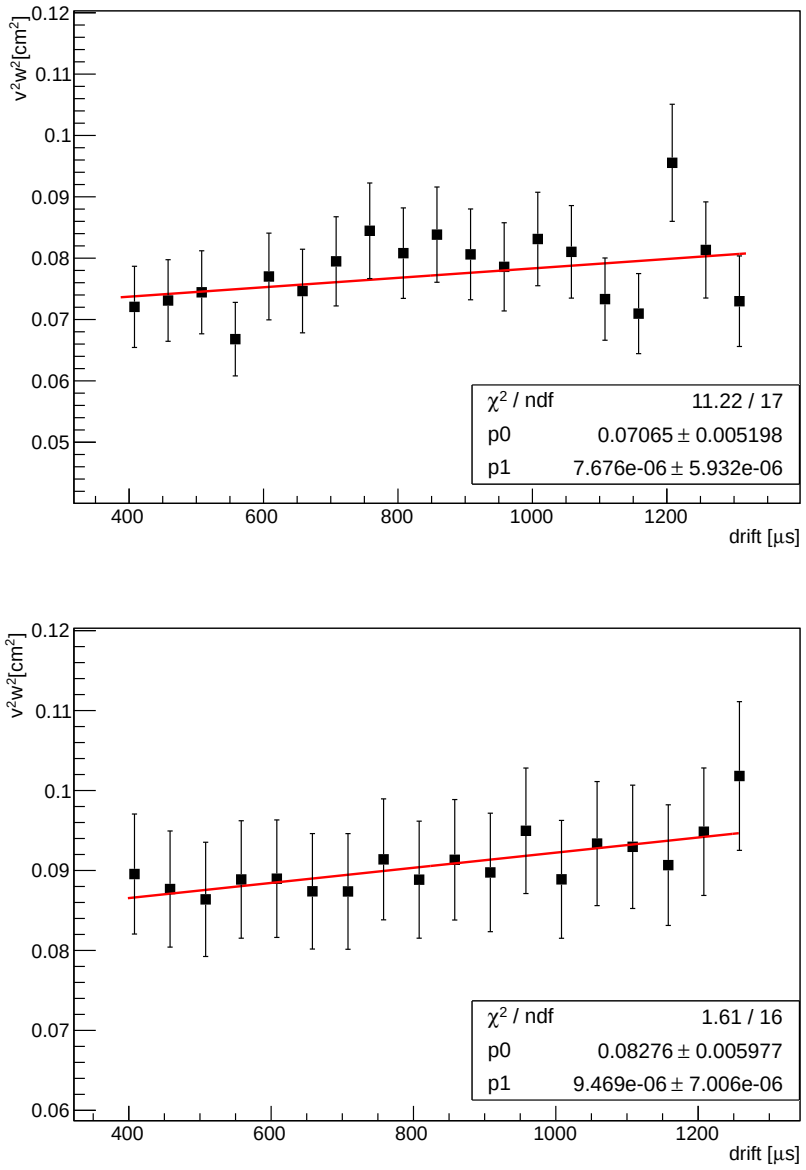


Figure 5.7: Signal width $w^2$ as a function of drift time for $E = 500$ V/cm (top) and $E = 600$ V/cm (bottom). Each drift time bin is 50 $\mu$ s large. Plots are fitted with a linear function and fitting parameter are shown.

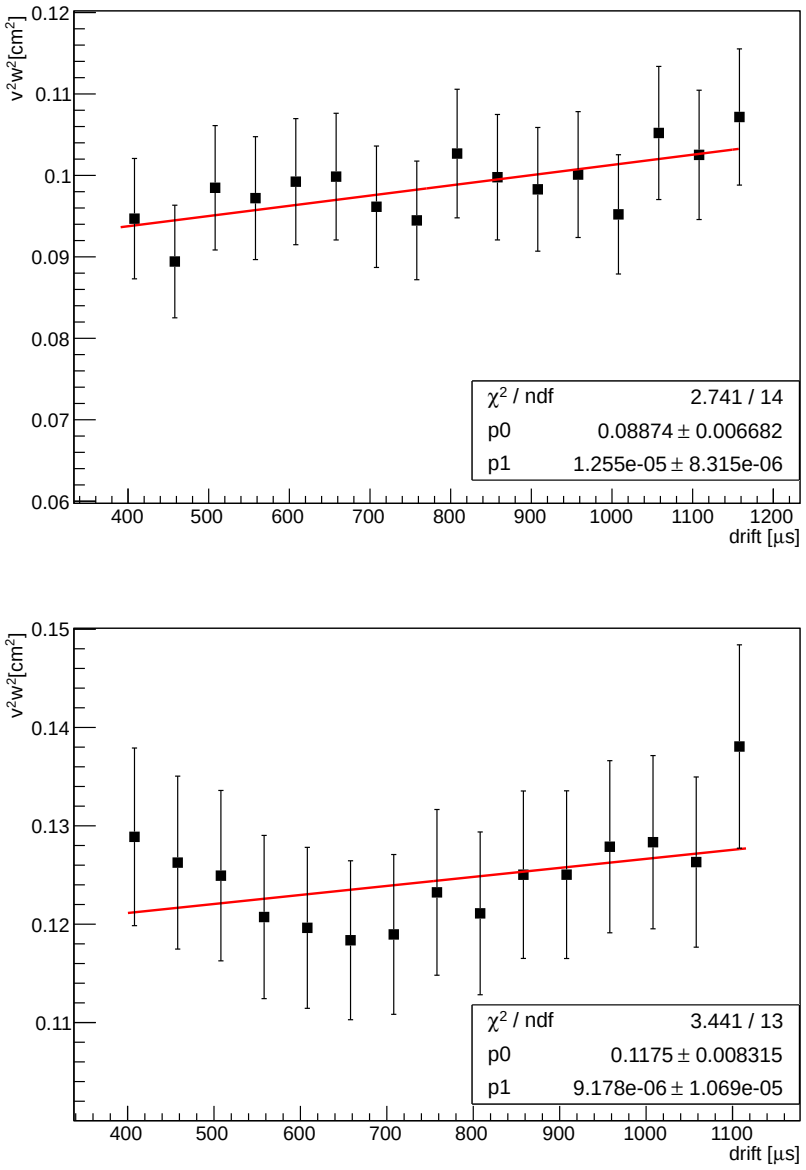


Figure 5.8: Signal width $w^2$ as a function of drift time for $E = 700$ V/cm (top) and $E = 978$ V/cm (bottom). Each drift time bin is 50 $\mu$ s large. Plots are fitted with a linear function and fitting parameter are shown.

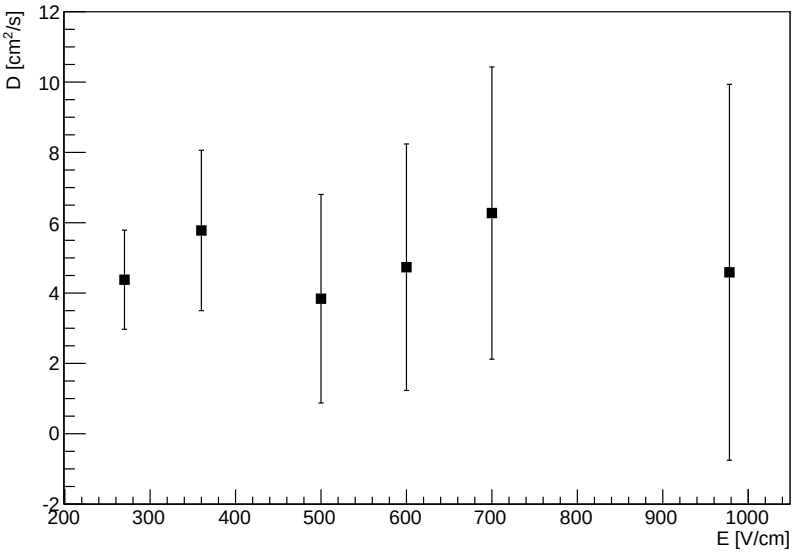


Figure 5.9: Diffusion parameter $D$ as a function of electric field $E$.

## 5.3 Conclusions

Longitudinal diffusion parameter is an important quantity contributing to the spatial resolution of LAr TPC detectors. Dedicated measurements were performed in underground conditions with the ICARUS T600 detector.
Experimentally, this parameter can be calculated measuring the width of the signal recorded by the TPC, with the procedure explained in Sec. 5.2.
Considering the signal width $w$ as a function of the drift path, it is possible to evaluate the diffusion parameter $D$, retrieving it from the slope of the linear fit, as shown in Fig. 5.6-5.8. I obtain a value of $D$ for each electric field $E$, compatible with a constant value $D = 4.74 \pm 2.04$ cm$^2$/s: however it is a preliminary results, because the errors are large due to the small statistic I analysed.
The ICARUS Collaboration evaluated the longitudinal diffusion parameter in 1994, with a 3 ton prototype placed at surface [59]. In that case, it was obtained $D = 4.8 \pm 0.2$ cm$^2$/s, but LAr temperature and pressure conditions were different and only a large sample of vertical cosmic ray muon were considered. In my analysis, I considered cosmic muons that cross the detector in each direction; the next step of this analysis is to selected vertical cosmic muons and enlarge the statistic.

Chapter 6

# Electron/positron separation in a magnetized LAr TPC

Once the short baseline experiment at Fermilab is finished, the T600 detector may be advantageously used as a near detector for the Deep Underground Neutrino Experiment (DUNE). It will be a long baseline experiment, with a multi-kiloton ($\sim$ 40 kton) modular LAr TPC as main far detector, placed deep underground in the Homestake Mine at Sanford Underground Research Facility (South Dakota), at 1300 km from the FNAL neutrino beam source [117]. The focus of the DUNE experiment is the determination of the neutrino mass hierarchy and the measurement of leptonic CP violation. Being the far detector deep underground, it will provide additional research opportunities in proton decay and neutrino astrophysics. The DUNE program is very ambitious and it foreseen to be completed in the next 20 years.
In this hypothesis the T600 could be equipped with an intense magnetic field, in order to obtain a precise particle momentum measurement and charge particle identification.
Some preliminary simulations have been already produced in order to understand the best configuration for the magnetic field system [89]. To achieve recognition and momentum measurement of charged particles, the best configuration is to have a magnetic field perpendicular both to the beam and to the drift direction. The reasonable intensity of the magnetic field inside the argon volume is $\sim$ 1 T. The purpose of the simulation is to evaluate the uniformity of the field inside the LAr volume. The Helmotz coil configuration have been proposed, with one or two sets of coils.
The first configuration, with a single set of coils is shown in Fig. 6.1. This simulated geometry is composed by an inner detector, conductive Helmholtz coils and an iron yoke. The inner detector is simulated as a single parallelepipedal volume, filled with LAr; its dimensions are $3 \times 6 \times 18$ m$^3$, as the whole T600 active volume. The coils are simulated as made of a perfect superconductive material; they are 1 m distant from the active volume and, in order to obtain the wanted magnetic field of $\sim$ 1 T, the total current value $i$ is set to 20 kA.

The iron yoke is used to have a contained return path and to significantly lower the residual magnetic field in the region around the detector.

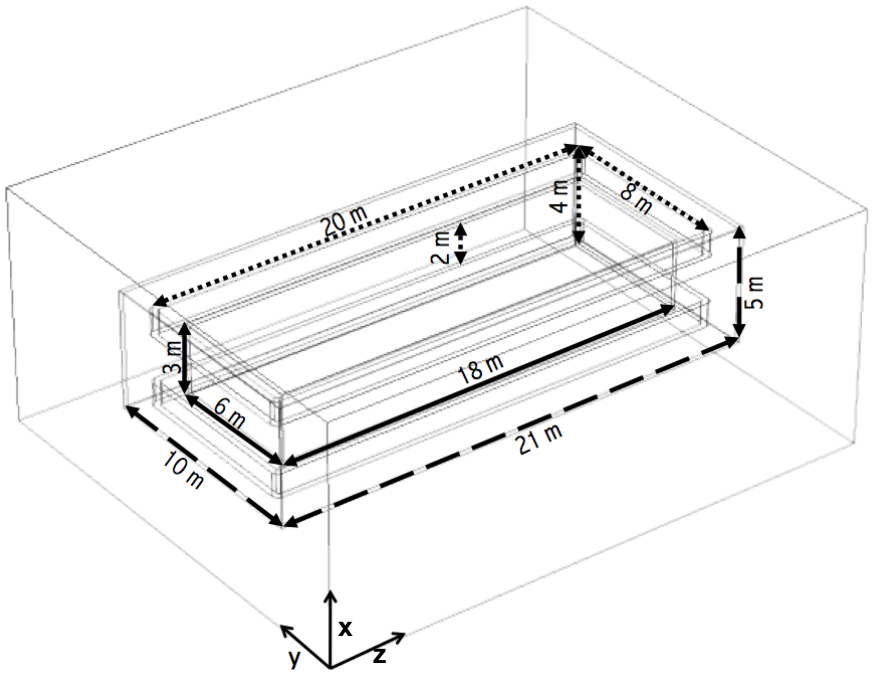


Figure 6.1: Simulation of the configuration with a single set of coils. Full lines refer to the dimension of the active argon volume, dotted lines to the dimension of the coils, while dashed lines to the dimension of the iron yoke.

The mean intensity of the module of the magnetic field results to be $\left|\bar{B}\right| = 0.92 \pm 0.12$ T with a spread of 13%, while the vertical component of the field is $\bar{B}_x = 0.92 \pm 0.12$ T and it represents the main component of the $\vec{B}$ field.
The second simulated configuration has two separate sets of coils, one for each T300 module (see Fig. 6.2), with the aim to improve the magnetic field containment, without losing in field uniformity. In this configuration the electric current flow with opposite direction in the two pairs of coils (i.e. clockwise and counterclockwise if seen from the top). In this case the active argon is simulated as two volumes, $3 \times 3 \times 18$ m$^3$ each, separated by 1 m, surrounded at 0.5 m by two pairs of coils. The distance between the coils and the iron yoke is the same as before, as well as the current circulating in the coils.
Using the same current as the previous configuration, the mean intensities of magnetic field in the active argon volume are $\left|\bar{B}\right| = 1.23 \pm 0.16$ T and $\bar{B}_x = 1.22 \pm 0.15$ T in both chambers, with the spread remaining at the level of 13%.
In this framework, I developed an algorithm for separation between $\nu_e$ and $\bar{\nu}_e$, and it will be described in the following.

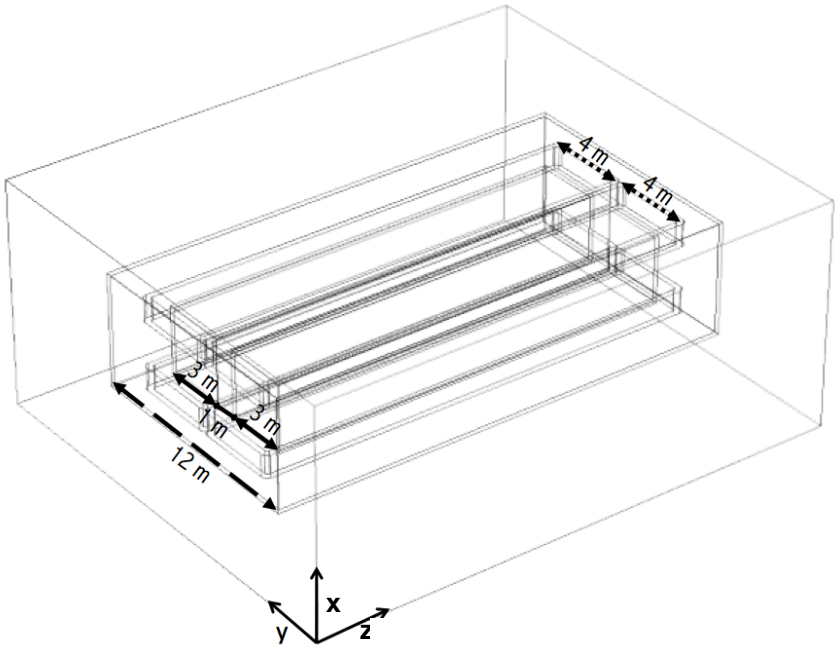


Figure 6.2: Simulation of the configuration with two set of coils. Full lines refer to the dimension of the active argon volume, dotted lines to the dimension of the coils, while dashed lines to the dimension of the iron yoke.

## 6.1 Study on electron/positron identification

The hypothesis of magnetizing the ICARUS T600 active volume has the aim of allowing to distinguish if the incoming particle is a neutrino or an anti-neutrino. In this framework, a dedicated algorithm has been developed to recognise electrons and positrons produced in electron neutrino charged current interactions, looking for one or more parameters that characterize these two particles. I develop this algorithm adapting at this case the classes in the `Qscan` analysis framework (see Chap. 3) and I test it using a Monte Carlo sample.

### 6.1.1 The Monte Carlo sample

In order to test this algorithm, the full ICARUS T600 detector simulation [120], based on the Fluka package [118, 119], was used.
In this simulation, $\nu_e$ and $\bar{\nu}_e$ with energy $E_\nu$=500 MeV are generated and made to interact within the detector, with a total of 2000 events equally divided between the two categories of particles. The active volume is supposed to be permeated by 1 T uniform magnetic field, perpendicular to both the drift and beam directions. An example of these kind of events is reported in Fig. 6.3, where both electron and positron are shown. The simulation represents an ideal case, where only electrons/positrons are supposed to origin from the vertex, while in a realistic case also other interactions can be present, such as nuclear recoil or products from the fragmentation of the nuclei.
Starting from this sample, the algorithm for identification between $\nu_e$ and $\bar{\nu}_e$ can be developed.

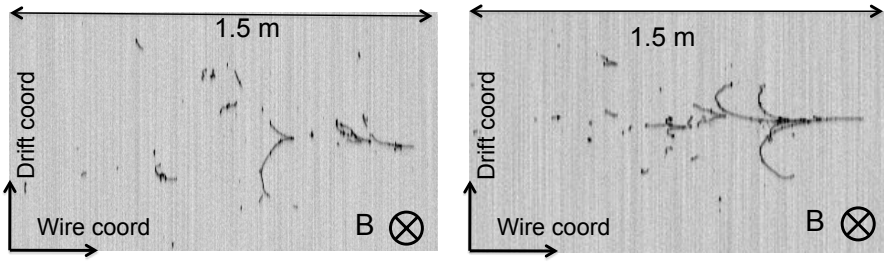


Figure 6.3: Examples of simulated electron neutrino (left) and antineutrino (right) interactions, where only the electron or the positron are respectively produced. These events represent interactions inside the ICARUS T600 with a magnetic field perpendicular to the drift and beam directions.

### 6.1.2 Discrimination procedure

Consider now a neutrino or antineutrino interaction inside the magnetized ICARUS T600 detector, as described previously. The goal of the algorithm is to distinguish the two cases, finding one or more parameters that characterize

them in presence of magnetic field. The identification is achieved through several steps, that starts from the recognition of the first part of the interaction and ends with the characterization of the particle.
First of all, I have to identify where the interaction starts, thus the primary vertex coordinates, which are already included in the simulation data.
Then, applying the standard `Qscan` hit finding and fit procedure to every event (see Chap. 3), the cluster containing the primary vertex is selected. This selection is made considering only neighbouring hits, due to the requirement of having particles coming from the original neutrino interaction. I consider as neighbouring hits, all hits that have a mutual distance smaller than 0.42 cm. This last value is the right compromise between finding a good first track and having a good number of hits to apply the algorithm. In this stage I would like to apply the algorithm to the whole sample, so we decide to choose the minimum distance that permits to have a 100% efficiency in finding cluster. As we can see in Fig. 6.4, for values just below the selected one, the efficiency is high but not the whole sample is reconstructed. However this value has to be evaluated with real data because also converting $\gamma$s could be included in the cluster: this Monte Carlo is an ideal case where the first part is composed only by electrons or positrons.

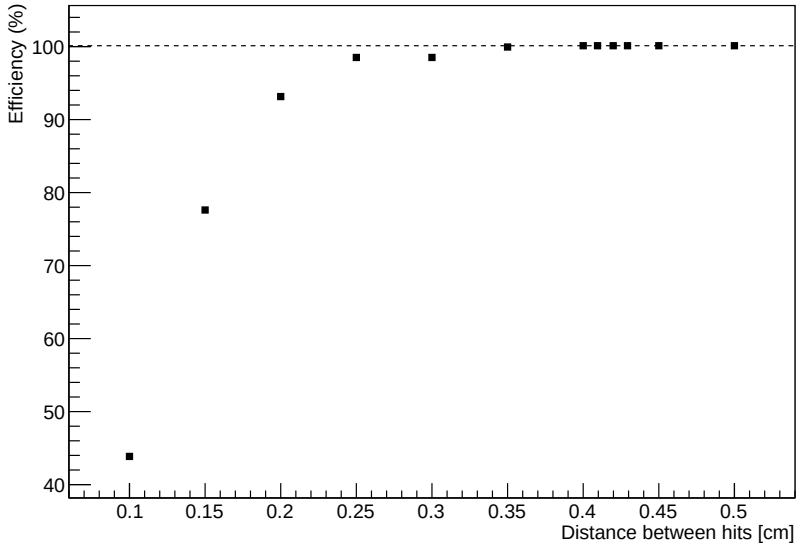


Figure 6.4: Efficiency in recognising the cluster with primary vertex as a function of different value of distance between hits. The minimum value that permits to have the best efficiency is 0.42 cm, while for lower values the efficiency does not reach the 100%.

Applying this first part of the procedure on the events in Fig. 6.3, the results shown in Fig. 6.5 are obtained, where primary vertices are depicted as the black crosses, the found hits are the red points, while the cluster containing

the primary vertex is represented by the green points.

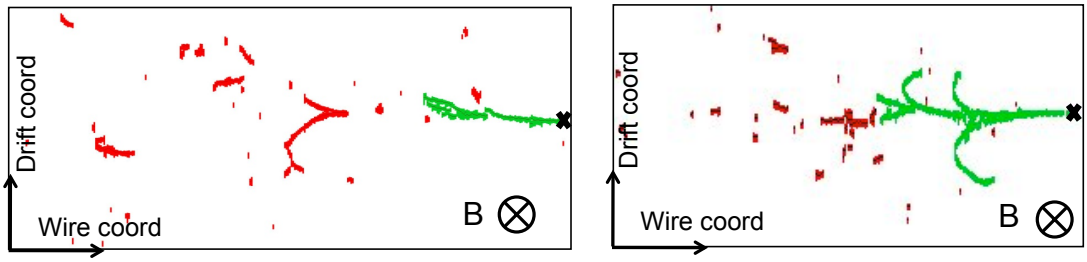


Figure 6.5: Picture of firsts steps of the separation procedure for the simulated neutrino (left) and antineutrino (right). The black cross represents the primary vetex, the red points are the hits while the green ones represent the cluster.

After the identification of the clusters, the first part of the lepton track, free of any interactions, is selected: it is the so called *clean track*. The length of the clean track $l_c$ is a crucial parameter: it defines the part of the track free from any interaction that is used as reference track for the next steps. So the entire procedure has to be repeated varying this parameter, in order to find the best compromise between efficiency of separation and acceptable background.
For any fixed value of the length $l_c$, the sequence of hits is modelled with a straight line, with given direction, obtained interpolating the points .
Finally for each hit included in the selected cluster, the oriented distance between hit actual position $h_i$ and its projection on the modelled straight line $p_i$, is evaluated (see Fig. 6.6). This parameter can be positive or negative depending on the hit position with respect to the modelled straight line: it is supposed to depend on the track curvature due to the presence of magnetic field, and hence on the charge of the lepton. Therefore the mean value of these distances, called asymmetry $A$, whose expression is

$$A = \frac{1}{n} \sum_{i=1}^{n} d(h_i, p_i), \tag{6.1}$$

can be negative or positive depending on the particle development, and it is taken as the discriminating parameter.

### 6.1.3 Results

As said above, the asymmetry parameter $A$ (Eq. 6.1) can be used to discriminate between electrons and positrons. In fact, as we can see in Fig 6.7, these two particles show an opposite value of asymmetry parameter: for most electron tracks $A$ assumes a negative value, while for positrons $A > 0$. The shown histogram is obtained for the whole sample using a fixed length of the clean track of $l_c = 3$ cm.
The efficiency, i.e. the ability of the asymmetry parameter $A$ to separate electrons from positrons, depends on the length of the clean track. However, if

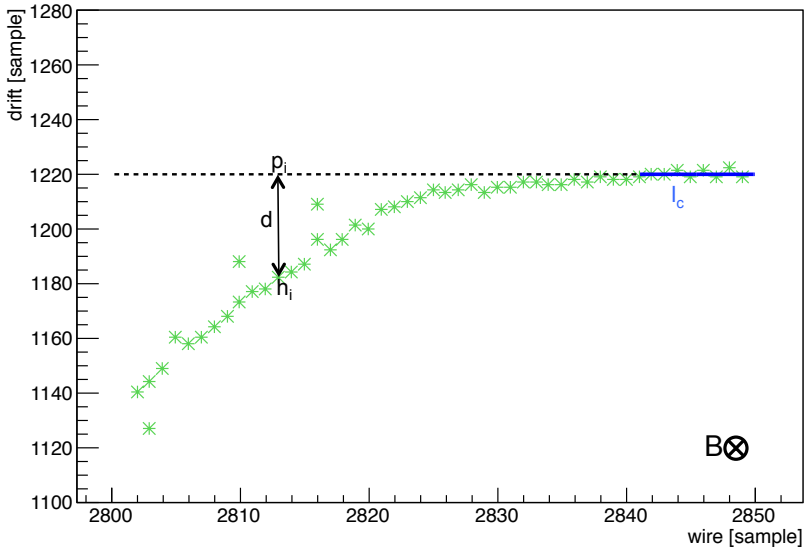


Figure 6.6: Sketch of the parameter involved in the asymmetry calculation: the green stars represent the hit of the considered cluster; the blue line is the modelled straight line of length $l_c$; $h_i$ is the actual position of the $i$ hit, while $p_i$ is its projection on the straight line.

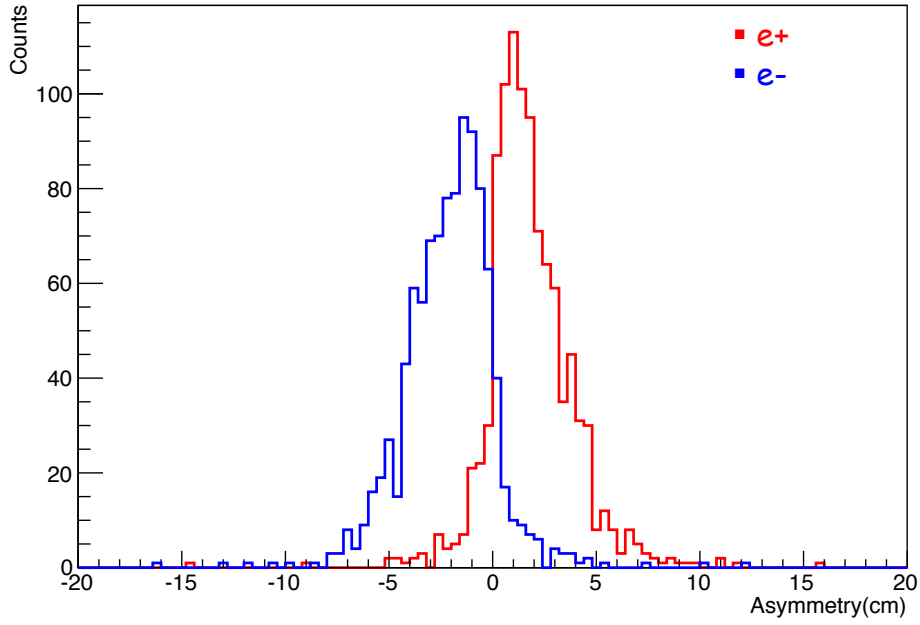


Figure 6.7: Distribution of asymmetry parameter calculated for the whole Monte Carlo sample, using $l_c = 3$ cm. The red line is referred to positrons, while blue one to electrons.

$A$ is too close to zero, separation capability drops. It is then necessary to choose a threshold value for the discrimination between the two lepton types. This threshold has to be a compromise providing both good efficiency and acceptable background contamination. Fig. 6.8 helps in the understanding of what I mean for efficiency and background contamination: for a given threshold, positrons that have an $A$ value bigger than threshold are properly recognised and their fraction represents the efficiency (red area in the figure); on the contrary, if an electron has a value of $A$ bigger than the threshold, is wrongly recognised and represents the background (blue area in the figure). The opposite case is given by an electron with $A$ value lower than the threshold, that is correctly recognised (efficiency), while a positron with $A$ lower than the threshold forms the background because it is badly recognised.

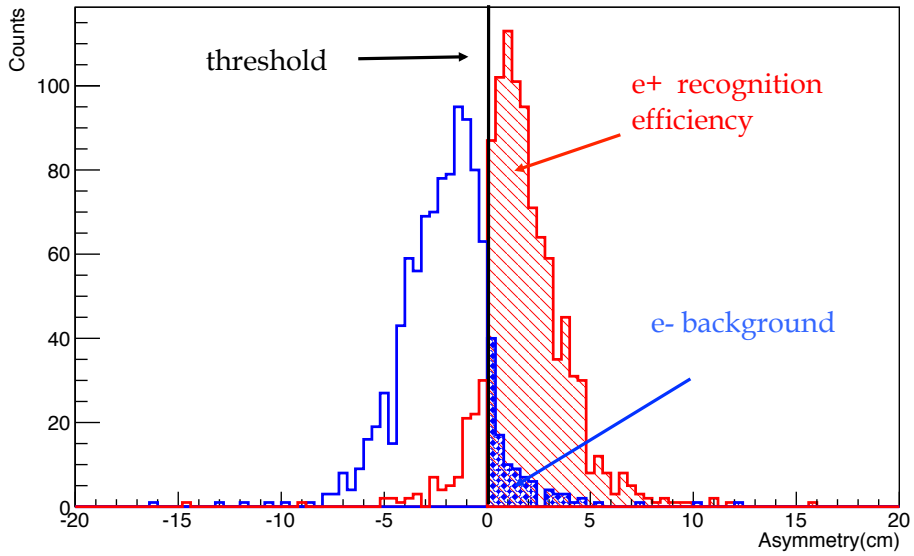


Figure 6.8: Distribution of asymmetry parameter for a fixed clean track length $l_c = 3$ cm, both for electron and for positrons. The coloured areas referred to efficiency and background contamination.

Therefore the efficiency depends both on the $l_c$ and on the threshold values. At first, in order to look for the $l_c$ optimal range, the threshold is fixed at 0, relying on the criteria of symmetry between $e^+$ and $e^-$: positrons should have $A > 0$, while electrons $A < 0$. Varying $l_c$ with steps of 0.5 cm, and counting how many electrons/positrons have negative/positive value of $A$, I obtained the plot in Fig. 6.9: the optimal value for clean track length lies in the range [2.5, 3.5] cm.
In addition, fixing $l_c$, it is possible to calculated efficiency and background contamination for different threshold values. The plots in Fig. 6.10 show the efficiency and background contamination for different value of threshold and clean track length. The threshold in asymmetry spans in the range [-1, 0] for

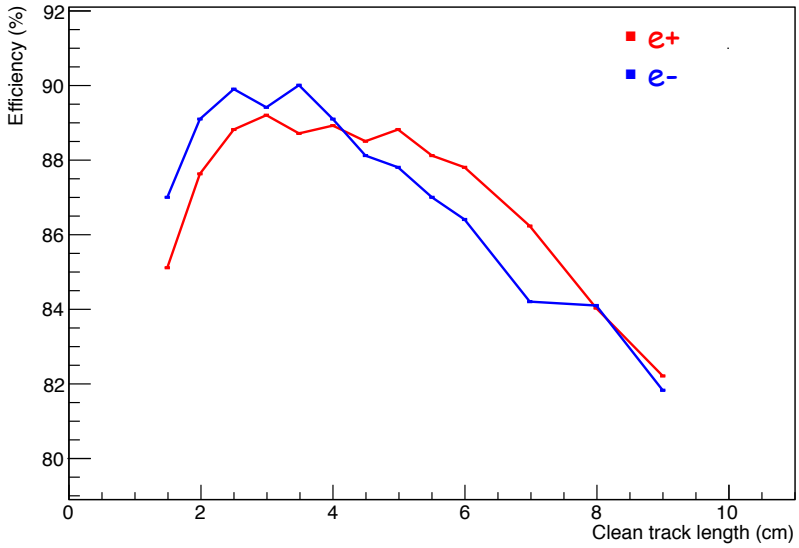


Figure 6.9: Efficiency of $e^+/e^-$ recognition as a function of clean track length, for a threshold fixed at $A = 0$. The blue line refers to electrons, while the red one to positrons.

electrons and [0, 1] for positrons, with steps of 0.2 cm. For what concern clean track length, three value have been considered: 2.5 cm , 3 cm and 3.5 cm.
The described algorithm shows very good capability on electrons/positrons separation: for example, with a clean track length $l_c$= 3 cm and a threshold in $A$ of $\pm$ 0.7 cm, it is possible to have $\sim$75% of efficiency with $\sim$5% of background contamination both for electrons and positrons.
However, more refinements will be needed to choose the final compromise values for efficiency, background and clean track length:

- apply the algorithm on an improved Monte Carlo sample, considering other neutrino/antineutrino energy and adding vertex activity due to other particles coming from the primary interaction;
- add possible magnetic field disuniformities, as expected from simulations of the field configuration;
- introduce eventual new parameters to improve electron/positron discrimination.

For what concern the last point, one hypothesis, still to be tested, is to combine asymmetry information with the curvature of the track.

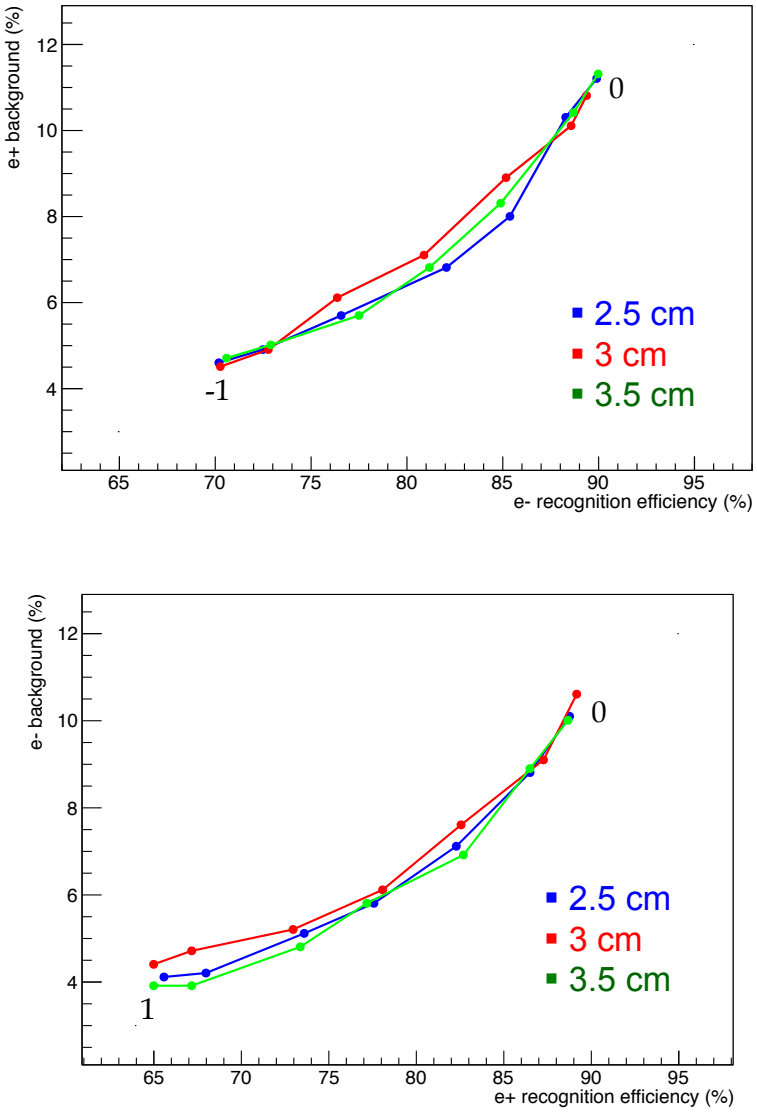


Figure 6.10: Efficiency and background contamination for different value of threshold and clean track length for electrons (top) and positrons (bottom). Each point corresponds to a threshold value in ranges: (-1, -0.9, -0.7, -0.5, -0.3, -0.1, 0) for e- and (0, 0.1, 0.3, 0.5, 0.7, 0.9, 1) for e+, for a given value of $l_c$, identified by the colour.

## 6.2 Conclusions

In the hypothesis of magnetizing the active volume of the ICARUS T600 detector, an algorithm that permits to distinguish between electrons and positrons has been developed, to discriminate between $\nu_e$ and $\bar{\nu}_e$ interactions. Using a Monte Carlo simulation, the asymmetry of the track is identified as a good parameter to separate these two classes of particles. In this algorithm there are two parameters whose values have to be chosen: the clean track length and the separation threshold. The optimisation of these parameters will be subject of a future work, accounting the foreseen improvements on Monte Carlo sample and the selection of new discrimination parameters.

# Conclusions

To give a definitive answer on the sterile neutrino presence or absence, the ICARUS T600 detector will be moved to Fermilab, where it will become the Far Detector of a series of three, for the Short Baseline Neutrino experiment. The detector will be placed at $\sim$ 600 m from the source of a $\sim$ GeV energy $\nu_\mu$ ($\overline{\nu}_\mu$) beam, in the ideal position to study the LSND anomaly. Although the T600 is already well fitted to work at Fermilab, some changes are required, in particular for the different location with respect to the LNGS: at FNAL the detector will work at shallow depth, not deep underground, and so with an high cosmic ray background. This Ph.D. thesis is devoted to describe the development of the methods, the analysis and the results for three different phenomena that affect the reconstruction procedure: electric field distortions, diffusion parameter and the presence of a magnetic field.
As said above, at Fermilab, ICARUS T600 detector will be placed at surface, with high cosmic ray flux. This could be source of local accumulation of positive ions (called space charge) that may distort the electric field along the drift direction. The uniformity of the electric field is fundamental for the event reconstruction, because it ensures an uniform drift velocity and the correct proportionality between drift time and drift coordinate.
To evaluate the presence of space charge inside the detector, I measured the bending of cosmic muon tracks in a sample of cosmic muon recorded during a test run of one T300 module, placed at surface in Pavia. Evaluating the bending parameter $\Delta T$ for each cm of the drift path, I found a maximum track bending of $\Delta T_{max} \sim 0.34$ cm, that could suggest the presence of small space charge effects inside the detector.
Also the agreement between this result and a simulation that consider electric field distortion induced by space charge, could suggest this hypothesis. Therefore, I decided to apply the analysis on track bending on cosmic muon sample collected underground at LNGS, where this effect should not be present. This sample produced a $\Delta T$ flat distribution, confirming that the track distortion observed at surface could be indeed due to space charge effects.
I can conclude that space charge effects should not be a problem for the ICARUS T600 detector at shallow depths, because the observed track bending

$\Delta T$ is within the spatial resolution of the detector. This effects could instead affect detector with larger drift path (higher than 2 m long), such as MicroBoone, one of the other detectors involved in the SBN program.
The drift coordinate is derived by the electrons drifted towards the wire planes, and its accuracy is affected by several parameters, such as the diffusion: in the ICARUS T600 detector, only the longitudinal diffusion parameter is important because the transversal one is hidden by the wire pitch. In order to evaluate this parameter, I analysed a cosmic muon sample, collected at LNGS with six different electric field values $E$.
Different electric field values mean different drift velocities and the first step of the analysis is their evaluation. Then, to determine $D$, I exploited the linear proportionality between the time spread of the signal $\sigma_t^2$ and the $D$. I plotted the $\sigma_t^2$ as a function of $t$ and fitted the graph with a straight line: from the slope of this linearity dependence I evaluated $D$ for each electric field values. They result compatible with a constant diffusion parameter, $D = 4.74 \pm 2.04\ cm^2/\text{s}$, independent from the electric field value, as expected. These are preliminary results because the errors are large, probably due to the small sample analysed; an increase of statistics will be performed in the future.
In the future life of the ICARUS T600 detector, there could be the possibility to equip the detector with a magnetic field. The presence of the magnetic field bring to the introduction of new parameters that permit better particle identification. I performed a first analysis for the discrimination between $\nu_e$ and $\bar{\nu}_e$, studying the behaviour of their interaction products (electrons and positrons). A Monte Carlo sample has been produced considering an uniform 1 T magnetic field and 500 MeV neutrino/antineutrino interactions inside the magnetized ICARUS T600. I developed an algorithm that identifies the asymmetry parameter $A$, that quantifies the mean displacement of hits from the initial direction of the track, as a good parameter to separate electrons and positrons: electrons have $A < 0$, positrons have $A > 0$. In this algorithm there are two parameters which values has to be fixed: the length of the first part of the track $l_c$, which defines the initial direction, and the threshold on $A$. To make a decision, I made calculation of efficiency and background, varying the value of both $l_c$ and asymmetry threshold. From these results, I select the optimal range of $l_c$, that lies on [2.5, 3.5] cm; for what concerns the selection threshold, a possibility could be $A = \pm\ 0.7$ cm.
The algorithm needs more refinements both on the Monte Carlo side (for example, adding vertex activity due to different particles coming from the primary interaction) and on the search of new parameters that could be associated to the asymmetry (for example the curvature of the track).

# Acknowledgements

At the end of these work I would like to warmly thank my supervisor A. Menegolli, that always advices and helps me in every moment.
Then thanks to Dr. P. Sapienza and Dr. T. Usher for their suggestions and corrections of this work.
I would like to thank also the ICARUS Collaboration, especially Pavia and Padova group for their advices and support.
For the fruitful discussions on my analysis, I would like to thank F. Pietropaolo, P. Sala, R. Sulej and D. Stefan.
And finally thanks to Prof. R. Dolfini, for the idea of diffusion parameter measurements.

# Bibliography


[1] S. L. Glashow, Nucl. Phys. 22, 579 (1961).

[2] S. Weinberg, Phys. Rev. Lett. 19, 1264 (1967).

[3] A. Salam, Proc. of the $8^{th}$ Nobel Symposium on Elementary particle theory, relativistic groups and analyticity, Stockholm, Sweden, 1968, edited by N. Svartholm, p.367-377, (1969).

[4] L. Landau, Nucl. Phys. 3 (1957) 127.

[5] T.D. Lee and C.N. Yang, Phys. Rev. 105 (1957) 1671.

[6] A. Salam, Nuovo Cim. 5 (1957) 299.

[7] Fundamentals of neutrino physics and astrophysics - C.Giunti, C.W.Kim (2007).

[8] B. Pontecorvo, Sov. Phys. JETP 6, 429 (1958). Sov. Phys JETP 7, 172 (1958).

[9] The Nobel Prize in Physics 2015, www.nobelprize.org

[10] S. M. Bilenky and B. Pontecorvo, Sov. J. Nucl. Phys., 24, 316–319 (1976). S. M. Bilenky and B. Pontecorvo, Phys. Rep., 41, 225 (1978). S. M. Bilenky and B. Pontecorvo, Nuovo Cim. Lett., 17, 569 (1976).

[11] S. Eliezer and A. R. Swift, Nucl. Phys., B105, 45 (1976).

[12] H. Fritzsch and P. Minkowski, Phys. Lett., B62, 72 (1976).

[13] L. Wolfenstein, Phys. Rev. D17, 2369 (1978).

[14] S. P. Mikheev and A. Y. Smirnov, Nuovo Cim. C9, 17 (1986).

[15] K.A. Olive et al. (Particle Data Group), Chin. Phys. C, 38, 090001 (2014) and 2015 update

[16] http://hitoshi.berkeley.edu/neutrino/

[17] F. Capozzi, et al., Phys. Rev. D 89, 093018 (2014).

[18] ALEPH, DELPHI, L3, OPAL, and SLD Collaborations, and LEP Electroweak Working Group, and SLD Electroweak Group, and SLD Heavy Flavour Group, Phys. Reports 427, 257 (2006).

[19] N. Said et al., Phys.Rev. D88, 023513 (2013).

[20] B. Pontecorvo, Sov. Phys. JETP 26, 984 (1968).

[21] C. Athanassopoulos et al. (LSND Collaboration), Nucl. Instrum. and Meth. A, 388, 149 (1997).

[22] A. Aguilar et al. (LSND Collaboration), Phys. Rev. D 64, 112007 (2001).

[23] G. Drexlin et al. (KARMEN Collaboration), Nucl. Instrum. and Meth. A, 289, 490 (1990).

[24] B. Armbruster et al. (KARMEN Collaboration), Phys.Rev. D65, 112001 (2002).

[25] A. Aguilar-Arevalo et al. (MiniBooNE Collaboration), Nucl. Instr. and Meth. A, 599, 28 (2009).

[26] A. Aguilar-Arevalo et al. (MiniBooNE Collaboration), Phys.Rev.Lett. 102, 101802 (2009).

[27] A. Aguilar-Arevalo et al. (MiniBooNE Collaboration), Phys.Rev.Lett. 105, 181801 (2010).

[28] W. Hampel et al. (GALLEX Collaboration), Phys.Lett. B420, 114 (1998).

[29] J. Abdurashitov et al. (SAGE Collaboration), Phys.Rev. C59, 2246 (1999).

[30] J. Kopp et al., JHEP 1305, (2013) 050.

[31] B. H.J. McKellar, M. J. Thomson, Phys. Rev. D49, 2710 (1994); G. Sigli, G. Raffelt, Nucl. Phys. B406, 423 (1993); D. Hollander, arXiv:1301.5313 (2013).

[32] C. Giunti and M. Laveder, Phys.Rev. C83, 065504 (2011).

[33] K. Nakamura et al. (Particle Data Group), J.Phys.G G37, 075021 (2010).

[34] T. Mueller et al., Phys.Rev. C83, 054615 (2011).

[35] G. Mention et al., Phys.Rev. D83, 073006 (2011).

[36] Gariazzo, S. et al., Light sterile neutrinos, arXiv:1507.08204v1.

[37] C. Giunti,Laveder M, Li Y and Long H, Phys. Rev. D 88, 073008 (2013)

[38] D. Lhuillier, AIP Conference Proceeding 1666 (2015) 180003.

[39] M. Pequignot (Nucifer and Stereo Collaborations), Nucl. Part. Phys. Proc. 265-266 (2015) 126-128.

[40] M. Danilov, Sensitivity of the DANSS detecotr to short range neutrino oscillation, Proceeding of the 2013 European Physical Society Conference on High Energy Physics, EPS-HEP2013, p. 493.

[41] N. Ryder, First results of the deployment of a solid detecotr module at the SCK-CEN BR2 reactor, Proceeding of the 2015 European Physical Society Conference on High Energy Physics, EPS-HEP2015, p. 071.

[42] A.P. Serebrov et al. (Neutrino4 Collaboration) arXiv:1205.2955.

[43] I.S. Yeo et al. , J. Korean Phys. Soc. 64 (3) (2014) 377-381.

[44] M. Cribier et al., Phys. Rev. Lett. 107 (2011) 201801.

[45] A. Gando et al, arXiv:1312.0896.

[46] J.M. Conrad et al, Phys. Rev. D 89 (2014) 057301.

[47] D.A. Dwyer et al, Phys Rev. D87 (9) (2013) 093002.

[48] C. Grieb et al., LENS as a probe of sterile neutrino mediated oscillations, Proceeding of the 12 International Workshop on Neutrino Telescope 2007.

[49] V. Barinov et al., arXiv:1602.03826.

[50] J.A. Formaggio et al., Phys. Rev. D85 (2012) 013009.

[51] B. Caccianiga, Future short baseline neutrino searches with nuclear decays, AIP Conference proceeding 1666 (2015) 180002.

[52] J. Spitz, Future short baseline sterile neutrino searches with accelarators, AIP Conf. Proc. 1666 (2015) 180004.

[53] M. Harada et al., arXiv:1310.1437.

[54] P.Kyberd et al., arXiv:1206.0294.

[55] A.Bungau et al., Phys. Rev. Lett 109 (2012) 141802.

[56] F.J. Hasert et al., Phys. Lett. B46, 121 (1973); Phys. Lett. B46, 138 (1973).

[57] C. Rubbia, The liquid-argon time projection chamber: a new concept for neutrino detector,CERN-EP-77-08 (1977).

[58] P. Benetti et al. (ICARUS Collaboration), Nucl. Instr. and Meth. A, 332, 395 (1993).

[59] P. Cennini et al. (ICARUS Collaboration), Nucl. Instr. and Meth. A, 345, 230 (1994).

[60] F. Arneodo et al. (ICARUS Collaboration), Nucl. Instr. and Meth. A, 449, 36 (2000).

[61] P. Cennini et al. (ICARUS Collaboration), Nucl. Instr. and Meth. A, 432, 240 (1999).

[62] F. Arneodo et al. (ICARUS Collaboration), Nucl. Instr. and Meth. A, 498, 293 (2003).

[63] F.Arneodo et al. (ICARUS Collaboration), Nucl. Instr. and Meth. A, 508, 287 (2003).

[64] S. Amerio et al. (ICARUS Collaboration), Nucl. Instr. and Meth. A, 527, 329 (2004).

[65] C. Rubbia et al. (ICARUS Collaboration), JINST 6 P07011 (2011).

[66] M. Antonello et al. (ICARUS Collaboration), JINST 9 P08003 (2014).

[67] M. Antonello et al. (ICARUS Collaboration), JINST 9 P12006 (2014).

[68] M. Antonello et al. (ICARUS Collaboration), JINST 10 P12004 (2015).

[69] S. Amoruso et al. (ICARUS Collaboration), Nucl. Instr. and Meth. A, 523, 275 (2004).

[70] G. Aquistapace et al., CERN 98-02., INFN/AE-89-05 (1998).

[71] R. Bailey et al., CERN-sl799-034 (DI), INFN/AE-99/05 Addendum (1999).

[72] E. Gschwendtner et al., CERN-ATS-2010-153 (2010).

[73] A. Cesana et al., Status report of the 2010-11 CNGS data processing, Tech. Rep. ICARUS-TM 12-06 (2012).

[74] F. Boffelli et al., Advances in 2010-12 CNGS data processing and preliminary results, Tech. Rep. ICARUS-TM 13-04 (2013).

[75] F.Boffelli et al., Final update of 2010-12 CNGS data processing, Tech. Rep. ICARUS-TM 15-01 (2015).

[76] M. Antonello et al. (ICARUS Collaboration), Advances in High Energy Physics, 260820 (2013).

[77] M. Antonello et al. (ICARUS Collaboration), Eur. Phys. J. C 73, 2345 (2013).

[78] M. Antonello et al. (ICARUS Collaboration), Eur. Phys. J. C 73, 2599 (2013).

[79] F. Capozzi et al., Phys. Rev. D 89, 093018 (2014).

[80] J. Beringer et al. (Particle Data Group), Phys. Rev. D86, 010001 (2012).

[81] G.J. Feldman and R.D. Cousins, Phys. Rev. D57, 3973 (1998).

[82] N. Agafonova et al. (OPERA Collaboration), New J. Phys.13, 053051 (2011).

[83] N. Agafonova et al. (OPERA Collaboration), JHEP 07 (2013) 004.

[84] M.G. Aartsen et al. (IcaCube Collaboration), arXiv:1605.01990v2.

[85] T. Miceli (MiniBooNE Collaboration), arXiv:1411.4572

[86] C. Rubbia, for the ICARUS Collaboration, Using the beam bunch-structure with the T600 detector, internal SBN report (2014).

[87] R. Acciari et al., A Proposal for a Three Detector Short-Baseline Neutrino Oscillation Program in the Fermilab Booster Neutrino Beam, arXiv:1503.01520.

[88] ICARUS/WA104 Coll. , Status and plans of WA104/ICARUS, CERN-SPSC-2016-019, SPSC-SR-186-2016 .

[89] A. Falcone, Ph.D. Thesis, University of Pavia (2015).

[90] A.Bueno, J.Rico and A. Rubbia, Tech. Rep. ICARUS-TM 2002/03

[91] M.Antonello, N.Canci, E.Scantamburlo, E.Segreto, D.Stefan, R.Sulej,Tech. Rep. ICARUS-TM 11-04.

[92] F.James, MINUIT-Function Minimization and Error Analysis, CERN Program Library, 1998.

[93] S.Amoruso et al., Nucl. Instr. and Meth. A, 516, 1 (2004).

[94] M. Miyajima, et al., Phys. Rev. A, vol. 9, no. 3, pp. 1438–1443, 1974.

[95] B. Kegl, A. Krzyzak, T. Linder, and K. Zeger, IEEE Transactions on Pattern Analysis and Machine Intelligence, vol. 22, no. 3, pp. 281–297, 2000.

[96] W.R.Leo, Techniques for Nuclear and Particle physiscs experimentis, (1994) Springer Verlag.

[97] M. Torti on behalf of the ICARUS Coll., EPJ Web of Conference 126, 05013 (2016).

[98] National Institute of Standards and Technology, Web site: http://www.nist.gov/.

[99] T.K. Gaisser et al.(Particle Data Group), Cosmic Rays rev., http://pdg.lbl.gov/2015/reviews/rpp2015-rev-cosmic-rays.pdf

[100] S.Palestrini et al. , Nucl. Instr. and Meth. A 421, 75, (1999).

[101] Rene Brun and Fons Rademakers, *ROOT, An Object Oriented Data Analysis Framework*, Proceedings AIHENP'96 Workshop, Lausanne, Sep. 1996, Nucl. Inst. and Meth. in Phys. Res. A 389 (1997) 81-86. See also http://root.cern.ch/

[102] ProtoDUNE Collaboration, Proposal for a Full Scale Prototype Single Phase Liquid Argon Time Projection Chamber and Detector Beam Test at CERN, CERN-SPSC-2015-020, SPSC-P-351.

[103] M. Mooney (MicroBoone Collab.), The MicroBooNE Experiment and the Impact of Space Charge Effects, arXiv:1511.01563v1 (2015).

[104] M.Mooney, Space charge effects at ProtoDUNE, ProtoDUNE Measurements Meeting, 2015.

[105] J.H. Parker and J.J. Lowke, Phys. Rev. 181 (1969) 290.

[106] A. Fick, Ann. der. Physik 94 (1855) 59.

[107] A. Fick, Phil. Mag. 10 (1855) 30.

[108] A.Einstein, Annalen der Physik 322 (1905) 549-560.

[109] M. von Smouluchowski, Annalen der Physik 326 (196) 756-780.

[110] G. H. Wannier, Bell System Technical Journal 32 (1) (1953) 170-354.

[111] R.E. Robson, Australian Journal of Physics 25 (1972) 685.

[112] W. Walkowiak, Nucl. Instr. and Meth. A 449 (2000) 288-294.

[113] J. Lekner, Phys. Rev. 158 (1967) 130.

[114] S. Huang and G. Freeman, Phys. Rew. A 24, 2 (1981).

[115] B. Halpern, J. Lekner, S. A. Rice, R. Gomer, Phys. Rev. 156 (1967) 351–352.

[116] W.P. Allis and H.W. Allen, Phys. Rev. 52 81937) 703-707.

[117] J. Huber and K. Jepsen, "The dawn of DUNE", Symmetry Magazine, March 2015.

[118] A. Ferrari et al., *FLUKA: a multi-particle transport code.*, Tech. Rep. CERN-2005-10, INFN/TC 05/11, SLAC-R-773 (CERN, 2005).

[119] G. Battistoni, S. Muraro, P. R. Sala et al., "The FLUKA code: description and benchmarking," in Proceedings of the Hadronic Shower Simulation Workshop, M. Albrow and R. Raja, Eds., vol. 896 of AIP Conference Proceeding, pp. 31–49, September 2007.

[120] A. Ferrari et al., ICARUS TM/01-05 (2001).